A TRIBOLOGICAL AND BIOMIMETIC STUDY OF POTENTIAL BONE JOINT REPAIR MATERIALS

A Dissertation

by

RAHUL RIBEIRO

Submitted to the Office of Graduate Studies of
Texas A&M University
in partial fulfillment of the requirements for the degree of

DOCTOR OF PHILOSOPHY

December 2006

Major Subject: Materials Science and Engineering

A TRIBOLOGICAL AND BIOMIMETIC STUDY OF POTENTIAL BONE JOINT REPAIR MATERIALS

A Dissertation

by

RAHUL RIBEIRO

Submitted to the Office of Graduate Studies of
Texas A&M University
in partial fulfillment of the requirements for the degree of

DOCTOR OF PHILOSOPHY

Approved by:

Chair of Committee,	Hong Liang
Committee Members,	Terry Creasy
	Harry Hogan
	Andreas Holzenburg
Chair of Interdisciplinary Faculty,	Joseph H. Ross Jr.

December 2006

Major Subject: Materials Science and Engineering

ABSTRACT

A Tribological and Biomimetic Study of Potential Bone Joint Repair Materials.

(December 2006)

Rahul Ribeiro, B.E., Marine Engineering and Research Institute, India;

M.S., Mechanical Engineering, Texas A&M University

Chair of Advisory Committee: Dr. Hong Liang

This research investigates materials for bone-joint failure repair using tribological and biomimicking approaches. The materials investigated represent three different repairing strategies. Refractory metals with and without treatment are candidates for total joint replacements due to their mechanical strength, high corrosion resistance and biocompatibility. A composite of biodegradable polytrimethylene carbonate, hydroxyl apatite, and nanotubes was investigated for application as a tissue engineering scaffold. Non-biodegradable polymer polyimide combined with various concentrations of nanotubes was investigated as a cartilage replacement material.

A series of experimental approaches were used in this research. These include analysis of material surfaces and debris using high-resolution techniques and tribological experiments, as well as evaluation of nanomechanical properties. Specifically, the surface structure and wear mechanisms were investigated using a scanning electron microscope and an atomic force microscope. Debris morphology and structure was investigated using a transmission electron microscope. The debris composition was

analyzed using an X-ray diffractometer. Nanoindentation was incorporated to investigate the surface nanomechanical properties.

Polytrimythelene carbonate combined with hydroxyapatite and nanotubes exhibited a friction coefficient lower than UHMWPE. The nanoindentation response mimicked cartilage more closely than UHMWPE.

A composite formed with PI and nanotubes showed a varying friction coefficient and varying nanoindentation response with variation in nanotube concentration. Low friction coefficients corresponded with low modulus values. A theory was proposed to explain this behavior based on surface interactions between nanotubes and between nanotubes and PI. A model was developed to simulate the modulus as a function of nanotube concentration.

The boronized refractory metals exhibited brittleness and cracking. Higher friction coefficients were associated with the formation of amorphous debris. The friction coefficient for boronized Cr (~0.06) under simulated body fluid conditions was in the range found in natural joints.

ACKNOWLEDGEMENTS

The directions taken in my life and the overall success obtained in completing this dissertation was not achieved alone. Several individuals played an informative and supportive role.

I would first and foremost like to acknowledge my creator Almighty God for this wonderful life and interesting experience on earth. My parents played a very important role of selflessness and love, without which I would not have been as fortunate as I have. My dear siblings Sarita and Vinay were constant sources of support, love and encouragement throughout my life.

I'd like to acknowledge the work and effort put in by all teachers, tutors and mentors throughout my schooling that went into educating and moulding me into the person that I am today.

During my undergraduate days, the four years spent at the Marine Engineering and Research Institute at Kolkata, India prepared me for a life in the open, real world. The institution trained me and my fellow students to work as engineers on board merchant marine vessels.

My graduate studies, comprising a Master of Science in Mechanical Engineering and a Doctor of Philosophy degree in Materials Science and Engineering were both obtained at Texas A&M University, College Station, Texas. Several individuals and the high standard of educational facilities at this university were instrumental in achieving these prestigious qualifications.

I am grateful to my Master of Science advisor, Dr. Roger Morgan for his mentoring and financial support. I also wish to thank the other members of my Master of Science committee, Dr. H. J. Sue and Dr. John Whitcomb, for their guidance and support.

I am ever grateful to my PhD. Advisor, Dr. Hong Liang for giving me an opportunity to work on this project. I thank her for her financial support and mentoring throughout. Her constant guidance and ever willingness to help has got me where I am.
I also thank other members of my committee, Dr. Terry Creasy, Dr. Andreas Holzenburg and Dr. Harry Hogan for agreeing to serve on my committee and for their guidance and support.

I wish to acknowledge Dr. Donald Darensbourg of the Chemistry department, Texas A&M University for serving as a substitute on my PhD. Committee and his students Poulomi Ganguly and Wonsook Choi for help in preparing polymeric composite samples.

I wish to acknowledge Dr. Zoubeida Ounaies and her graduate student colleague Sumanth of the Aerospace Engineering department, Texas A&M University for support with sample preparation.

All my research colleagues helped me in some capacity or other towards my learning and progress towards my degree and I acknowledge their support.

I also wish to acknowledge members of the Microscopy and Imaging Center, Dr. Zhiping Luo, Ann Ellis, Rick Littleton, Dr. Michael Pendleton and Tom Stephens for training and support with electron microscopy equipment. I wish to thank Dr. N. S.

Bhuvanesh for help with X-ray diffraction and Yulia Vasilyeva for help with nanoindentation.

Last but not the least, I wish to acknowledge the support of the funding agencies, NSF (CMS-0239136), Texas Engineering and Experiment Station and Texas A&M University.

TABLE OF CONTENTS

Page

LIST OF FIGURES

FIGURE Page

FIGURE Page

LIST OF TABLES

CHAPTER I

INTRODUCTION TO BIOMATERIALS AND BONE JOINT REPAIR

A biomaterial is defined as "a nonviable material used in a medical device, intended to interact with biological systems" [1].

Over the years, synthetic biomaterials have been applied in various medical treatment areas, namely dentistry [2, 3], plastic surgery [4,5], cardiology [6,7], orthopaedics [8, 9], and tissue engineering [10, 11].

A biomaterial needs to possess certain properties depending on its application and desired function. Four broad categorical requirements of a biomaterial are [12].

- Biocompatible - The material should be well accepted by the body and should not incite a negative response from the host.
- Sterilizable - It must be able to undergo sterilization. Common techniques to sterilize materials are bombarding with gamma rays, ethylene oxide gas and steam autoclaving.
- Functional- The material should have the ability to be shaped and tailored to meet required functions. This depends on the molecular structure.
- Manufacturable - The material should be able to be manufactured by techniques that are cost and time effective. Being able to be manufactured by already developed techniques would be a great advantage.

Biomaterials can also be classified as i) biological and ii) synthetic. Further sub-classifications are biomaterials for soft and hard tissue. Finally based on the material

---

This dissertation follows the style of the *Journal of Materials Research.*

type, they can be classified as metallic, polymeric, ceramic and composites as listed in Table 1.1.

TABLE 1.1. Classification of biomaterials.

Material source	Material type	Examples
Biological	Soft tissue	skin, ligament, cornea
	Hard tissue	bone, teeth, nails
Synthetic	Polymeric	Ultrahigh molecular weight polyethylene (UHMWPE), Polymethylmethacrylate (PMMA)
	Metallic	Stainless steel, Co-Cr- Mo alloy, Titanium alloys
	Ceramic	Alumina (Al_2O_3), Zirconia (ZrO_2).
	Composite	Carbon fiber (CF)/poly ether etherketone (PEEK), CF/UHMWPE

A. BONE AND BONE JOINTS

As stated by Currey [13], bone of present day mammals and birds is a stiff skeletal material made principally of the fibrous material called collagen. This is impregnated with a mineral closely resembling calcium phosphate. Acting together with the intestine and kidney, bone contributes to regulate calcemia. Along with this metabolic activity, bone is devoted to important mechanical functions. The hardness, moderate elasticity, plasticity and brittleness of bone, make it an ideal tissue for standing and moving, and for the insertion of muscles. They form levers for movement, and also protect soft tissues and organs [14]. Cavities in the center of bones serve as containers of red blood cells, as a marrow producer and its storage. Bony tissues of the entire body are a huge

warehouse of minerals to be tapped by the body in response to different physiological needs [15]. The skeleton and its individual elements provide a framework or scaffolding that supports the soft tissues of the body and permits them to function without collapsing. The skeleton acts as armor, shielding important soft tissues from damage. The joints and spongy bone tissue in the skeleton function as shock absorbers, modulating the impacts produced by locomotion and other movements and supports the soft tissues of the body. Bones act as levers or struts, to be pulled upon by muscles, producing movement and locomotion. Contracting muscles anchored to bones, which in turn are articulated with other bones at joints, produce movement or action. The different actions that can be produced by bones are flexion, which decreases the angle at a joint, extension, which increases the angle, rotation, which rotates a bone, gliding, which is the movement of one bone past another, circumduction, which causes a bone to pivot about the joint and form the base of a cone at the distal end, abduction, which moves a bone away from the body midline, and adduction, which moves the bone towards the body midline [15] (Fig. 1.1).

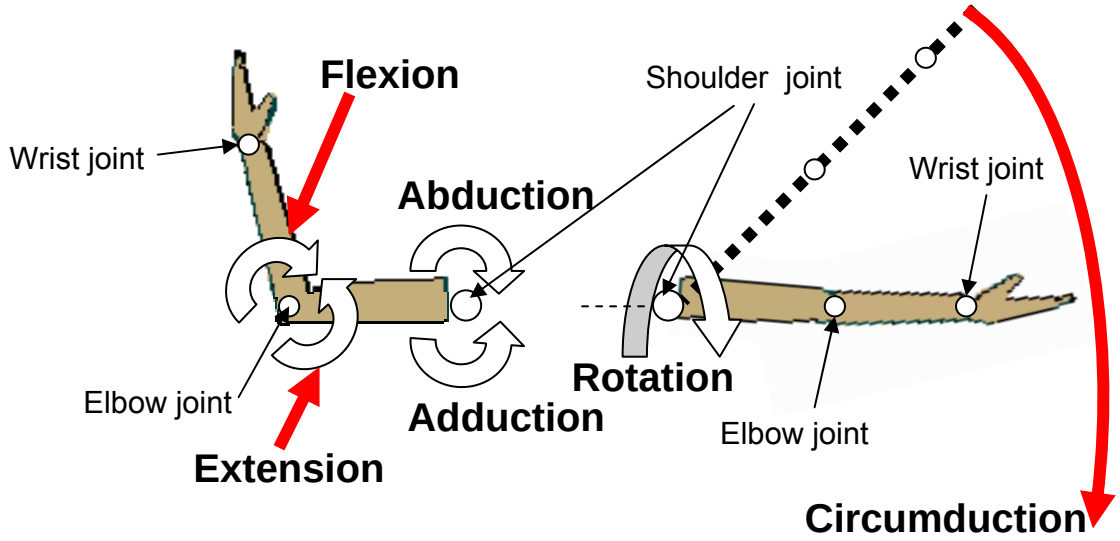

FIG. 1.1. Joint movements

A bone joint is formed at the end of two or more bones that are connected by tissues. The functions of the joint are to provide movement and stability. Joints resist some forces to prevent certain motions and allow other forces to act upon them. Joints are classified according to their structure, namely, fibrous, cartilaginous, synovial [16].

In fibrous joints, the bones are connected by a dense, fibrous tissue called ligament. These joints do not allow much movement [16].

Two types of cartilaginous joints exist. They are synchondrosis (bones fused by hyaline cartilage) and symphyses (joint in which bones are joined by fibrous cartilage) [16].

Synovial joints have the greatest degree of mobility [16]. They possess a joint cavity which is enclosed by a strong fibrous capsule and lined by a synovial membrane [17]. The synovial membrane secretes the synovial fluid which flows over the surfaces of

the joint, acting as both a lubricant, and a nutrient [16]. Each bone end is covered by articular cartilage. The synovial membrane is attached to the articular cartilage and forms a bridge between the bones of the joint (Fig. 1.2).

B. CARTILAGE

Cartilage is the evolutionary tissue of majority of bone. In an adult human, cartilage is present in the larynx, trachea, nose, ears, and ribs [17]. It is also present at the ends of long bones, forming articulating surfaces of bone joints. Cartilage consists of chondrocyte cells, embedded in an extracellular matrix.

Cartilage is present in different forms. The three most common forms are [18]:

- *Hyaline cartilage:* It has a smooth glass-like surface. It is found in the ventral ends of ribs, in the tracheal rings, and covering the joint surfaces of bones (articular cartilage). The growth plate of bone is also composed of this type of cartilage.
- *Elastic cartilage:* It is found in the external ear, eustachian tubes, and epiglottis. It has greater opacity, flexibility, and elasticity than hyaline cartilage. Its extracellular matrix is permeated with dense, branching elastic fibers unique to this type of cartilage.
- *Fibrocartilage:* It occurs in intervertebral disks, the pubic symphysis, and in the bony attachments of certain tendons. It also may form when hyaline cartilage is damaged.

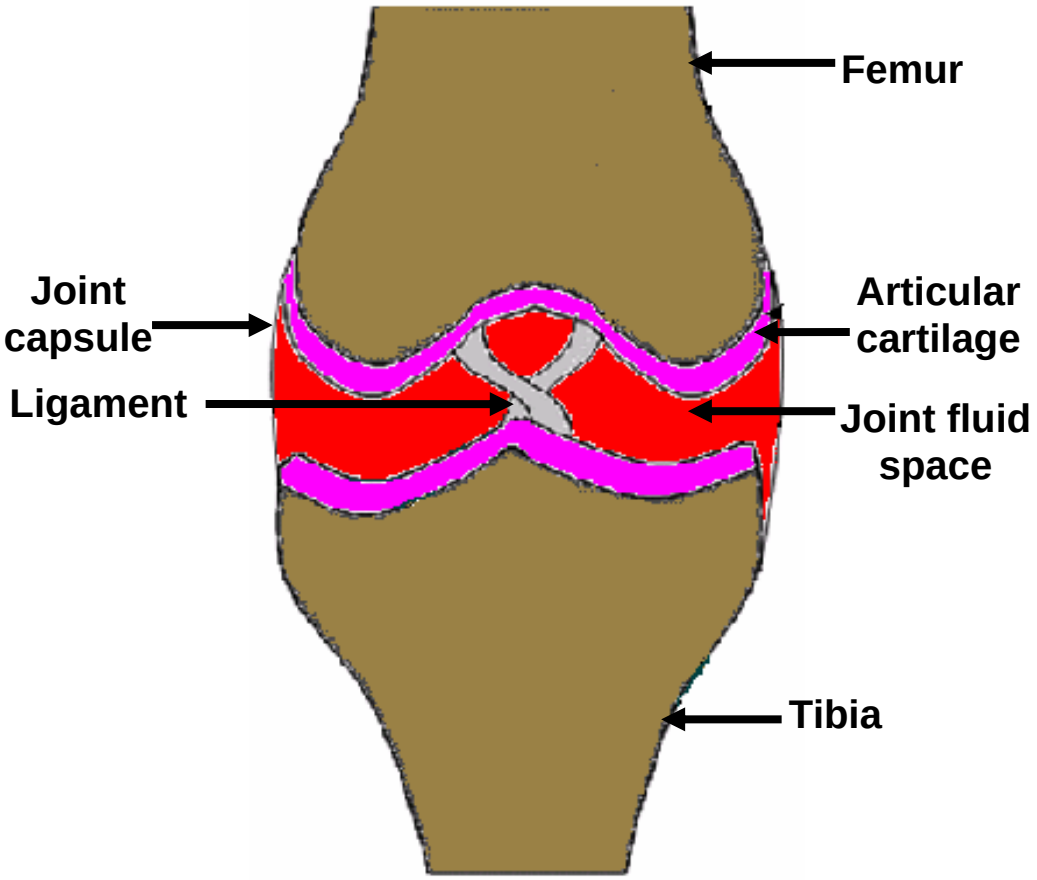

FIG. 1.2. Synovial joint (knee joint shown)

This research focuses on articular cartilage. It is made up of hyaline (glassy) cartilage and is smooth, glistening and bluish white in appearance in the healthy condition [19]. The appearance changes when it is diseased [19]. There are two major and distinct phases present in articular cartilage. One is a fluid phase made up of water and electrolytes, and the other, a solid phase consisting of chondrocytes (cartilage cells), collagen fibrils, proteoglycans, and other glycoproteins [19]. The percentage composition of major components in articular cartilage is given in Table 1.2 [19].

TABLE 1.2. Major components of cartilage and their composition [19].

Tissue	Water	Collagen II (wet wt.)	Proteoglycan (wet wt.)
Articular cartilage	60-85%	15-22%	4-7%

C. ARTHRITIS

Osteoarthritis (OA) is the joint disease with the highest prevalence worldwide [20]. It is characterized by progressive loss of articular cartilage leading to chronic pain and functional restrictions [21]. Causes of OA are trauma, genetic predisposition, and defective position of joints, ageing and malnutrition [22]. There is progressive loss of articular cartilage followed by attempted repair, remodeling, sclerosis of subchondral bone and formation of osteophytes [23, 24]. Subchondral cysts, or cavities have also been detected [25]. Symptoms of the disease are pain, restriction of motion, joint subluxation, deformity, inflamation and malalignment [26, 27, 28]. The most common causes of cartilage failure are:

- *Age:* As age increases, cartilage cells synthesize smaller aggrecan molecules and less functional link proteins leading to deterioration of the tissue [29, 30]
- *Dysplasia:* Abnormal development or growth of tissues, organs, or cells [31, 32]
- *Trauma:* A serious bodily injury or shock, as from violence or an accident [33, 34]
- *Genetic disorder:* Hereditary abnormality [35]
- *Osteopetrosis:* Stiff subchondral bone leading to less damping of loads [36]
- *Metabolic changes* [37, 38]

D. TECHNIQUES OF JOINT REPAIR

1. Restoration of degenerated cartilage

Surgeons have attempted to treat arthritic patients by penetrating the subchondral bone, to stimulate formation of a new articular surface [39, 40]. Penetration causes a disruption of blood vessels, leading to the formation of a fibrin clot over the bone surface. Undifferentiated mesenchymal cells migrate into the clot, proliferate and differentiate into cells having morphological features of chondrocytes [41]. In some instances, they form a fibrocartilagenous surface, but in others they fail to restore an articular surface. Examination of the new tissue formed by this method indicated that it lacks the structure, composition, mechanical properties and durability of articular cartilage [42, 33, 43].

2. Total joint Replacement

Joint prostheses initially began as a hemiartroplasty type with only one arthritic surface being replaced [44]. The results were found to be unsatisfactory. In total joint replacements, the cartilage and part of the subchondral bone on either side of the joint is replaced by synthetic materials (Fig. 1.3). In the 1930's Philip Wiles of Middlesex Hospital, England, designed and inserted the first Total Hip Replacements (THRs) [45]. McKee, who was a trainee with Wilkes, developed various types of uncemented total hip replacements in the 1940's and 1950's [45]. Haboush introduced polymethylmethacrylate as a bone cement in 1953 [46]. In the early 1950's Sir John Charnley used Teflon as a resurfacing material for the femoral head and acetabular cup [47]. The Teflon bearings wore out in two years and the wear particles were found to be harmful [48]. In the early

1960's, Charnley attempted replacing the acetabular socket with polyethylene [49]. It was a major success and the use of metals and polyethylene as articulating materials in joint replacement is widely used even today.

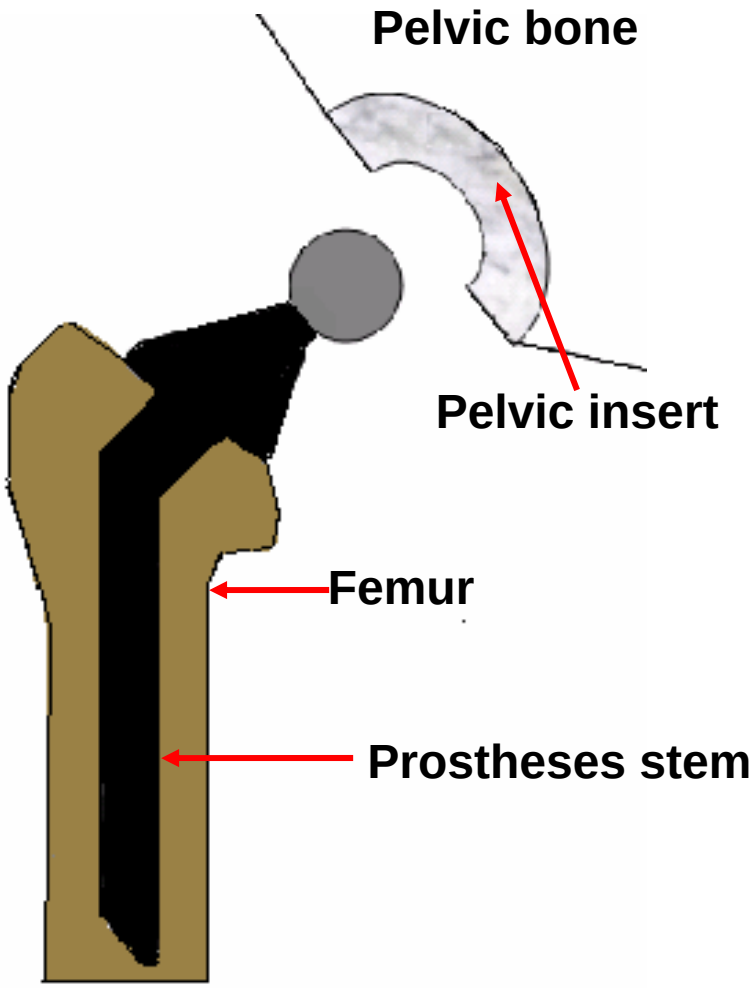

FIG.1.3. Total hip replacement

In joint replacement surgery, the idea is to replace the diseased articular surface with one made from a synthetic material. This new joint surface is a part of the total artificial joint, which is itself fixed to the bone. The major design issues in artificial joint replacement are: the geometric and material design of the articulating surfaces and design of the interface between the artificial joint and the surrounding bone.

Figure 3 shows the typical components found in a totally replaced hip joint. The two articulating surfaces are a metal ball called the femural head and ultra high molecular weight polyethylene (UHMWPE) liner. The part that interfaces with the bone is usually made of a metal alloy. There are two widely used methods for interfacing the joint with the bone [50]. They are: using a polymethylmethacrylate (PMMA) cement to adhere the metal to the bone and using a porous metal surface to create a bone ingrowth interface.

3. Tissue engineering and gene therapy

Articular cartilage has limited capacity for self-repair, due to the lack of blood supply. Chondral injuries are usually found to exist entirely within the cartilage and do not penetrate into the subchondral bone [51, 52]. Osteochondral injuries penetrate through the vascularized subchondral bone. In this case, some repair occurs as mesenchymal chondroprogenitor cells invade the lesion and form cartilage [51, 52]. However, this tissue is transient and fibrous and does not have the functional properties of native hyaline cartilage [52]. Tissue engineering is the process of replacing living tissue to restore, maintain or improve tissue function. It is a process of transplanting cells into a biocompatible, biodegradable scaffold that provides appropriate mechanical strength to

induce three-dimensional tissue growth. This construct can be implanted and should function, remodel and grow like native tissue.

It has been stated by Tuli et al. [51] that studies incorporating hyluronan and collagen based natural biopolymeric scaffolds have shown promise, however there were problems with lot inconsistency and the potential for immunogenic problems. This has prompted investigators to focus mainly on synthetic polymer-based scaffolds, such as the poly-α-hydroxy esters [51]. Freed et al. [53] have shown that the rates of chondrocyte proliferation and deposition of cartilage specific glycosaminoglycans are significantly higher on polyglycolic acid (PGA)-based scaffolds as compared to poly(L)lactic acid (PLA)-based scaffolds, while both polymers have been shown to promote proteoglycan (cartilage material component) synthesis at higher rates than collagen scaffolds [54].

4. Cartilage replacement

Natural cartilage is a porous material which contains approximately 60-85% by weight of water. Several authors have therefore studied the efficacy of using porous gels as artificial cartilage [55-58]. These materials showed promising frictional and mechanical properties for use as artificial cartilage materials. Święszkowski et al. [59] studied a soft cryogel material, having shock absorbing properties, similar to cartilage. Freeman et al. [58] investigated hydrogels with variable factors being applied load, lubrication, hydrogel crosslink density and degree of hydrogel hydration. Covert et al. [57] studied the friction characteristics of polyvinyl alcohol cryogel (PVA-c).

E. TRIBOLOGY

Tribology is defined as the science of the mechanisms of friction, lubrication, and wear of interacting surfaces that are in relative motion. Three fundamental aspects related to tribology are [60]:

- The effect of the environment on surface characteristics through physical-chemical interactions
- The force generation and transmission between the surfaces in contact
- The behavior of the material near the surface in response to the external forces acting at contact points on the surfaces

Usually, the nature of the two surfaces in contact, have an effect on the friction and wear characteristics. The properties of the surface are usually different from those of the bulk. This is due to the significance of the electronic and atomic structures of surfaces as well as the common defects on and near the surface (e.g. disloations) [60].

It is known that a solid surface is created through cracking or when a liquid solidifies [60]. According to Suh [60], a surface is defined as an asymmetric boundary separating two areas. Generally, these areas are dominated by thermal energy and intermolecular forces[61]. The surface is an asymmetric boundary between two regions: one region has interatomic forces that are greater than the thermal energy of each atom so the atoms are closely packed (into the material). The other region is exposed to a fluid or vacuum with no near-neighbor interatomic interactions [61]. Because of this asymmetry, the atoms of the outer surface layer experience different forces from those of the bulk.

As a consequence, the electronic structure at the surface is also different from that of the bulk.

1. Friction

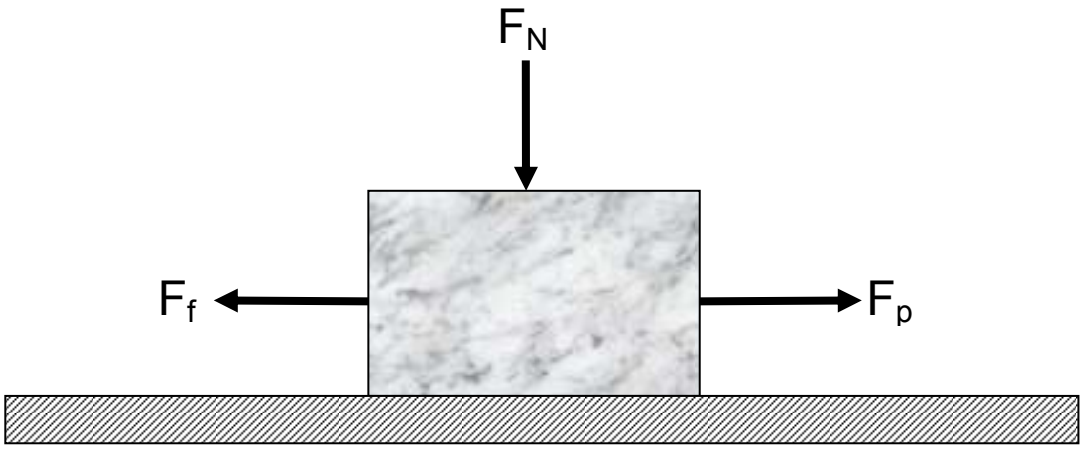

F_N: Normal load
Fp: Applied force
F_f: Friction force

Coefficient of friction $\mu = \frac{F_f}{F_N}$

FIG. 1.4. Frictional force between two sliding surfaces

When two bodies are in contact and in relative motion, a finite force is required to maintain this motion due to the nature of the surfaces in contact. This force is the friction force between the two surfaces (Fig. 1.4). A coefficient of friction, usually designated by the Greek letter 'μ', is calculated by dividing the friction force by the normal force, $\mu=F_f/F_N$ (Fig. 1.4).

Friction force follows three basic laws put forth by Amontons (1663-1705) (i and ii) and Coulomb (1736-1806) (iii): i) It is proportional to the normal load on the surfaces in contact, ii) It is independent of the area of contact and iii) the kinetic friction is independent of the sliding speed and is less than the static friction. The true contact area is different from the bulk contact area due to the asperities on the surfaces. The smoother the surfaces, the larger will be the contact area.

2. Wear

Wear is the gradual removal of material from contacting surfaces in relative motion. In joint implants, the wear debris and hence the extent of wear of articulating surfaces is an important factor in their success. The higher the wear resistance, the more successful is the implant.

There basic modes of wear are [61]

- Abrasive wear, in which the ploughing effect of hard particles on one surface causes the removal of particles of equal or lower hardness form a contacting surface.
- Adhesive wear, in which particles on one contacting surface sticks to the other surface and are torn off due to the sliding motion.
- Erosive wear, in which wear takes place as a consequence of impact of particles of solid or liquid on a surface.
- Cavitation wear, in which cyclic formation and collapse of bubbles on a surface in contact with a fluid, causes wear in the form of a series of holes or pits.
- Fatigue wear, in which a variety of cyclic events initiates and propagates cracks. The cracks eventually cause a layer of material near the surface that is ejected as debris.
- Fretting wear, in which wear takes place due to vibration of contacting surfaces or particles at small amplitudes (~1μm)
- Tribochemical wear, in which there is a combined effect of mechanical, chemical and thermal processes occurring at the interface. The corrosiveness or reactivity of

the environment is generally enhanced due to these mechanical and thermal processes. Figure 1.5 illustrates the different modes of wear.

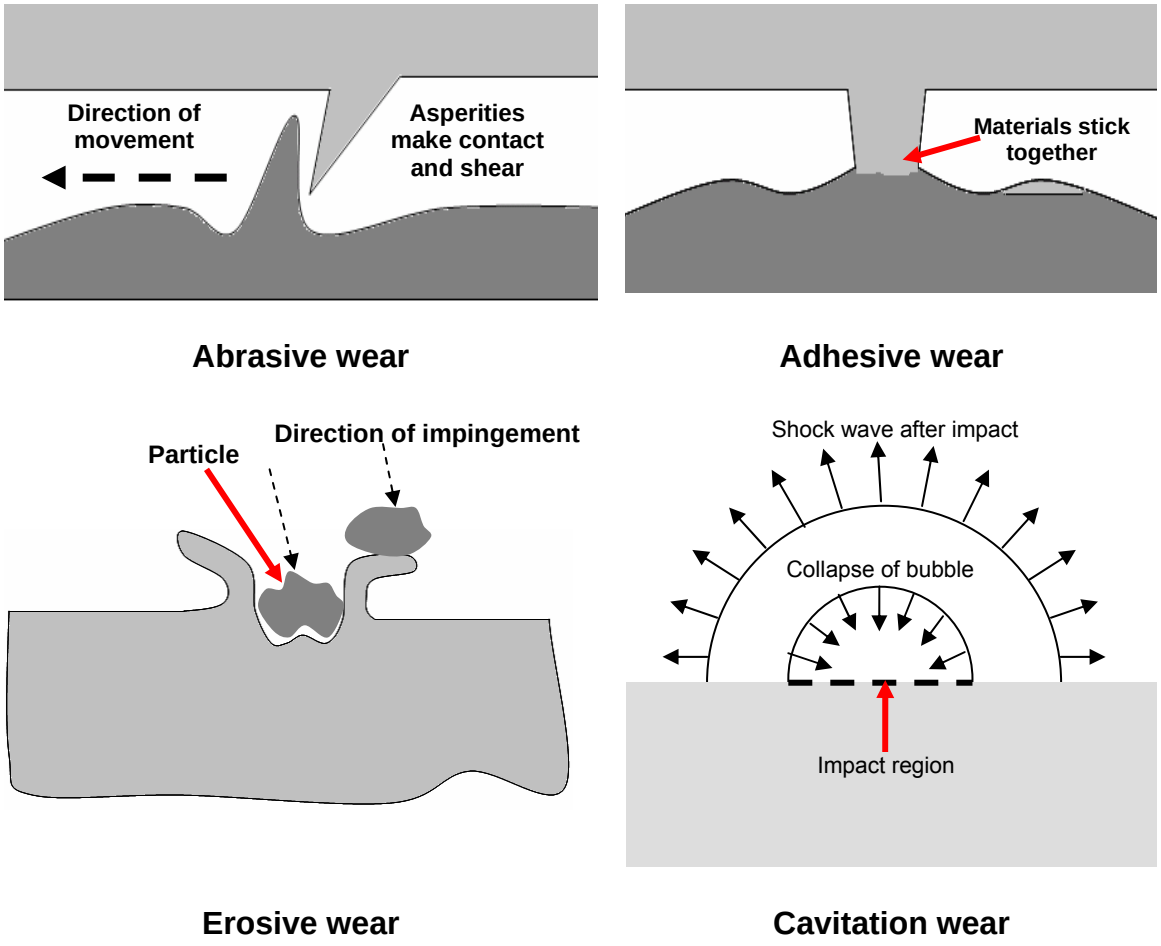

FIG. 1.5. Different wear modes

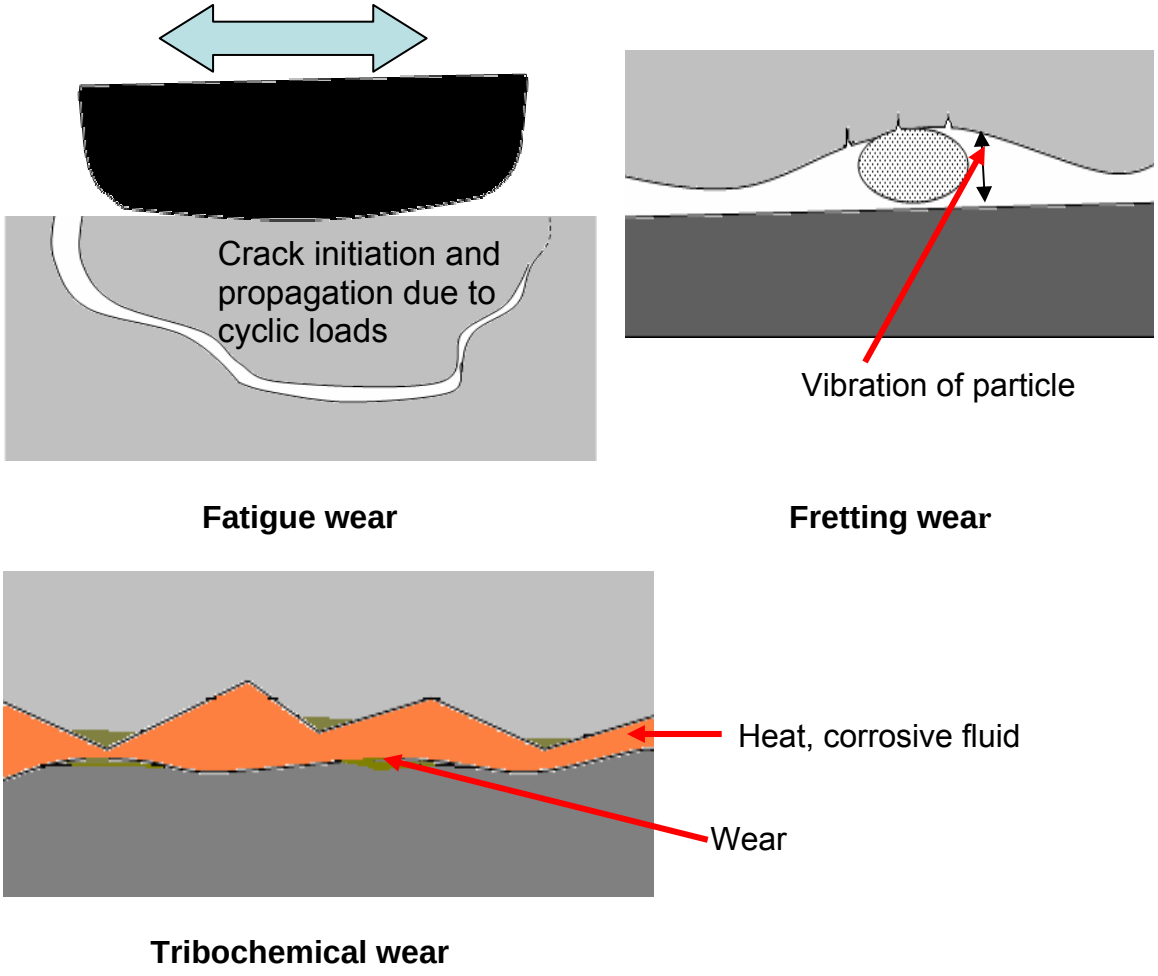

FIG.1.5. (continued)

3. Lubrication

Lubrication is the process of making a surface smooth or slippery and reducing the coefficient of friction. There are two basic types of lubrication.

Boundary lubrication: In this form of lubrication, there is adsorption of a single monolayer of lubricant on each surface [62]. This prevents direct surface to surface contact at an articulation and therefore minimizes wear (Fig. 1.6a). It is independent of the properties of the lubricating substance and the mechanical properties of the surfaces

involved. In synovial joints, it is believed that body serum albumin (BSA), in conjunction with surface-activated phosopholipid (SAP), plays the role of the adsorbed molecule [63]. The coefficient of friction in a synovial joint is about 0.01 [64].

Fluid film lubrication: This involves a thin film of lubricant which increases the separation of the bearing surfaces. Load on the bearing surfaces is supported by the pressure in the fluid film. Two forms of fluid film lubrication are (Fig. 1.6a):

- Hydrodynamic: This occurs when rigid bearing surfaces are not parallel and slide tangentially in relation to each other with the lubricant in between. A converging wedge of fluid forms as shown in Fig.1.6a. The viscosity of the lubricant within this wedge produces a lifting pressure [65].
- Squeeze film lubrication: This occurs when the bearing surfaces are moving perpendicular towards each other. The viscosity of the lubricant in the gap between the surfaces produces pressure which tends to force out the lubricant. This phenomenon provides the capability of carrying high loads for short lengths of time.

Other types of lubrication specific to synovial joints are:

- Elastohydrodynamic (Fig. 1.6b): This occurs when the bearing surfaces are not rigid. The fluid pressure deforms the soft articular surfaces (Fig.1.6b). This deformation causes an increase in the surface area of the bearing surfaces. This reduces the escape of fluid from between the surfaces and means that the lubricating film lasts longer, increasing the load bearing capacity of the surfaces.
- Weeping/Self lubrication (Fig. 1.6c): The articular cartilage is filled with fluid, is porous and permeable and capable of exuding and imbibing lubrication fluid [66]. As joint surfaces slide over one another, fluid is exuded by the cartilage in front of and beneath the leading half of the moving load. When pressures and strains are low, the articular catrilage is most permeable and the cartilage imbibes lubricating fluid. As they increase, the cartilage is less permeable and fluid is exuded.
- Boosted lubrication (Fig. 1.6c): During prolonged periods of standing, the fluid film tends to disappear due to the squeeze film mechanism. However lubrication is

maintained by boundary lubrication and ultrafiltrated Hyaluronic acid macromolecules [67]. This is called boosted lubrication.

The joint space is filled with a fluid called 'synovial' fluid. It is slightly yellow and viscid [48]. It is secreted by the synovial membrane that surrounds the joint. The quantity of synovial fluid in the knee joint of a man may be as little as 0.2 ml [68]. The fluid is a diasylate of blood plasma and contains electrolytes, cells, protein and mucopolysaccarides. It also contains hyaluronic acid with a high molecular weight (approximately 1.10 million) [69], which imparts a non-Newtonian viscosity to the fluid. Fluids from osteoarthritic joints have a more Newtonian behavior. In a total joint replacement, part of the synovial membrane is sometimes removed, to accommodate the implant, and therefore the quantity of synovial fluid secreted is reduced. The predominant lubrication modes are boundary and mixed [70]. Proteins in the synovial fluid have an impact on the lubrication of natural and artificial joints. The goals of this thesis work are:

- To investigate refractory metals and their coated counterparts as substitutes for currently used metals in joint replacements
- Develop biomimetic and biocompatible polymeric composite materials that could possibly replace damaged cartilage without the necessity of a total joint replacement.

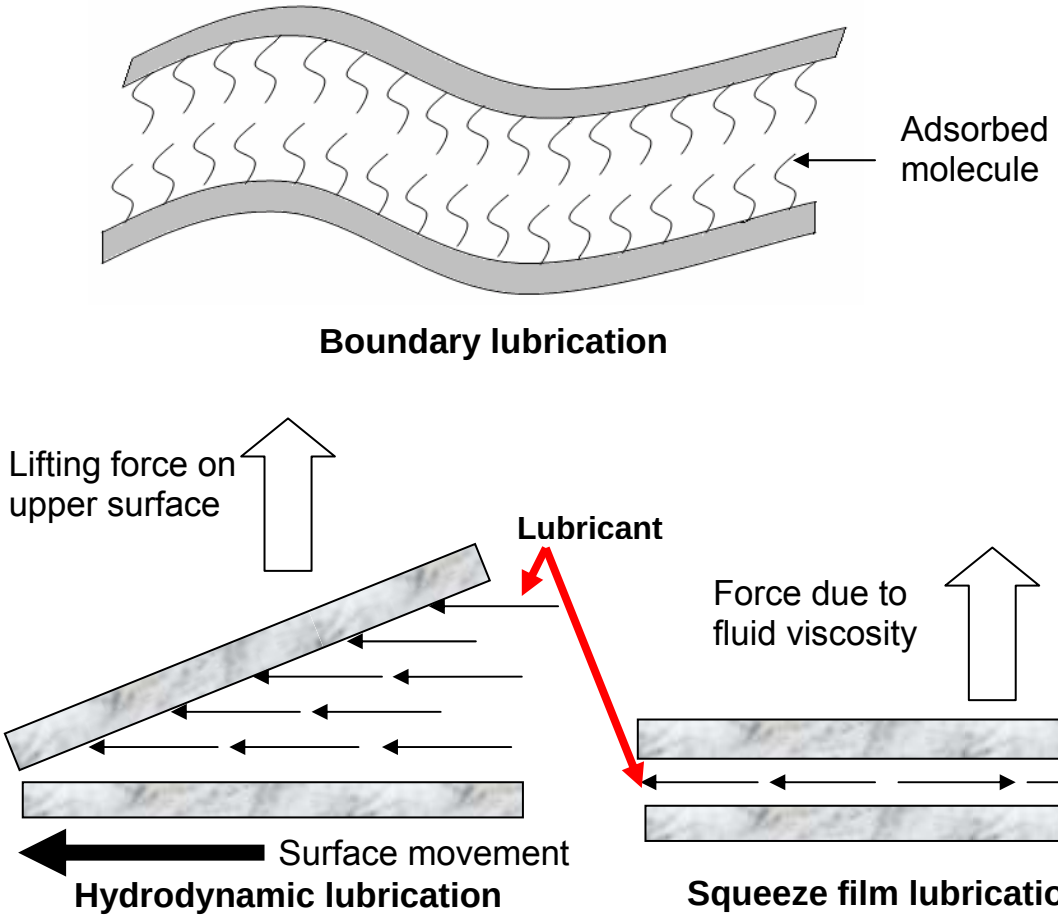

FIG. 1.6. Lubrication modes

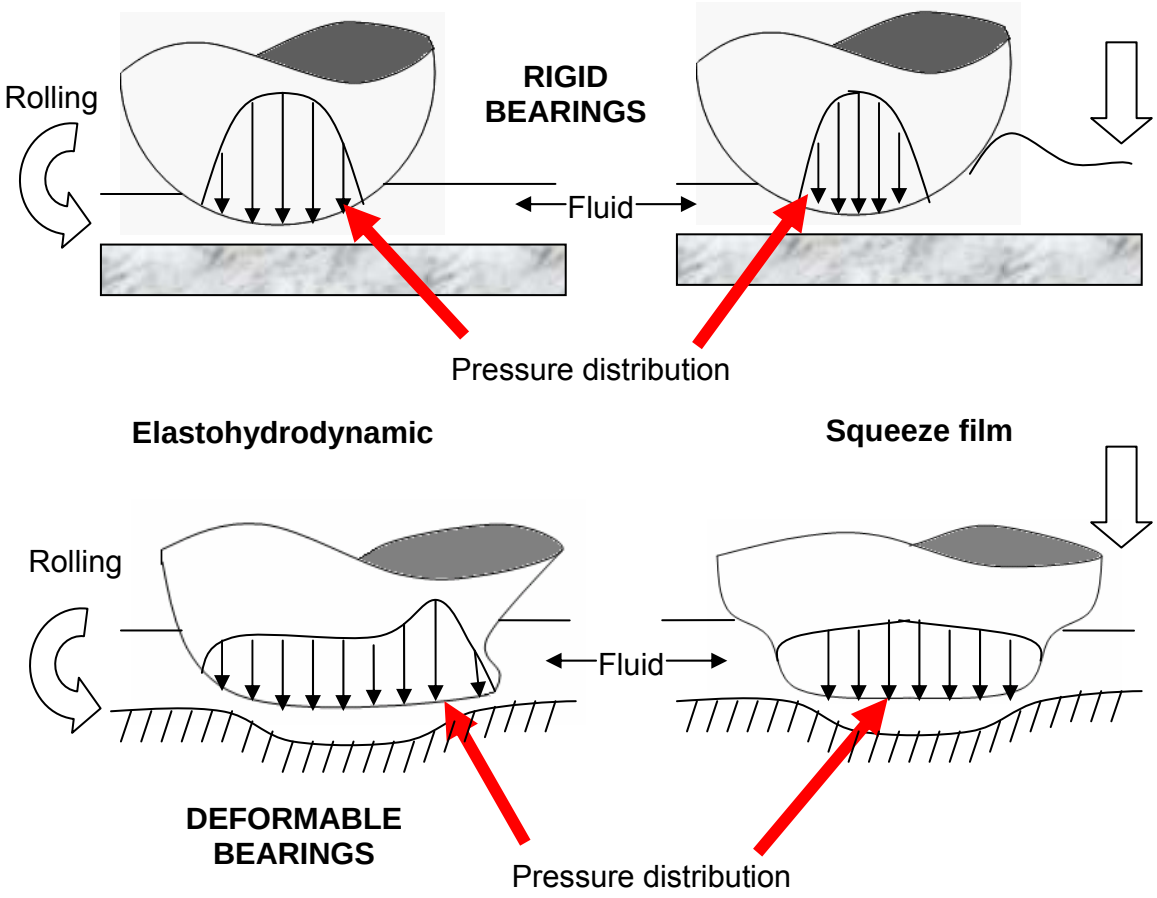

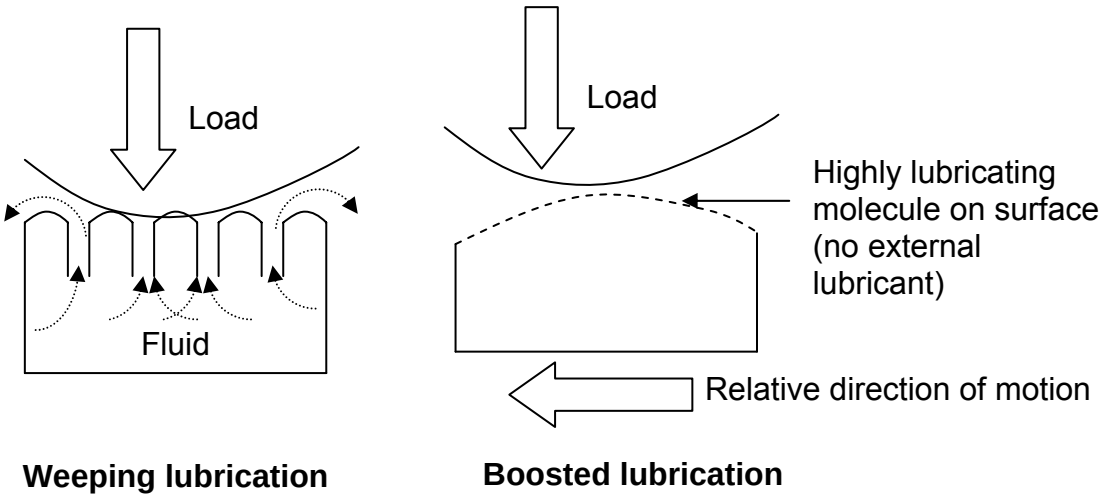

FIG. 1.6 (continued)

CHAPTER II

MOTIVATION AND APPROACH

A. INCREASING LIFE OF JOINT PROSTHESES

The effects of wear and unnatural functional restoration provided by artificial joints are a major concern. The debris particles from the articulating surface lead to biological as well as mechanical complications. A lack of biomimetic behavior causes severe discomfort and immobility to the patient.

One of the most common causes of total joint failure is prosthesis loosening [71]. Causes of loosening may be septic (related to infection) or aseptic (sometimes called mechanical loosening) [72]. Loosening causes severe pain to the patient and the implant needs to be replaced, a procedure known as revision. Septic loosening can be caused due to skin or airborne microsorganisms introduced during surgery and also due to the nature of the implant material [73-75]. Factors that can lead to mechanical loosening are bone necrosis, mechanical damage, wear debris effects and fatigue caused at the bone-implant interface due to usage over time [76-79].

Current prostheses made of synthetic materials such as stainless steel, titanium alloy, polymers, and ceramic composites, undergo degradation after 10-15 years of use. Assuming that the wear debris is non-toxic, three possible reactions from the body immune system may occur [80]. They are

i) The macrophage cells would try to digest the particles by releasing chemicals and enzymes to dissolve them, and later attempt to absorb the by products.

The by products would then be eliminated through the blood circulation and lymphatic systems.

ii) If the process in i) fails, the body would try and excrete the particles without dissolving them.

iii) If both i) and ii) fail, cellular fibrous linings are formed that surround the foreign particles, so as to isolate them from the surrounding tissue.

Scenario iii) can decrease the interfacial strength between the implant and tissue and give rise to micro-motion and fretting. The detailed mechanisms of fatigue wear have been described in some references [81, 82]. These mechanisms involve surface chemistry, size, shape and surface to volume ratio of the wear debris, and the extremely hostile body environment [80].

Stainless steels used in joint replacements are composed of iron alloyed with chromium, nickel and molybdenum. The advantages of these materials are good strength, good biocompatibility, and low cost. A major disadvantage is that they can undergo slow corrosion in the body environment [83]. Another disadvantage is the high elastic modulus (~200 GPa) which is 10 times that of bone [83]. This can lead to the phenomenon of stress shielding wherein the implant bears a larger proportion of the load than bone. This leads to weakening of the bone, and decrease in bone density. Cobalt-chromium (Co-Cr) alloys are found to be stronger and more corrosion resistant than stainless steel [83]. However, the elastic modulus is slightly higher than that of stainless steels. Titanium alloys are strong, corrosion resistant and have an elastic modulus of ~110 GPa. Therefore there is less problem of stress shielding than stainless steel or Co-Cr alloys.

It has been reported that heating UHMWPE to temperatures even below its melting point can significantly alter its crystallinity and physical properties [84]. It has been found that resistance to crack propagation improves when the crystallinity increases [85]. Radiation sterilization, in the presence of air can lead to chain scission, decrease in molecular weight, increased crystallinity, oxidation, accompanied by decreased mechanical strength [86]. Crosslinking the polymer enhances the resistance to plastic flow and lamellae alignment at the articulating surface, resulting in better resistance to wear [87, 88]. However, there is a tradeoff with decreased mechanical properties that include strength, ductility, elastic modulus, fracture toughness, and crack propagation resistance [89]. In UHMWPE tibial inserts, the components are subjected to high cyclic contact stresses. This results in pitting and delamination [90]. It has been found that large-scale deformation and plasticity induced damage layers develop under the articulating surface due to sliding and high contact stresses [91].

Bone-implant cements are mostly made of polymethylmethacrylate (PMMA) [83]. Bone cement is viscoelastic and may undergo creep. It is much stronger in compression than in tension, but weakest in shear [83]. Problems related to bone cement are [92]

i) The stability of the cement depends largely on its homogeneity. This homogeneity may be disturbed by inclusions of blood and fat during the setting stage.

ii) Production of heat during polymerization can lead to necrosis of the immediate layer of bone.

iii) The rapid packing of cement into the medullary cavity of the bone may cause compression of air, fat, blood and debris into surrounding open veins. This can lead to embolism of the blood vessels.

iv) A sudden drop in blood pressure at the time of application of acrylic cement may be caused due to the toxic effects of free monomers of methylmethacrylic acid.

B. IMPROVING CARTILAGE TISSUE ENGINEERING

Although tissue engineering promises the best form of repair by generating locally grown cartilage or implanting in-vitro grown cartilage, there are certain challenges that this method faces, before being widely used.

- The new tissue grown does not have adequate mechanical strength [93, 94]
- New tissue developed does not bond well with in-vivo bone or cartilage [95, 96]

C. DEVELOPMENT OF AN ARTIFICIAL ARTICULAR CARTILAGE

Cartilage is a porous, viscoelastic composite material that contains approximately 70% by weight water. Several researchers have therefore attempted to mimic these characteristics of cartilage by investigating hydrogel and cryogel materials. These materials are porous and contain void spaces, and therefore have the ability to hold water within, similar to natural cartilage.

Oka et al [56] investigated polyvinyl alcohol hydrogel (PVA-H) for potential use as an artificial cartilage material. Histological studies showed that articular cartilage and synovial membranes around PVA-H showed neither inflammation nor degenerative changes. In addition to this, it was possible to attach the PVA-H to underlying bone using a composite osteochondral device made from titanium fibre mesh [97] It was

however found that the wear factor was approximately five times that of conventionally used UHMWPE.

Freeman et al. [98] investigated hydrogels with variable factors being applied load, lubrication, hydrogel crosslink density and degree of hydrogel hydration. They studied the characteristics of friction and wear. They found a large variation in friction coefficient from 0.05 to 1.7 while wear varied by a factor of over 60. Lubrication with water reduced the coefficient of friction by approximately 70%. High crosslink density showed lower wear. Overall, they found high complexity in the tribological processes of hydrogels in vitro.

Covert et al. [99] studied the friction characteristics of polyvinyl alcohol cryogel (PVA-c).It was found that the range of temperature and lubricants used had no impact on the coefficient of friction. Static friction was proportional to the material's stiffness and roughness. Dynamic friction was proportional to the material's stiffness and roughness and inversely proportional to the sliding velocity. Święszkowski et al. [59] improved the mechanical characteristics of a PVA-c by incorporating a cycling freezing and thawing process.

D. RESEARCH GOALS

Based on the current status of joint repair and findings behind joint repair failure, the immediate need is to identify techniques of improving the durability and lifetime of the widely used 'total joint replacements' (TJR).

The main causes of joint replacement failure are the consequences of the wear debris particles that are liberated. The problems encountered are pathological (negative

immune response) and mechanical (increased friction and wear due to particles accumulating between the articulating surfaces and invasion of the bone-implant interface causing loosening). It is therefore necessary to decrease the wear rate of articulating materials and/or allow the generation of wear particles that are more acceptable by the body and do not cause joint loosening.

The long term necessity is to do away with total joint replacements (which last 10-15 years and are irreversible), and joint cement. New treatment methods are required that would be minimally invasive and last longer, thereby reducing the discomfort of elaborate surgical procedures accompanied by irreversible loss of cartilage and bone from the bone ends. Also, current joint implant materials do not provide a complete restoration of natural joint movement. A patient feels discomfort with even the slightest change in weather conditions.

Figure 2.1 illustrates the idea behind the desired transition, from a total joint replacement to a more natural, cartilage replacement. A material that can replace natural cartilage needs to mimic cartilage, bond well with surrounding tissue and have good biocompatibility. Some of the desired properties to mimic cartilage would be viscoelasticity, deformability and recoverability, water absorption capacity, low friction on the exposed surface, surface and bulk functionality to adsorb required proteins on surface.

It was therefore proposed that this research work would

- investigate tribological characteristics of boronized refractory metals for potential replacement of currently used metals in joint arthroplasty.

- investigate the possibility of developing degradable tissue engineering materials that would be stronger and more durable.
- investigate the biomimetic behavior of selected polymeric materials for potential cartilage replacement.

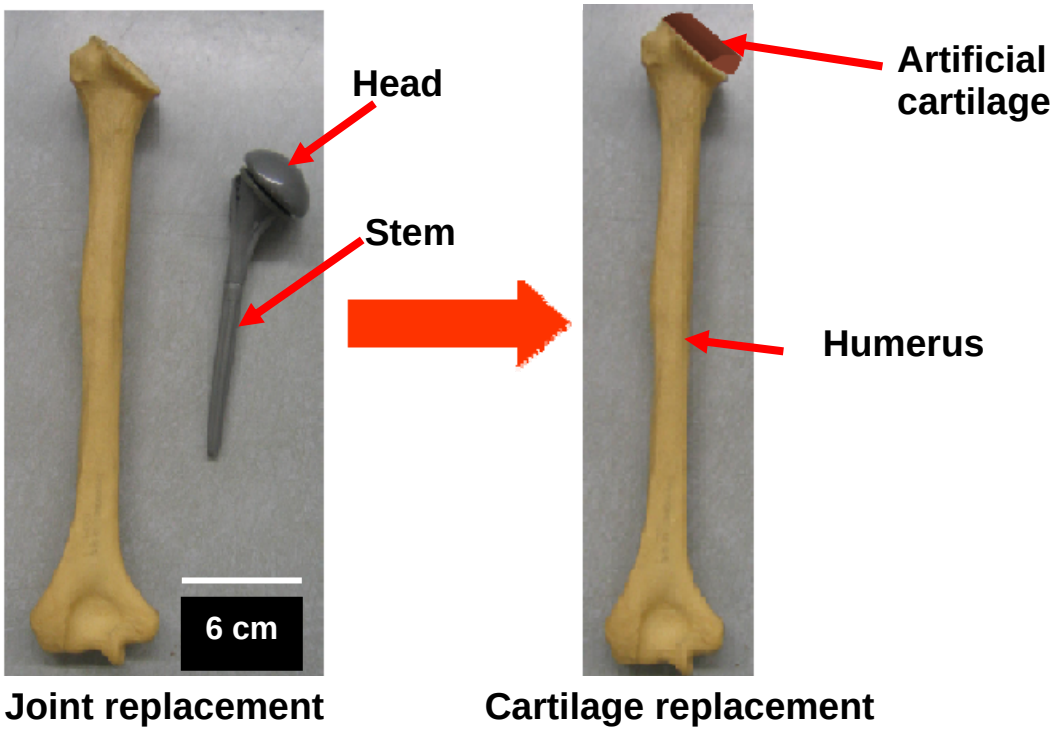

FIG. 2.1. Proposed future transition from a total joint replacement, to a cartilage replacement.

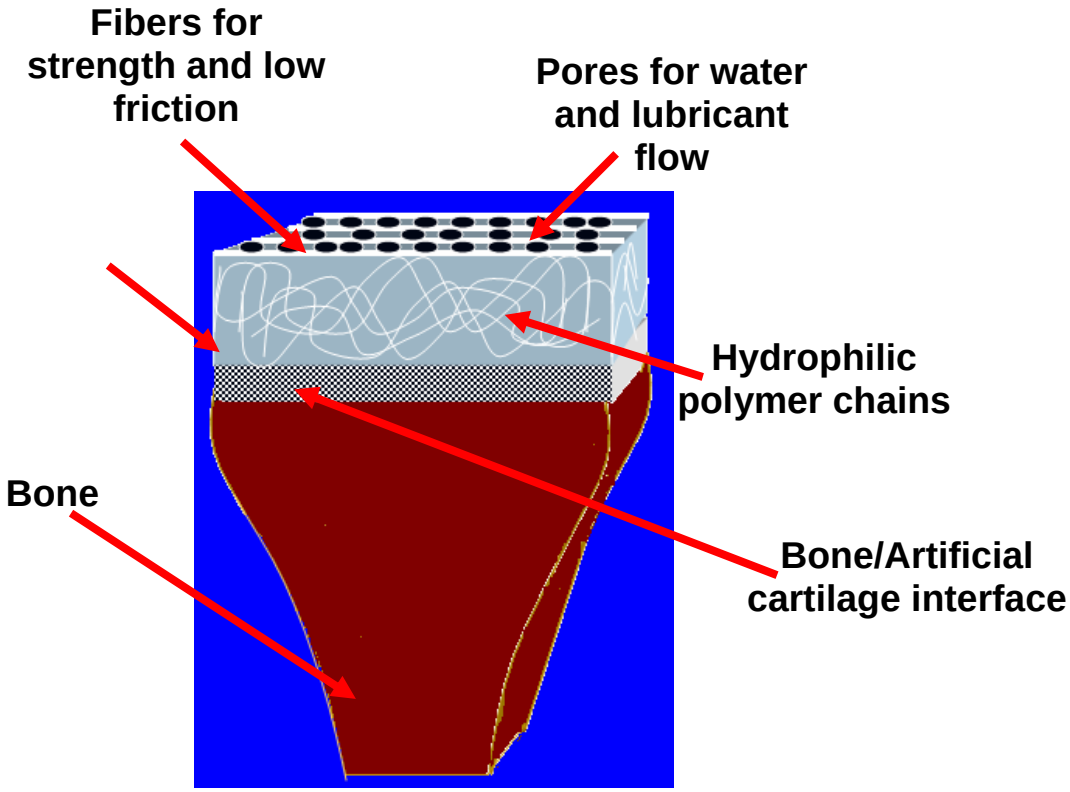

FIG. 2.2. Proposed artificial cartilage composite material affixed to bone.

E. APPROACH

The materials investigated in this research have been divided into three basic categories.

- Refractory metals and coated refractory metals (boronized and pure refractory metals)
- Polymers and polymer composites for tissue engineering (biodegradable polymers, copolymers and composites)
- Polymer composites for cartilage replacement (non biodegradable polymers and composites)

Control materials for comparison

- Ultrahigh molecular weight polyethylene (UHMWPE, which is currently used in joint implants)
- Ti6Al4V alloy (currently used in joint implants)
- Human cartilage
- Human bone

Chapter III provides information on the reasons for choice of materials and details on their properties.

Chapter IV explains the procedures adopted towards characterization of selected materials and their comparison with the control materials. The tribological and mechanical characteristics at the nano-scale level were determined and compared. The required characteristics were low friction and wear, viscoelastic response similar to cartilage.

Figure 2.2 illustrates the proposed development of an artificial cartilage material affixed to the bone. The material needs to be non biodegradable, highly wear resistant and biocompatible. In addition the viscoelastic and water absorption properties should be similar to those of natural cartilage in order to provide a more natural recovery to patients.

CHAPTER III

MATERIALS

In this chapter, materials used for this research are discussed. There are a wide variety of clinical materials used for artificial joints today. The tribology and clinical communities are particularly interested in materials that are high load bearing, corrosion resistant, biomimetic and biocompatible. This research focuses on novel, improved materials for joint repair. There were basically three material categories tested: natural cartilage and bone, metals and alloys (pure and coated), and polymers (including composites).

A. HUMAN CARTILAGE AND BONE

Cartilage is a semi-rigid form of supporting tissue [100]. The formation of cartilage commences with the differentiation of primitive mesenchymal cells to form rounded cartilage precursor cells called chondroblasts [100]. Mitotic division of chondroblats takes place followed by synthesis of ground substance and fibrous extracellular matrix [100]. Mature cartilage cells known as chondrocytes maintain the integrity of the cartilage matrix. Towards the periphery of the cartilage, chondroblasts merge with the surrounding loose supporting tissue. Growth of cartilage occurs by interstitial growth from within and appositional growth at the periphery. According to Burkitt et al. [100], the outermost layer of the cartilage is called the perichondrium and mesenchymal cells of this layer differentiate into fibroblast cells that form collagen.

Cartilage contains about 70% (by weight) water, 40%-70% collagen (dry weight) and 15%-40% proteoglycans [101]. Collagen in cartilage is predominantly of type II. The

collagen fibers are able to withstand high tensile stresses. Figure 3.1 shows the four major zones of articular cartilage. The outermost superficial tangential zone (STZ) consists of lamina splenden fibers (closely packed collagen fibrils which are ~30 nm diameter), which are aligned tangential to the surface. They act as a barrier membrane to enzymes and large molecules like hyaluronic acid, but allow glucose from the synovial fluid to enter the cartilage to nourish the chondrocyte cells. According to Martin et al. [101] gaps develop between the lamina splendens with age. Below these are thicker collagen fibers that are aligned parallel to the surface along with flat shaped chondrocyte cells. This zone has a smaller percentage of proteoglycan molecules. The next zone is the middle zone in which collagen fibers are arranged randomly. This is the thickest zone in which roundish chondrocyte cells are stacked parallel to the collagen fibers. It has the highest concentration of proteoglycan molecules. In the deep zone, there are collagen fibrils that are arranged perpendicular to the cartilage surface. Chondrocyte cells are aligned parallel to the fibril orientation. The zone adjacent and attached to the bone is known as the calcified zone.

Figure 3.2. illustrates the structure of a proteoglycan unit found in articular cartilage. It consists of a core protein, to which are attached glycosaminoglycan molecules. These are chondroitin sulphate and keratin sulphate. The core protein is attached to a hyaluronic acid chain by a link protein. The whole assembly is known as the proteoglycan aggregate or more commonly as ‘aggrecan’. The proteoglycan molecules are negatively charged and therefore, the aggrecan molecules tend to repel each other and branch out forming a bottlebrush kind of structure [101]. Due to the negative

charge, the aggrecan molecules are also hydrophilic. This causes them to attract water into the cartilage. Compressive loads are borne by cartilage tissue, as well as a large volume of water that is retained inside [101].

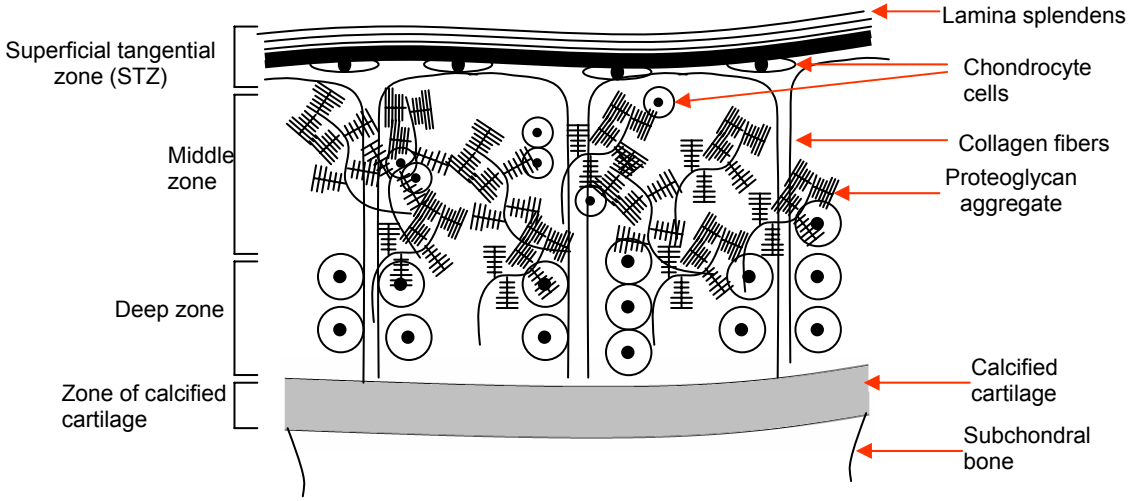

FIG. 3.1. Cartilage zones (not drawn to scale).

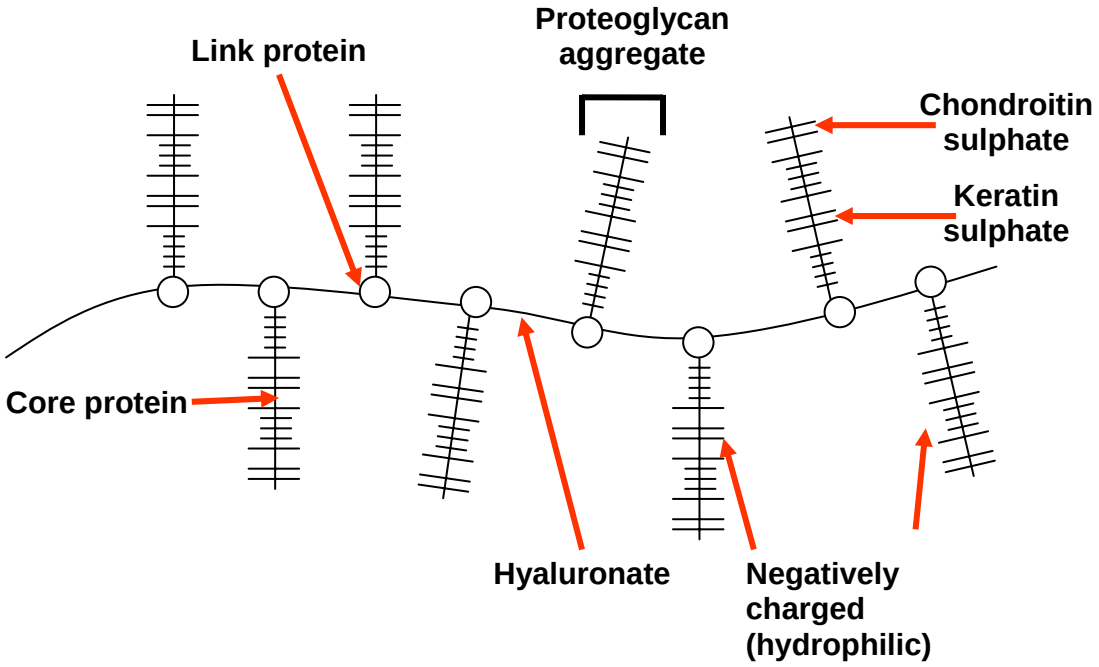

FIG. 3.2. Proteoglycan aggregate molecule

Bone is made up of 65% mineral, and 35% organic matrix, cells and water [102]. Bone mineral is made up of crystals in the shape of needles, plates and rods located within and between collagen fibers. It is made up largely of calcium hydroxyapatite with chemical formula $Ca_{10}(PO_4)_6(OH)_2$. The organic matrix consists of 90% collagen and about 10% noncollagenous proteins [103-105]. The basic structure of bone at the proximity of a joint is shown in Fig. 3.3. Articular cartilage is attached to porous cancellous bone which is in the form of a scaffolding-like structure. Cancellous bone is surrounded by a layer of cortical bone. Cortical bone is denser than cancellous bone and contains narrow channels for the passage of blood vessels.

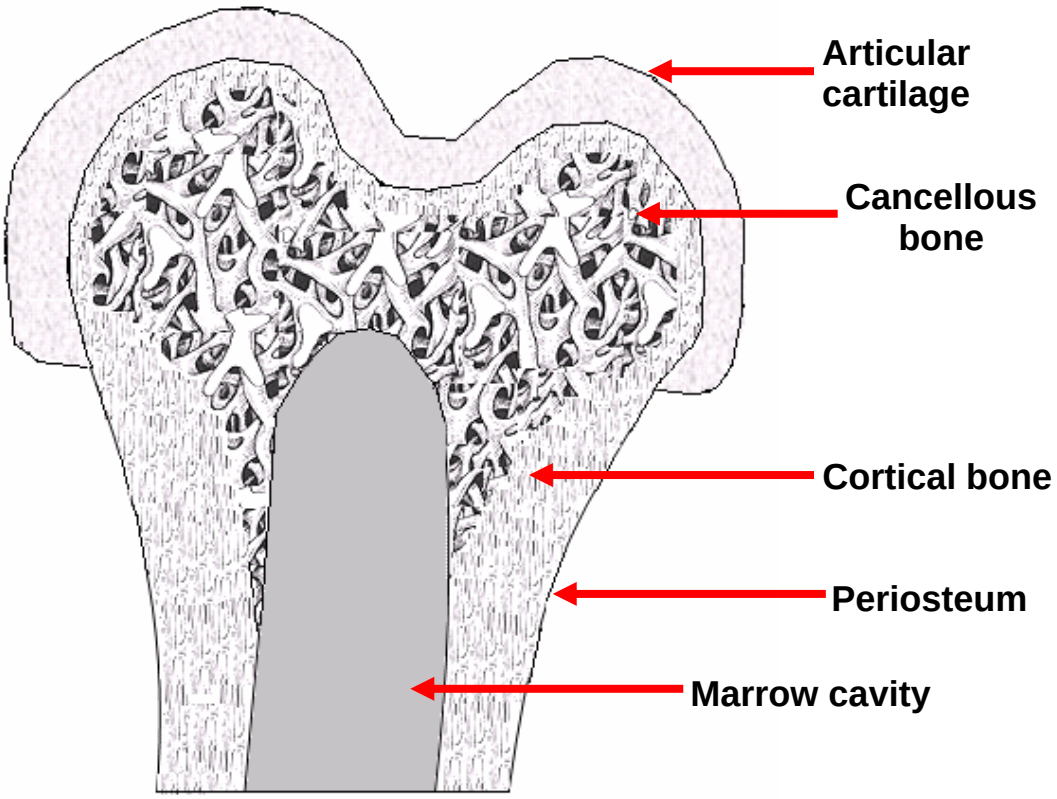

FIG. 3.3. Cross section of bone near the joint.

A human articular cartilage specimen was obtained from a 51-year old male's amputated right knee. The patient was suffering from a vascular obstructive disease in his right leg. He had no chance of living with conservative treatment because of ischemic necrosis of the foot. Therefore his leg had to be amputated above the knee. The specimens were harvested from the amputated joint using a hacksaw and scalpel blade. The specimens contained the entire thickness of cartilage and part of the subchondral bone (Fig. 3.4). Cartilage and subchondral bone obtained from near the femoral condyle was used as the pin material in the tribological tests. Cartilage (complete thickness) and subchondral bone from the tibial plateau was used as the counter material for the

cartilage-on-cartilage tests. Subchondral bone from the knee joint of the same subject from whom the cartilage was obtained, was used in these studies. The bone and cartilage specimens were stored in a deep freeze at -17 ^{o}C.

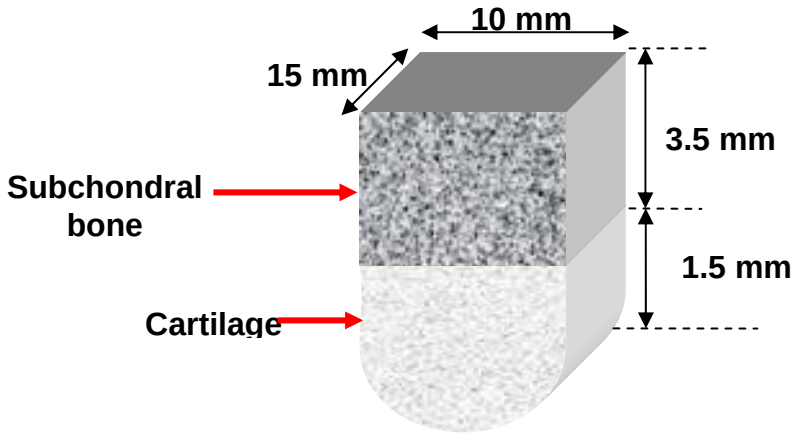

FIG 3.4. Approximate dimensions of cartilage-bone samples used in the tribotests.

Figure 3.4 shows the approximate dimensions of the specimens used. The cartilage and bone samples were defrosted at room temperature before testing. The temperature was maintained at 37 ^{o}C (body temperature) when experiments were conducted.

B. REFRACTORY METALS AND BORONIZING

Refractory metals are transition elements present in groups IVB, VB, and VIB of the periodic table. They are extraordinarily resistant to heat and corrosion [106]. Their use is found in lighting, tools, lubricants, nuclear reaction control rods, and as catalysts. Niobium (Nb), tantalum (Ta) and titanium (Ti) are refractory metals and have excellent corrosion resistance [107]. They form a passivating oxide layer on their surface that

prevents further corrosion. It has also been reported that they possess good biocompatibility [108-110]. They are therefore potential candidates for use in the corrosive body environment.

Niobium is element number 41 (atomic number) placed in group VB and period 5 in the periodic table. It is never found as a free element but exists in the minerals columbine ($(Fe,Mn)(Nb,Ta)_2O_6$), columbite-tantalite ($(Fe,Mn)(Ta,Nb)_2O_6$), pyrochlore ($(Na,Ca)_2Nb_2O_6OH,F$), and euxenite ($(Y,Ca,Ce,U,Th)(Nb,Ta,Ti)_2O_6$). It is named after 'Niobus', the daughter of the Greek mythological character 'Tantalus'. Minerals that contain niobium often also contain tantalum.

Tantalum has atomic number 73 and is in group VB and period 6 of the periodic table. It is named after Tantalus. It occurs in the same minerals as Niobium and was thought to be the same element until the two were isolated in 1844.

Chromium, with atomic number 24 is placed along with molybdenum and tungsten in group VIA of the periodic table. These elements are used extensively as alloying elements to improve on the wear and corrosion resistance of the alloys. Chromium is added as an alloying element to various metals to improve their corrosion resistance. It is used in joint replacement applications (stainless steel 316L and Co-Cr alloys).

Boronizing is a surface treatment, thermochemical process involving the diffusion of boron into a base metal at high temperature to form hard boride layers [111-113]. The resulting metallic boride provides high hardness, wear resistance, and resistance to acid corrosion [113]. The advantages of boronizing over other surface treatments are [114]:

- A very hard boride layer is formed
- The coefficient of friction is very low
- No extra heat treatment is required after boronizing
- The boride has considerable resistance to acid, base, metal solutions and high temperature oxidation.

Moreover, it has been reported that boronized steels and cast irons can resist wear and oxidation without losing their tribological properties upto a temperature of approximately 1000 ^{o}C [115, 116].

It has been found that boronizing of ferrous metal alloys form a FeB and Fe_2B phases [117-119]. FeB forms the outer layer and is hard [118]. FeB is hard and brittle whereas Fe_2B is soft and ductile [118]. It was also reported that single phase boride layers exhibited higher wear resistance than two-phase layers due to the inhomogeneous microstructure [119, 120].

The pretreatment process includes the washing of any cutting fluids and anti-corrosion oils and removal of rust films by brushing or gentle blasting with glass beads [121]. The boronizing agents of industrial importance are those based on activated boron carbide. The main constituents include the boron donor, the activator and the filler [21].

Pure niobium, tantalum and chromium (all 99.98% weight purity) made up the substrate material. Niobium and tantalum were cut into discs of dimensions approximately 6 mm diameter and 3 mm in height. Chromium was cut into a cuboid of approximate dimensions 1.1 cm x 0.7 cm x 0.5 cm. Boronizing was performed in a solid medium using Ekabor powders that had grain sizes less than 850 μm and had a nominal

chemical composition of 90% SiC, 5% B_4C and 5% KBF_4 (activator). The pretreated pure niobium and tantalum test specimens were placed in contact with Ekabor powders and then transferred to an electrical resistance furnace in a stainless steel crucible with a diameter of 5 cm and height 8 cm. This process is known as the 'pack cementation' process. Boronizing with a solid agent has advantages such as ease of treatment, forming of a smooth surface, and simplicity of equipment [14]. They were then heated from room temperature to 940 ^oC in 50 minutes under atmospheric pressure and held in the furnace for 4 hours. This was followed by cooling in air. The thickness of a boride layer depends on treatment time and temperature [18]. Sen et al [18] concluded that boride layer morphology is dominantly dendritic.

C. Ti6Al4V ALLOY AND BEARING STEEL E52100

The low density and good mechano-chemical properties of Ti make it ideal for implant applications. Alloying additives have produced even better results [122]. The alloy Ti6Al4V has been the most widely used. Aluminum (Al) is slightly lighter while vanadium (V) is slightly heavier than Ti. Therefore the density of Ti6Al4V alloy is close to that of pure Ti. It has high corrosion resistance. The elastic modulus is lower than other metallic materials used. It therefore causes less stress shielding [123]. We therefore used this material as a control material to compare its properties with those of Nb, Ta and their boronized counterparts. Ti6Al4V alloy was obtained from Goodfellow Inc. The specimens were cut into discs of 10 mm diameter and approximately 4 mm. height.

Bearing steel E52100 is a metal used extensively in tribological research. 6 mm. diameter balls of this alloy (obtained from Jelco) were used as a counter material to study the wear characteristics of Ti6Al4V alloy, Nb, Ta, and boronized Nb and Ta.

D. BIOCOMPATIBLE POLYMERS AND THEIR CHARACTERISTICS

Several polymers have been accepted for use in medical devices. Some of them are biodegradable (dissolve in the body over a period of time) and some are non biodegradable or non resorbable. UHMWPE is the most popular polymer used in joint arthroplasty due to its low friction, high impact strength, excellent toughness, low density, ease of fabrication, biocompatibility and biostability [124]. The wear debris that comes off the surface of this material is, however, the main cause for joint replacement failure due to the negative immune response that is incited. Biodegradable polymers such as polytrimethylene carbonate (PTMC), poly ε-caprolactone (PCL), poly lactide (PLA) and poly glycolic acid (PGA) are biocompatible and are resorbed within the body at a rate depending on their molecular structure [125, 126]. The bio degradability of these polymers is usually due to the hydrolytically unstable linkages in their backbone. Their applications include nerve guides and sutures [127]. The biodegradability of certain polymers is advantageous for the following reasons.

They can be used as sutures and will degrade completely after an internal wound has healed. This would not necessitate a second surgery for their removal [128]. A bone fracture that is fixated with a rigid metallic implant has a tendency for re-fracture upon removal of the implant. This is because the bone does not carry sufficient load during the healing process to enable proper remodeling. An implant made of a biodegradable

polymer can be tailored to degrade at a rate that will slowly transfer load to the healing bone [129]. Another potential application is in drug delivery, when a particular drug is to be released in the body over a period of time. The drug which is encapsulated within the polymer is released at a predetermined rate as the polymer degrades [130, 131].

Factors that affect the mechanical properties of polymers are monomer selection, initiator selection, process conditions, and the presence of additives. These factors in turn affect the polymer's hydrophilicity, crystallinity, melting temperature, glass transition temperature (T_g), molecular weight and its distribution, end groups, sequence distribution, and the presence of additives [132].

Biodegradation takes place in polymers that have backbone linkages that are hydrolytically unstable. The most common functional groups of this type are esters, anhydrides, orthoesters, and amides [128]. The chemical structure of PTMC is illustrated in Fig. 3.5. It has an ester group incorporated in its backbone. Zhang et al. [133] found that high molecular weight PTMC (Mn = 316 x 10^3 g/mol) did not degrade in phosphate buffered saline whereas subcutaneous implantation caused rapid degradation. They concluded that enzymatic degradation plays an important role in the surface erosion of PTMC in vivo. Ali et al. [134] reported that chemical attack on the amorphous phase of a polymer is more rapid than on the crystalline phase. Engelberg et al. [135] have reported that PTMC and PCL degrade at a rate slower than other biodegradable polymers. Moreover, at physiological temperature they are above their T_gs and therefore are in a rubbery and deformable state. These properties are promising for their use as tissue

engineering constructs for cartilage repair (cartilage being deformable and the polymers being suitable as scaffolds for the growth of chondrocyte cells) [136].

Polyimides have been widely used in the fabrication of aircraft structures and microelectronic devices [137]. They perform well under high temperatures, radiation and heavy mechanical loads [138]. In addition they also exhibit high wear resistance, low friction, high strength and toughness and dimensional stability [35]. Richardson et al. [139] reported that polyimides exhibited no cytotoxic response and little haemolysis. Moreover the polyimides adsorbed large amounts of body serum albumin (BSA) and fribrinogen. They also showed excellent film forming ability, electrical properties and sterilizability. Cai et al. [140] reported that PI/CNT nanocomposites exhibited lower friction than pristine PI. CNT as a reinforcing agent also contributed to restrain the adhesion and scuffing of the PI matrix. These reports indicate promise that PI/CNT composites could replace UHMWPE as a joint replacement material. The basic structure of a polyimide is shown in Fig. 3.6. R, R' and R" are organic groups.

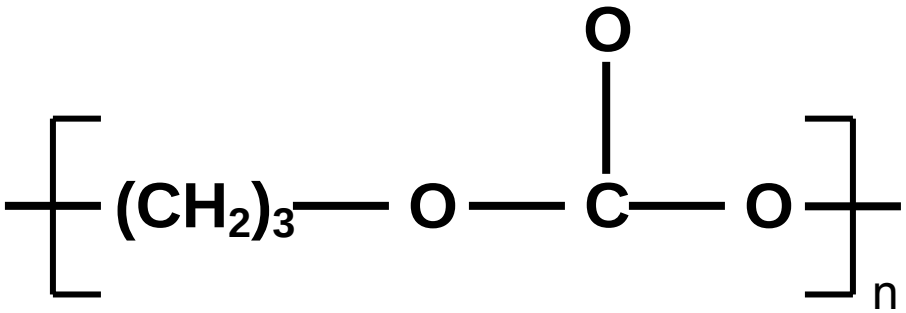

FIG. 3.5. Chemical structure of polytrimethylene carbonate (PTMC).

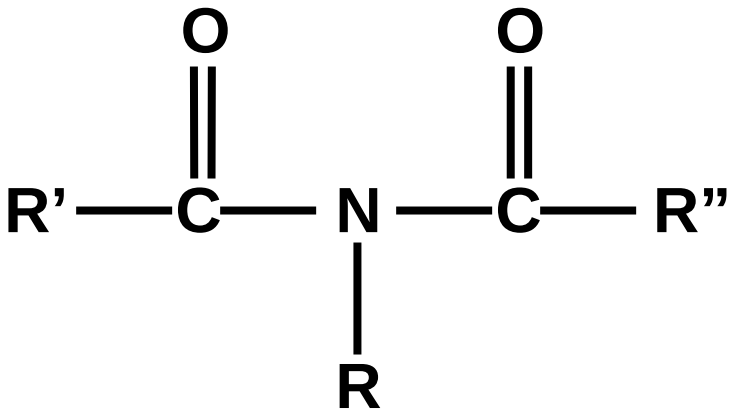

FIG. 3.6. Chemical structure of polyimide.

A carbon nanotube is made up of a graphite sheet that is rolled into a cylinder (Fig. 3.7). The ends of the sheet are joined by making the carbon atoms react. The cylindrical diameter is in the range of 0.4-2 nm [141]. A single walled carbon nanotube (SWNT) is made up of a single cylindrical graphite sheet, whereas a multi-walled carbon nanotube (MWNT) is made up of concentric cylinders of graphite. Carbon nanotubes possess high tensile strength, ultra-light weight and have excellent thermal and chemical stability [141]. Carbon based materials have been widely used as biomaterials [142-144]. Carbon nanotubes are therefore a potential candidate for being used as a multifunctional material in biomaterial composites. The mechanical strength can provide reinforcement similar to collagen fibers and functionalization of the CNT surface can vary attractive and reactive forces within and on the surface of the composite materials.

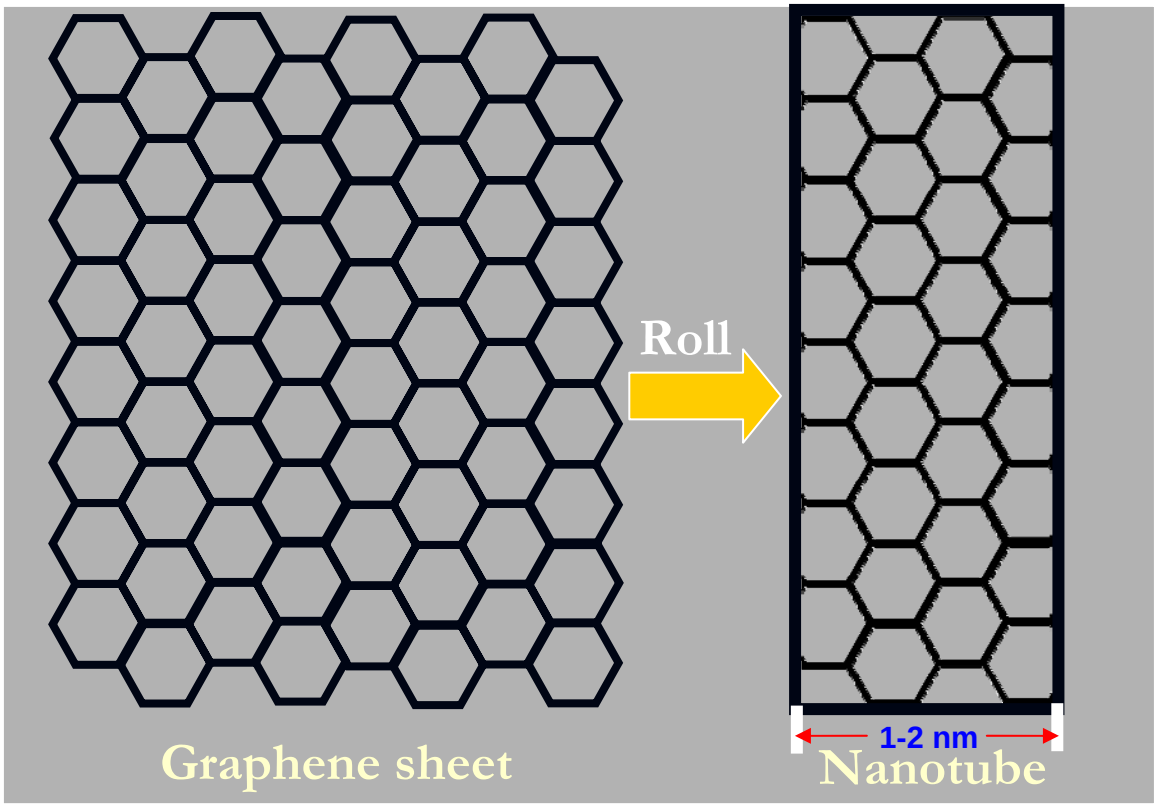

FIG 3.7. Schematic of carbon nanotube synthesis.

Monomer Trimethylene carbonate (TMC) was obtained from Boehringer Ingelheim. It was polymerized by the method of ring opening of the monomer units. The catalyst was N,N'-bis(3,5-di-tert-butylsalicylidene)-1,2-ethylenediimine Ca(II). The co-catalyst was $[Bu_4N]^+N_3$. Polymerization was conducted at 86 ^oC for 2 hours. The monomer:catalyst:co-catalyst molar ratio was 350:1:1. More information on the polymerization process can be found in a publication by Darensbourg et al. [145]. Polytrimethylene carbonate (PTMC) was physically combined with multi walled carbon nanotubes and hydroxyapatite (HAP) (Sigma Aldrich) powder to form a composite

material for potential cartilage tissue engineering. The proportion of constituents, PTMC:HAP:MWNT was 500:5:1 by weight

Polyimide was synthesized by reacting 2, 6 Bis (3 amino phenoxybonzo nitrile) (βCN-APB) with 4, 4, oxydiphthalic anhydride (ODPA). They were initially dissolved in a solvent N, N-dimethylacetamide (DMAC). The product formed was polyamic acid. Figure 3.7 illustrates the polymerization process. On heating, water was liberated from the polyamic acid, forming the polyimide product. Hipco processed SWNT's were obtained from Carbon Nanotechnologies Inc. The details on the polymerization and composite preparation can be found in a reference [146]. Polyimide was combined with single walled carbon nanotubes. Samples were prepared with different nanotube concentrations (0.035%, 0.05%, 0.075%, 0.1%, 0.2%, 0.5%, 1%, 2%, and 5% by weight).

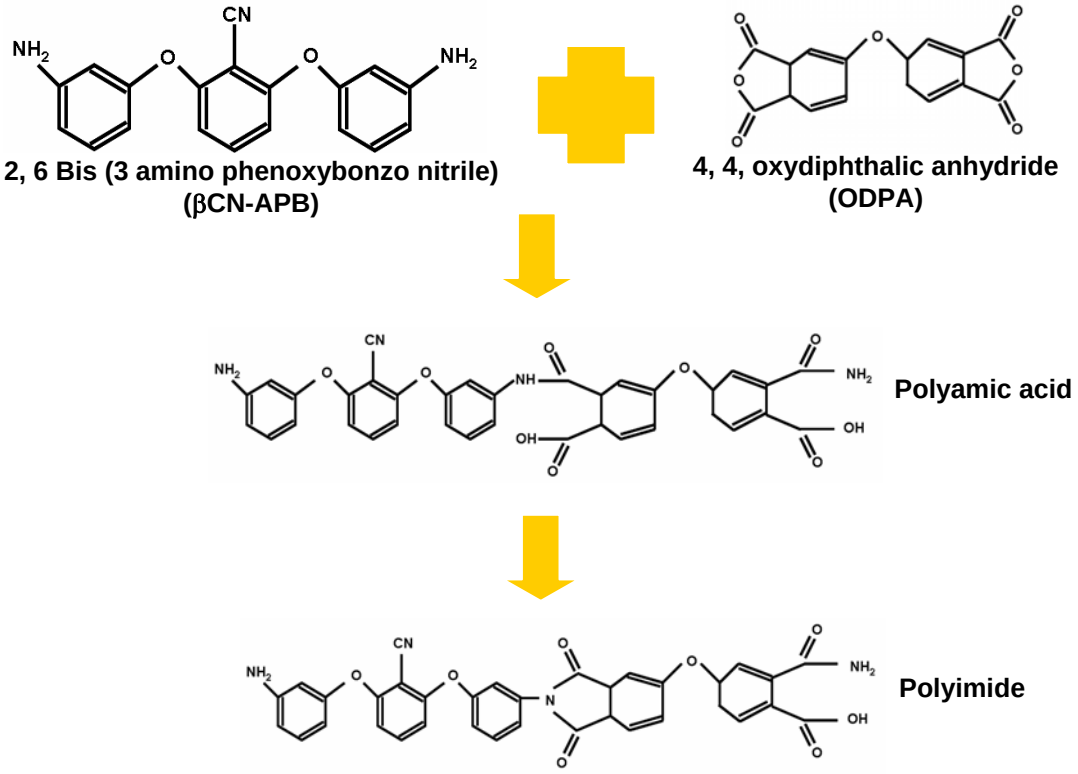

FIG. 3.8 Synthesis of polyimide.

Ultrahigh molecular weight polyethylene (UHMWPE) was obtained from Goodfellow in processed form. It is a semi-crystalline, whitish and effectively opaque engineering thermoplastic which, chemically, has a very high molecular weight (3-6 million) [147]. As a result it has an extremely high (effectively infinite) melt viscosity and can only be processed by powder sintering methods. It also has outstanding toughness, cut and wear resistance and very good chemical resistance. Specimens were cut into rectangular plates approximately 10 mm (length) x 10 mm (width) x 2mm (height). It was used as a control material to compare properties with novel polymer materials.

E. SIMULATED SYNOVIAL FLUID (SSF)

Initially, a solution of simulated body fluid (SBF) was prepared. The ionic composition of SBF is given in Table 3.1**.** This liquid solution was originally prepared by Dr. Tadashi Kokubo [148]. It was buffered at a pH of 7.25 with Tris (hydroxymethyl) aminomethane and HCl. It has a composition similar to human blood plasma. The method of preparation of 1000 mL of SBF is as follows [149].

1. Dissolution of chemicals
   i) Using a 100 ml beaker, heat 700ml of ion exchange water to 36.5 ^{o}C, stirring continuously with a magnetic stirrer.
   ii) Combine the first nine chemical from Table 3.2, according to the amounts shown.
2. Adjustment of pH
   i) Calibrate a pH meter with fresh standard buffer solutions.
   ii) After the first nine chemicals are added, confirm that the temperature is at 36.5 ^{o}C and titrate the 1M HCl solution with a pipette to adjust the pH to 7.25.
   iii) After adjusting the pH, transfer the solution to a 1000 mL volumetric flask.
   iv) Add ion-exchange water to the flask until the total volume is 1000 mL and allow the solution to cool to room temperature. Once cooled, add more ion-exchanged water to achieve 1000 mL of solution.
   v) The SBF should be stored in a refrigerator at 5-10 ^{o}C.

TABLE 3.1. Ionic concentrations in SBF.

Ion	Concentration (mM)
Na^+	142.0
K^+	5.0
Mg^{2+}	1.5
Ca^{2+}	2.5
Cl^-	147.8
HCO^{3-}	4.2
HPO^{4-}	1.0
SO_4^{2-}	0.5

TABLE 3.2. Chemicals included in SBF.

Chemical	Quantity
NaCl	7.996 g
$NaHCO_3$	0.35 g
KCl	0.22 g
K_2HPO_4	0.174 g
$MgCl_2.2H_2O$	0.305 g
1M HCl aqueous solution	~40 ml
$CaCl_2.2H_2O$	0.368 g
Na_2SO_4	0.071 g
Tris(hydroxymethyl)aminomethane	6.057 g
1M HCl aqueous solution	~10 ml

The concentration of hyaluronic acid in synovial fluid has been reported as 0.1 to 5 mg/ml [19]. Based on this, a concentration of 3 mg of hyaluronic acid (Rexall Inc., Boca Raton, FL) was added per ml of SBF. The mixture was then sonicated for 10 minutes to disperse the hyaluronic acid particles in the fluid. The resulting fluid was stored in a refrigerator at 3 ^oC. This solution was applied between the articulating surfaces before the tests were started.

CHAPTER IV

EXPERIMENTAL TECHNIQUES

A. FRICTION

A pin-on-flat tribometer configuration is illustrated in Fig.4.1, one test material is held vertically over the other. One material is attached to a shaft known as the pin. The counter material is attached to a reciprocating stage, vertically below the pin. The pin is attached to a beam which is connected to a transducer. When the stage moves back and forth, the friction force between the two surfaces is sensed by the transducer and is recorded by a computer. A fixed, predetermined vertical load is mounted on top of the pin. The computer divides the friction force by the applied vertical load (which is fed into the computer prior to starting the test). This quotient is known as the coefficient of friction and is usually denoted by 'μ'. The computer exhibits a plot of the coefficient of friction as a function of time or number of cycles. The parameters that can be varied are the distance of sliding, the speed of sliding and the duration of the test. These values are fed into the computer prior to starting the test and remain constant throughout the test. Since the objective of the experiments was to compare different materials, this simple setup served the purpose.

In this study, a CSM tribometer was used in the pin-on-flat configuration, for the tribo-tests. Temperature was controlled with a heater attached to the reciprocating stage (Fig. 4.1). The motion was linear reciprocating. The distance of travel, number of cycles, and speed were adjustable. The coefficient of friction against the number of cycles and

time was plotted using TriboX software (CSM Instruments), as the experiments progressed.

Tests were conducted incorporating different values for different parameters, depending on the material and information required. For tests with plastic and cartilage samples, the amplitude of linear reciprocating motion was 3 mm and speed of movement was 1.5 cm/s, in order to simulate natural joint motion. For severe wear tests of boronized chromium, niobium and tantalum, the amplitude was 1mm and speed was 2.5 cm/s.

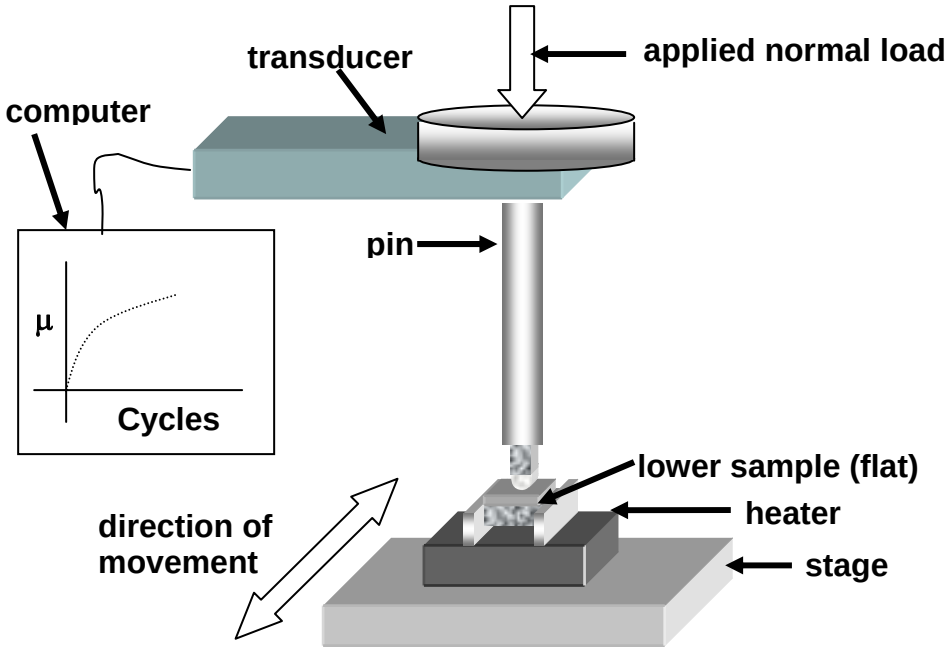

FIG. 4.1. Schematic of tribometer tests.

B. DEBRIS CHARACTERIZATION

In a transmission electron microscope, a beam of electrons is passed through a thin section of the specimen. There can be three possible fates for these electrons [150]. They are i) Transmitted through the specimen without any interaction (undeflected), ii) Deflected but loses no energy (elastically scattered), and iii) Loses energy and is deflected (inelastically scattered). Electrons with minimum interaction with the specimen have higher energy when collected by the detector. The image output from the detector therefore shows these parts of the sample as brighter. The final image is therefore a black and white image (with different shades) of the part of the sample through which the beam of electrons travels.

Images and diffraction patterns of wear particles obtained from the friction tests were obtained with a transmission electron microscope (TEM, JEOL 2010). The operating voltage was 200 kV. Samples for testing were collected in the form of wear particles from the specimen wear tracks after the tribo-tests. The particles were mixed in acetone and dispersed by placing the solution in a sonicator for 10 minutes. A drop of this solution was then applied onto a 300 to 400 mesh copper, carbon stabilized, formvar TEM test grid. The acetone was allowed to evaporate, leaving behind the debris.

Figure 4.2 illustrates the schematic of a transmission electron microscope. The source of the electron beam is called the electron 'gun' which is made up of a filament of tungsten or lanthanum hexaboride (LaB_6). A high voltage (~50-300kV) is applied across the filament along with a DC current. The resulting energy generated in the filament is absorbed by the resident electrons, which are then able to escape from their atoms, and

form an ejected beam from the filament. Another type of gun is the field emission type in which the cathode is in the form of a very sharp tip (100 nm diameter or less). When the cathode is held at a negative potential with respect to the anode, the electric field at the tip becomes very strong (> 10^7 V/cm). As a result, a tunneling electron current passes out of the cathode, through the barrier. A beam intensity hundreds of times higher than that of thermionic emission can be obtained. This type of cathode is usually made of tungsten due to the very high mechanical stresses at the tip. A cuplike structure surrounds the filament and is known as the shield or Wehnelt cylinder [151]. A slight negative potential (greater than the filament potential) is applied to the shield so that it repels the electrons, causing them to shape into a beam that is directed towards the specimen. The anode is an electromagnetic coil that draws the electrons from the gun. The lenses are electromagnetic coils, the strengths of which can be controlled by the amount of current passed through them. The magnetic field strengths produced by them are used to deflect the electron beam. The first condenser lens is a demagnifying lens that decreases the size of the beam spot while the second condenser lens increases the size. The overall effect of both lenses is to precisely control the amount of electron irradiation striking the specimen. The condenser aperture controls the intensity of the beam by blocking off part of the beam. The condenser stigmator is meant to compensate for astigmatism in the beam and to create a circular beam profile at the specimen. The objective lens forms the initial image that is further magnified by the other imaging lenses. It is used to focus and magnify the image. The intermediate lens is also used to magnify the image in the normal imaging mode. A diffraction pattern of the specimen is

formed in the back focal plane of the objective lens. By changing the excitation of the intermediate lens coils, a magnified image of the diffraction pattern can be sent to the projector system. The projector lens is used to further magnify the image from the intermediate lens. The final image is captured on a fluorescent plate or film negative. The whole microscope column is maintained under high vacuum by air pumps, in order to minimize interaction of air molecules with the electron beam.

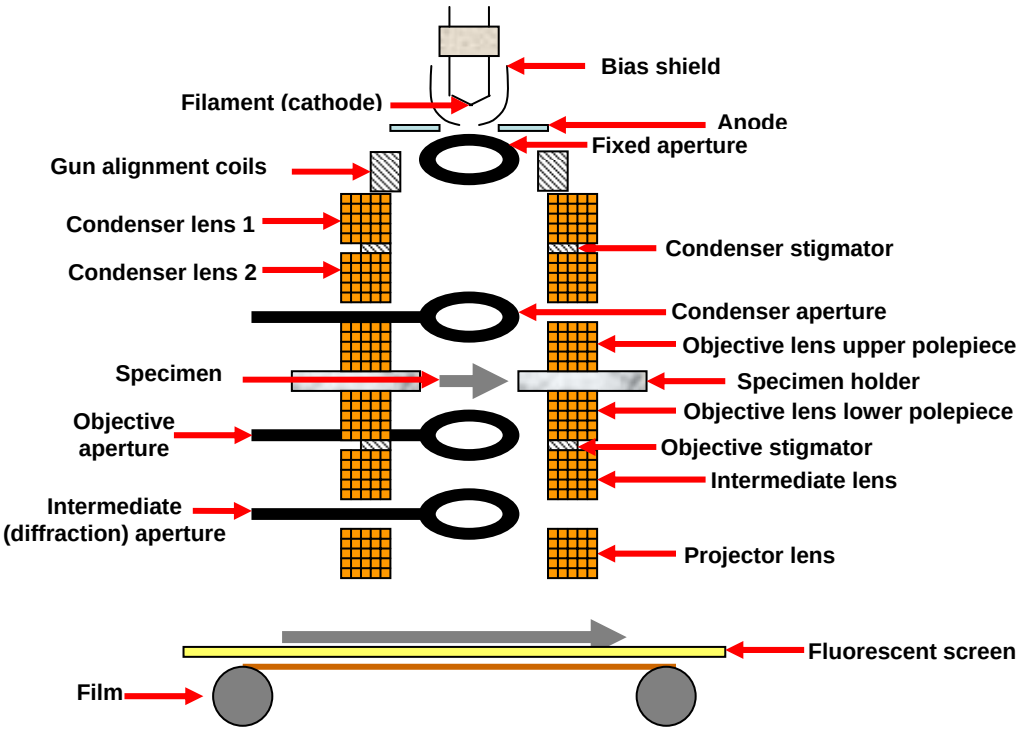

FIG. 4.2. Schematic of a transmission electron microscope (TEM).

C. SURFACE CHARACTERIZATION

An atomic force microscope consists of a physical probe (with diameter approximately 10 nm) that scans the surface of a specimen (Fig. 4.3). It scans the surface in two perpendicular directions (usually horizontal called X and Y directions). It can also move vertically (Z direction) following the height of asperities on the specimen surface. It therefore gives a three dimensional image of the surface. The nanometer range resolution of motion is achieved using piezoelectric controllers. Higher positions on the surface are indicated in a bright shade while lower positions, in a darker shade. In contact mode, the probe physically touches the surface of the specimen.

As shown in Fig. 4.3a and b, the probe is fixed to a flexible cantilever that is fitted onto a base plate. This assembly is mounted onto a movable stage that enables the scanning motion. A laser reflects off the top of the cantilever and the movement of the probe on the surface is therefore transferred to the reflected laser beam that is captured by a detector. This movement is then amplified by a computer and the output is shown as an image on a computer monitor. In contact mode of operation, the probe can be moved towards and away from the sample through a short distance, during which the force of attraction or repulsion between the surface molecules and the probe tip can be measured. Important information on surface phase characteristics can be obtained using this information.

Another mode of operation is the ‘close contact’ mode, in which the probe, along with the cantilever, is vibrated at a predetermined frequency. The probe remains close to the specimen surface but never touches it. The attractive or repulsive forces of the

surface on the probe cause a change in vibration frequency, which is detected and fed back into the computer. In order to maintain the set frequency, the amplitude of vibration is changed. This change in amplitude therefore depends on the force of attraction of the surface material on the probe, and hence on the material composition of the surface. The change in amplitude is therefore shown as a change in material composition. In this way, we can determine if there are different material phases on the surface of the specimen. Harder materials are shown in a lighter shade while softer ones show up darker. An atomic force microscope (Pacific Nanotech Inc.) was used to obtain the surface topography and phase images.

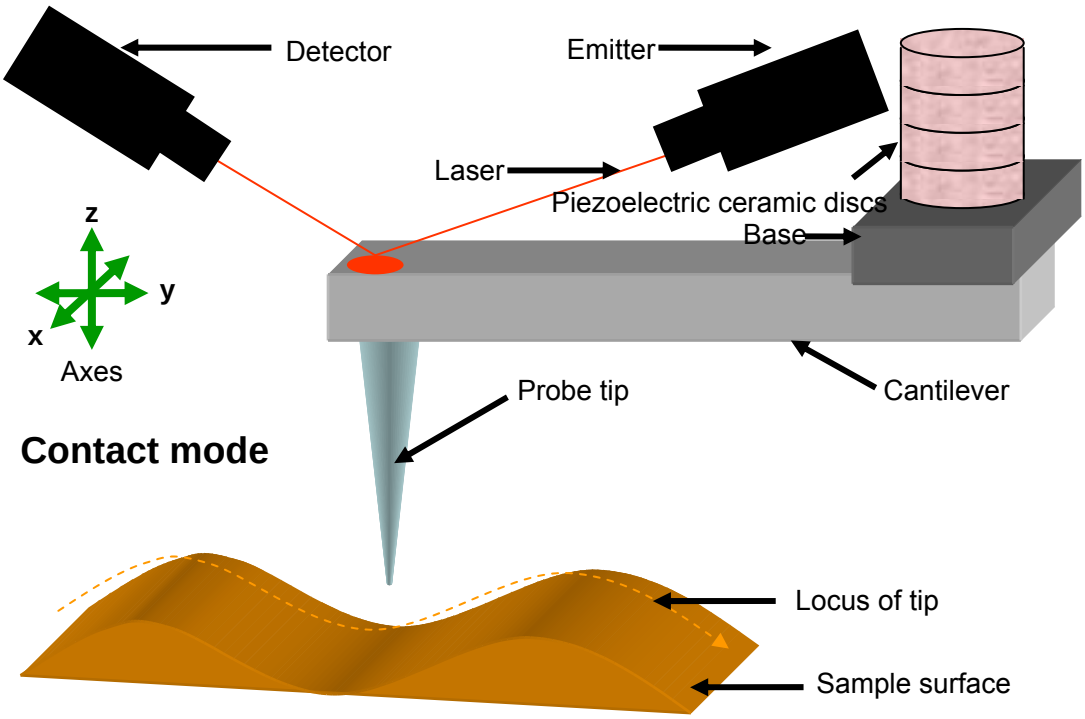

FIG. 4.3. Schematic of an AFM.

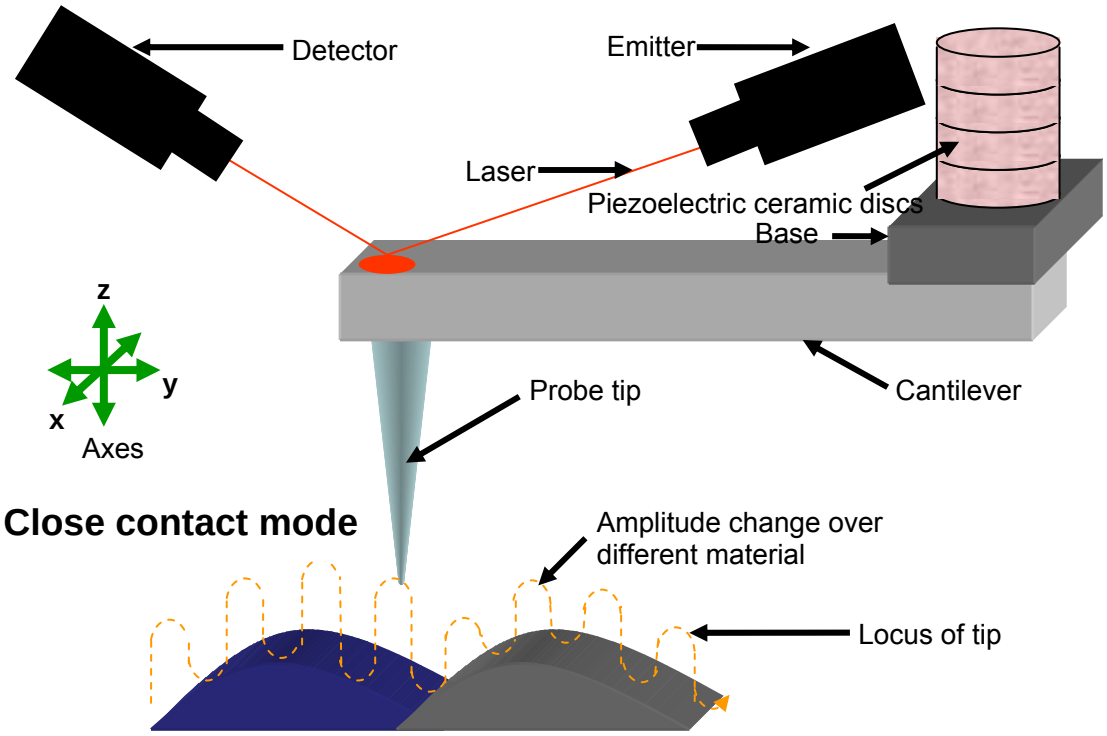

FIG. 4.3. (continued)

In a scanning electron microscope (SEM), a beam of electrons impinges on the surface of the specimen. Images of the specimen can be captured by detecting either backscattered electrons (beam electrons that are reflected back from the sample) or by detecting secondary electrons (electrons from the specimen atoms that absorb energy from the electron beam, thereby escaping from their atoms). The electrons that are obtained from higher positions on the surface lose less energy than electrons that are obtained from lower positions, and therefore show up as brighter spots in the final image.

Fig. 4.4 is an illustration of the schematic of a scanning electron microscope. The filament, bias shield, anode, gun alignment coils, apertures, condenser lenses and stigmators, are similar to those found in a TEM (described earlier). The beam passes

through the objective lens before reaching the sample. Between the condenser lens and the objective lens, there are scanning coils that cause the beam to raster along the specimen surface along parallel lines. The image signal that is captured by the detector is transformed into a graphical image and exhibited on a computer screen.

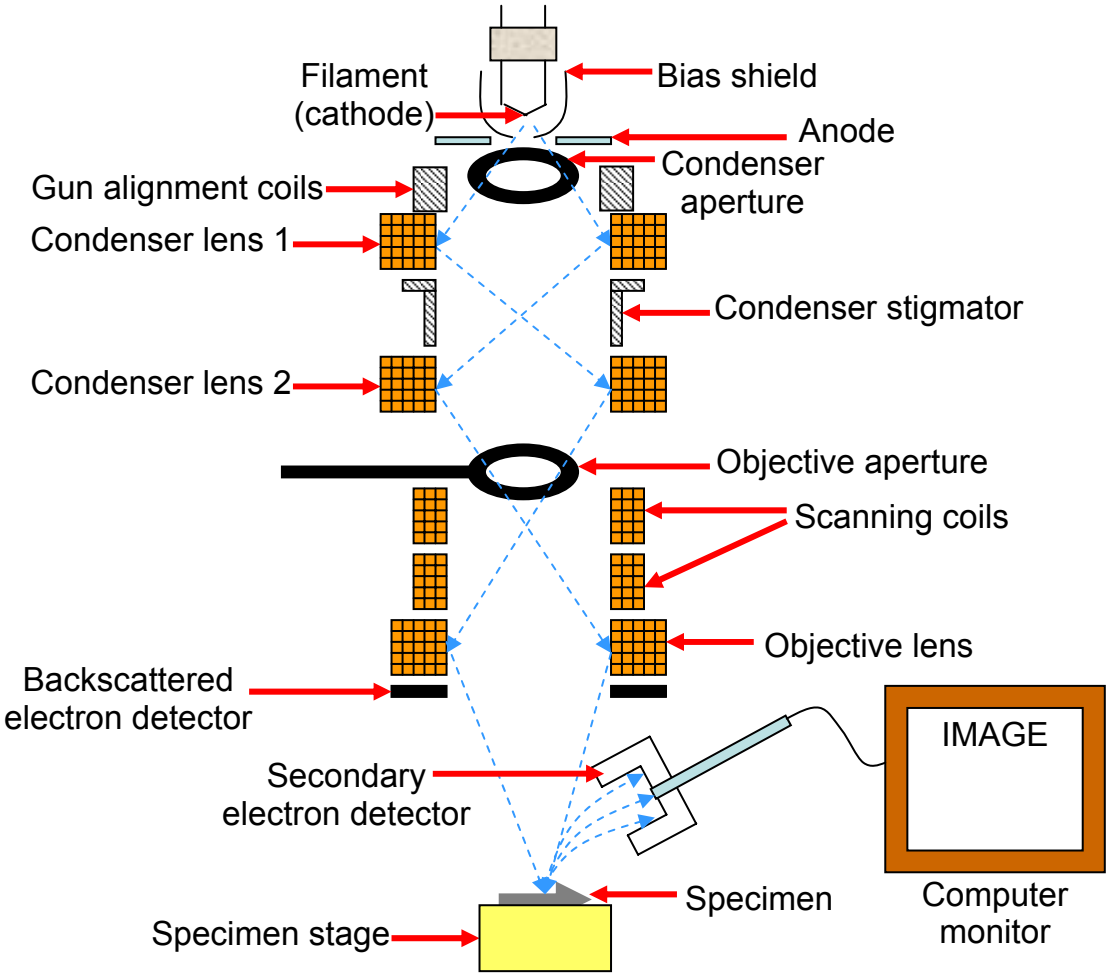

FIG.4.4. Schematic of a scanning electron microscope.

A JEOL 6400 scanning electron microscope was used to obtain images of the surfaces. Images were captured from secondary electrons. The working voltage was 15 kV and the working distance varied.

D. MATERIAL COMPOSITION

Diffraction is the process of bending, spreading and interference of waves due to deflection by an obstruction in their path. Such diffraction happens to X-rays when they are deflected by regularly spaced atoms in a crystal. The diffracted X-rays are also regularly spaced and hence form a pattern on a photographic plate consisting of regularly spaced spots. X-ray crystallography functions on the principle of Bragg's law. In 1913 Sir W.H. Bragg and his son Sir W.L. Bragg discovered that diffracting X-rays are constructive, off certain crystals, at certain angles of incidence. When X-rays strike an atom, they transfer some of their energy to electrons in the atom. The electrons are transferred to a higher energy level temporarily, and fall back to their stable state, emitting the energy in the form of X-rays. These re-emitted X-rays interfere, giving constructive or destructive interferences. According to Bragg's law, the interference is constructive when the phase difference between waves is proportional to 2π (see Fig. 4.5). The equation governing Bragg's law is

$$n\lambda = 2d\sin\theta, \tag{1}$$

where n is an integer

λ is the wavelength of X-rays

d is the spacing between planes in the atomic lattice

θ is the angle between the incident ray and the scattering planes

An X-ray diffractometer (Bruker AXS D8 Discover) with Cu Kα radiation was used to determine the crystalline composition of metals and their wear debris.

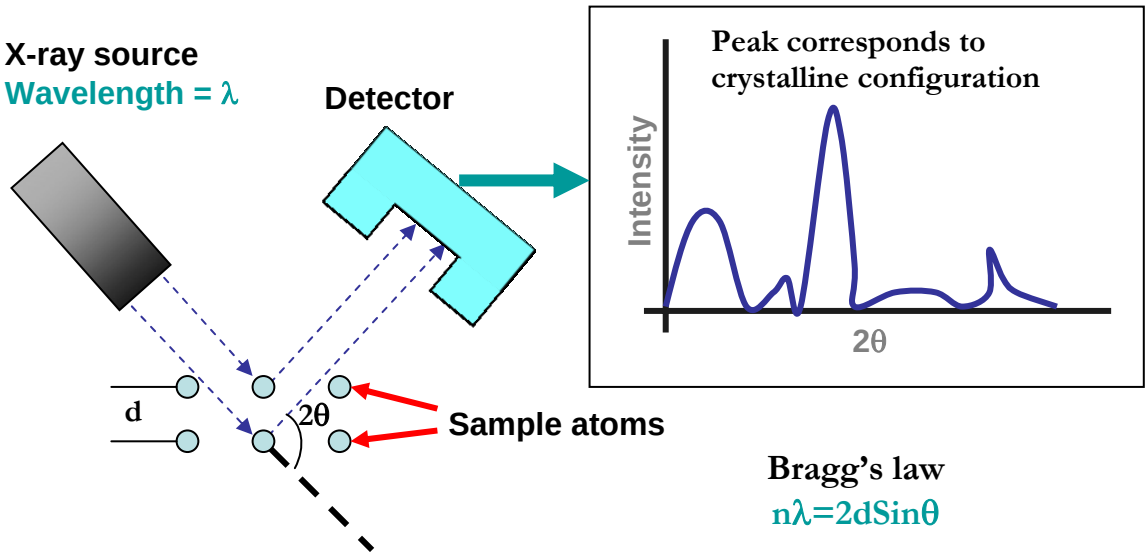

FIG. 4.5. Schematic of an X-ray diffractometer.

E. NANO MECHANICAL PROPERTIES

Nano-indentation tests were conducted using a Hysitron triboindenter. The triboindenter possesses a replaceable tip (diameter in the nm range) that can be moved with a precision of nanometers. Perpendicular penetration into a specimen or parallel scratch testing on the surface can be achieved. Different types of tips can be incorporated, depending on the nature of the sample to be tested. Motion control and load sensing is achieved with piezoelectric transducers. The data is processed by a computer. Load-depth curves and other mechanical property values can be obtained. The loading rate, peak load and duration of applied loads can be varied. Figure 4.6 is a schematic of the

triboindenter. The loading-unloading curve is shown in Fig. 4.7. From the results, information on hardness, modulus, elastic, plastic, and viscoelastic behavior can be obtained.

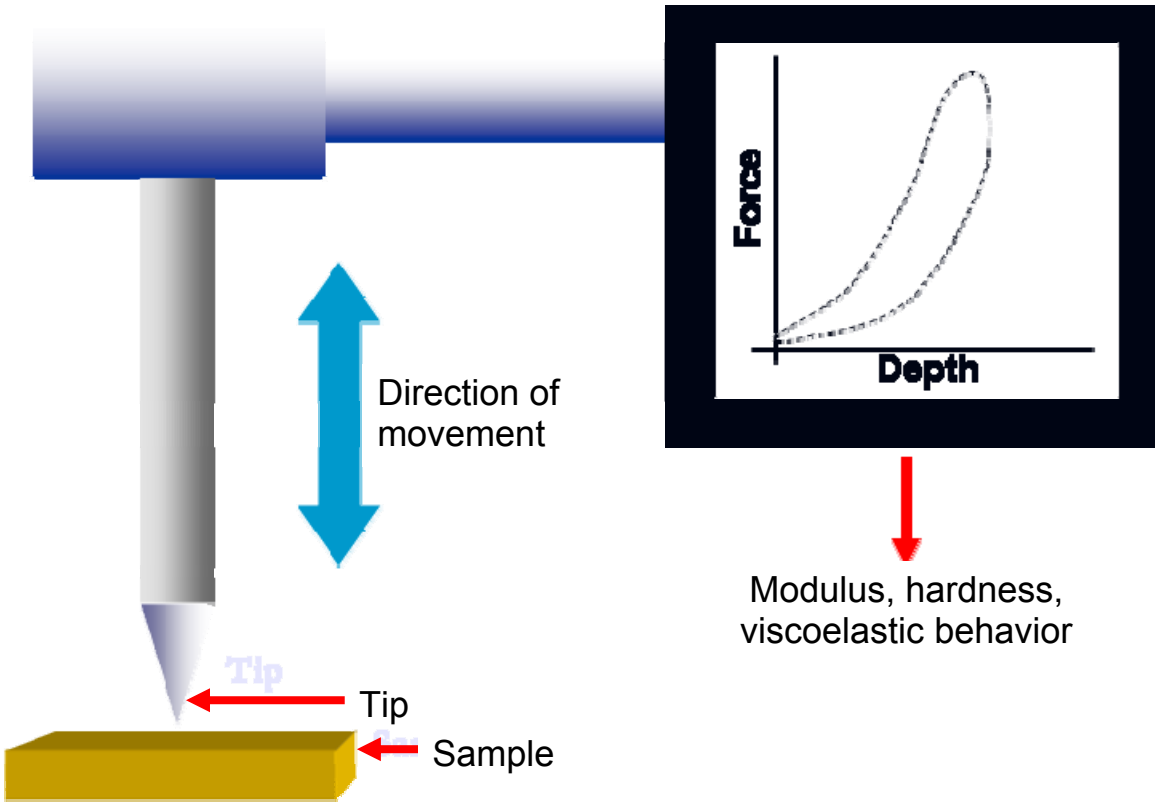

FIG.4.6. Schematic of nanoindenter.

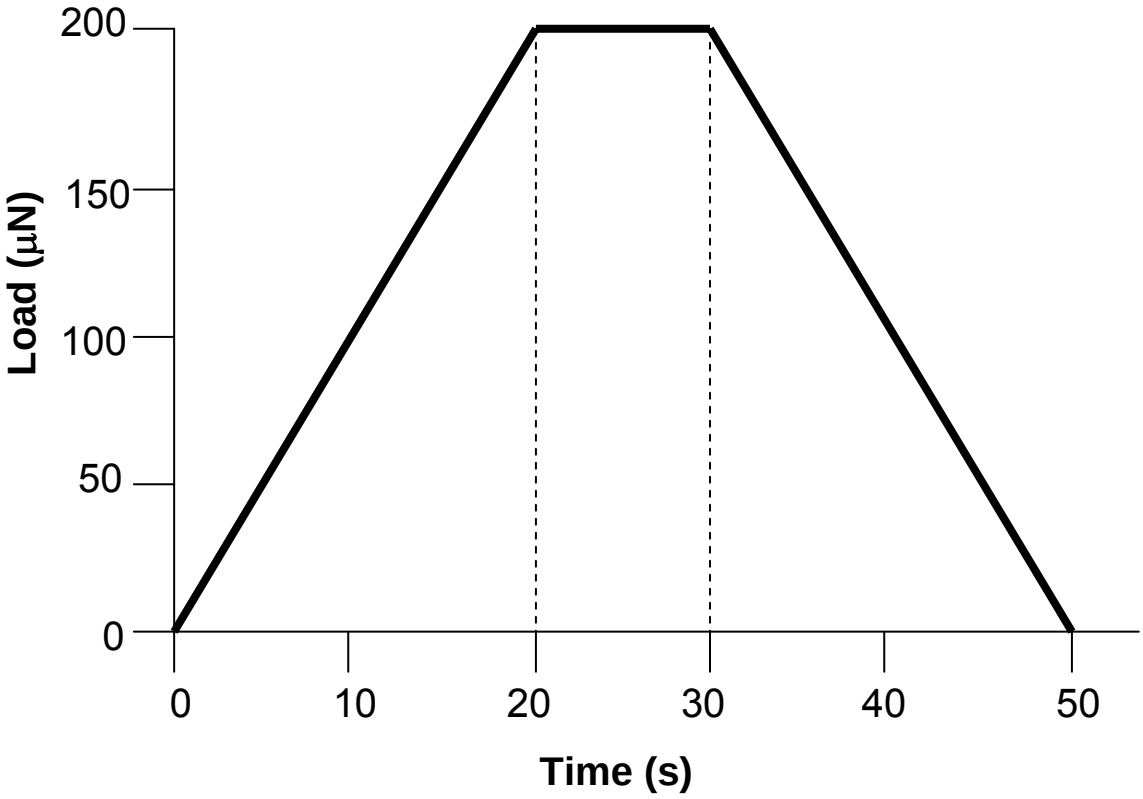

FIG. 4.7. Nano-indentation load-time curve.

CHAPTER V

RESULTS

As discussed in Chapter I, a wide variety of tribomaterials have been used for biological applications. The present research focuses on the artificial cartilage. Therefore, the surface, near-surface, and bulk properties are particularly interesting. This chapter presents the results of two groups of materials: polymeric composites and metals with coatings. The polymers are considered for frictional behavior mimicking cartilage while the coated metals are for load bearing and wear properties.

A. POLYMER BASED MATERIALS

1. Multiphase polymeric composite

The advantages of using multi-phased polymeric composites are several. The distinguished properties of each phase could contribute to the desired, hybrid property. This is considered important in the biological environment where chemical degradation resistance and mechanical durability are required.

Figure 5.1 shows nanoindentation load-depth curves for the composite PTMC+HAP+NT (PTMC + Hydroxyapatite + multi-walled carbon nanotubes), cartilage, subchondral bone and UHMWPE. As expected, bone showed the highest stiffness with the lowest penetration depth. The deformation during the dwell period for the bone was also lower. The UHMWPE surface exhibited the lowest stiffness. The UHMWPE also showed highest viscoelastic strain during the constant load dwell period. Cartilage and PTMC+HAP+NT exhibited very close load-depth values with cartilage being slightly

stiffer. The load-depth curves for both these materials were in between those of bone and UHMWPE. Details will be discussed in the next chapter.

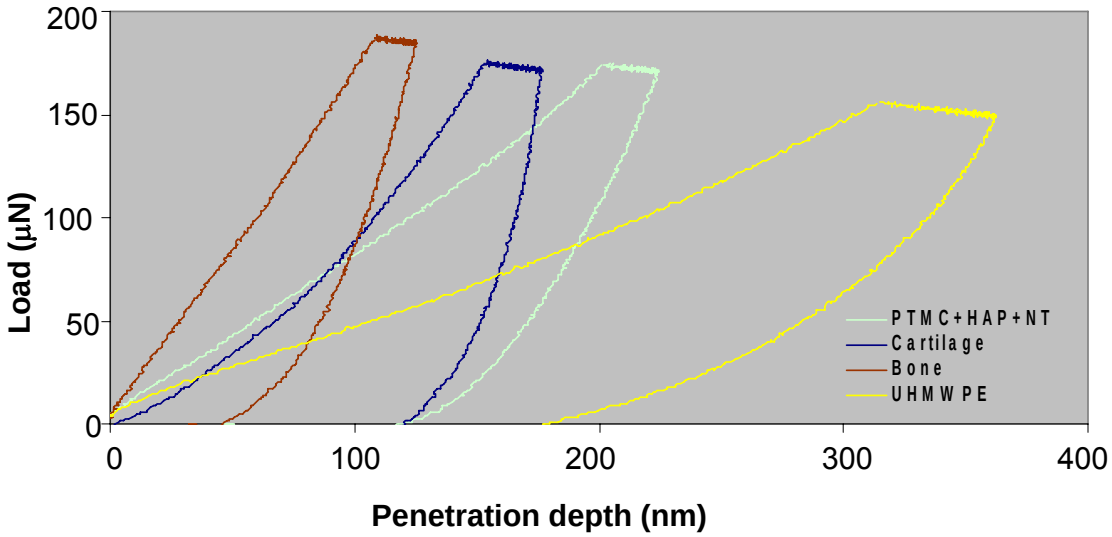

FIG. 5.1. Nanoindentation load-depth curves of PTMC+HAP+NT, cartilage, bone and UHMWPE.

Figure 5.2 shows the average friction coefficient values with standard deviation error bars for the UHMWPE, cartilage, and the PTMC+HAP+NT. Tests were conducted against cartilage with SSF between the surfaces. The coefficient of friction (COF) value for the UHMWPE against cartilage was the highest while that for cartilage against cartilage was the lowest. The value for PTMC+HAP+NT was in between those of UHMWPE and cartilage.

Figures 5.3 a, b and c are AFM topography and phase images of unworn cartilage, PTMC+HAP+NT, and UHMWPE respectively. Cartilage shows longitudinal fiber-like structures which may correspond to collagen fibers. The PTMC+HAP+NT image shows

patches (probably HAP) sticking out of the surface with a nanotube-like structure lying along the surface (Figure 5.3b). UHMWPE possessed a fairly uniformed phase on the surface with the lowest variation in height (~0.3 μm). The spots in the UHMWPE phase image were probably created due to the manufacturing process. Cartilage had the highest height variation of ~3μm. The cartilage topography image indicates the presence of a pore-like structure on the surface, through which substances can pass in and out of the cartilage.

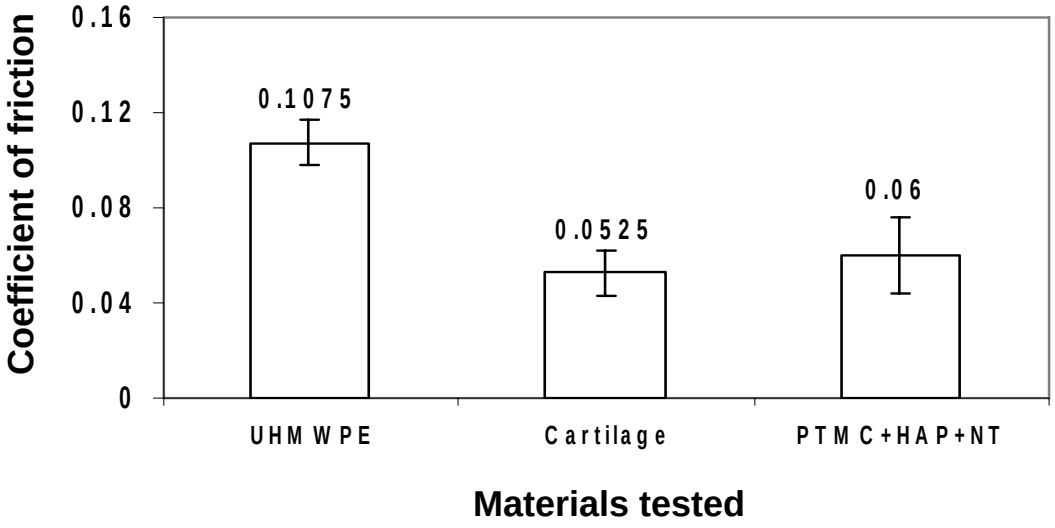

FIG. 5.2. Average coefficient of friction for tested materials.

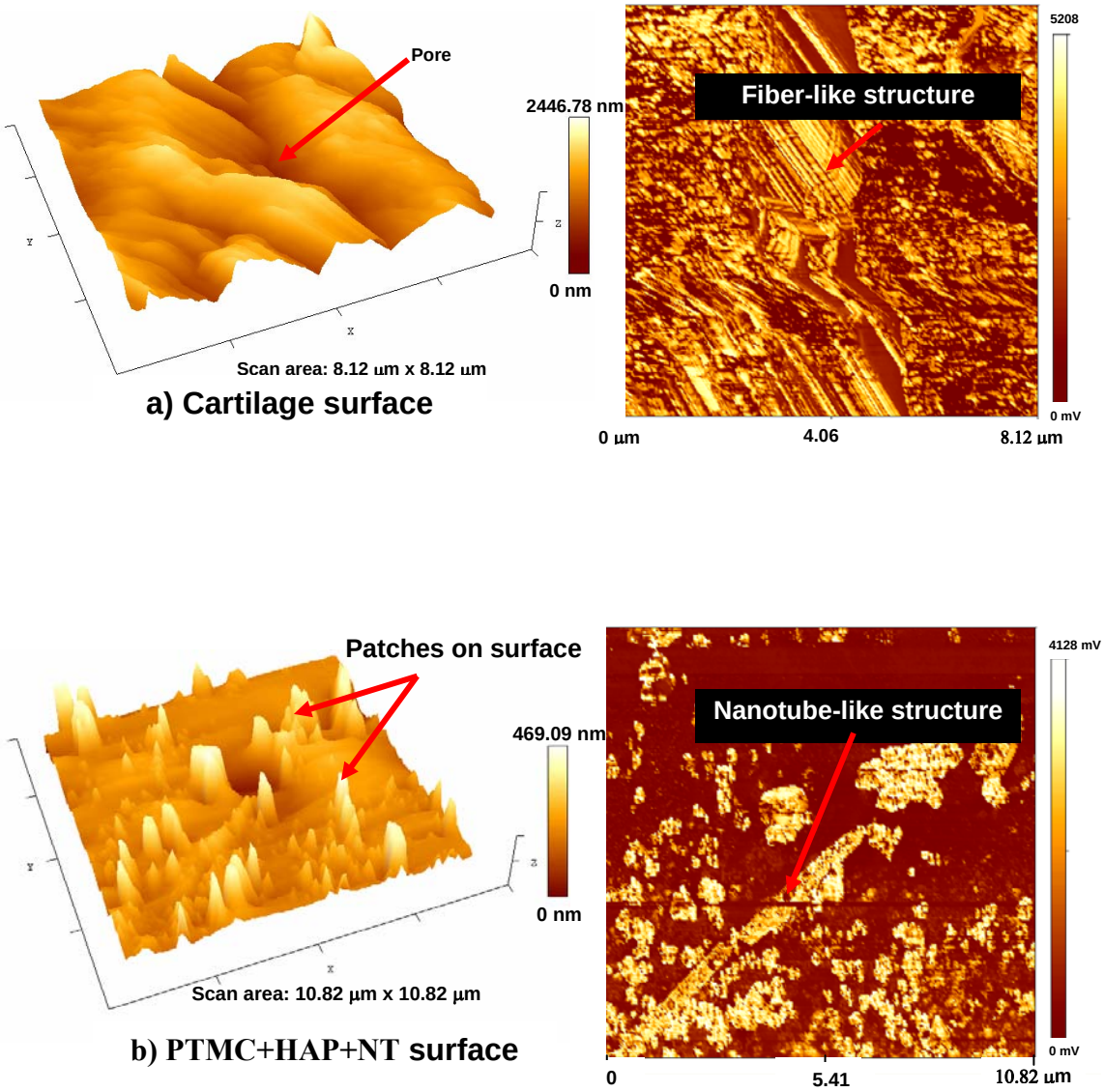

FIG. 5.3. AFM topography (L) and phase (R) images.

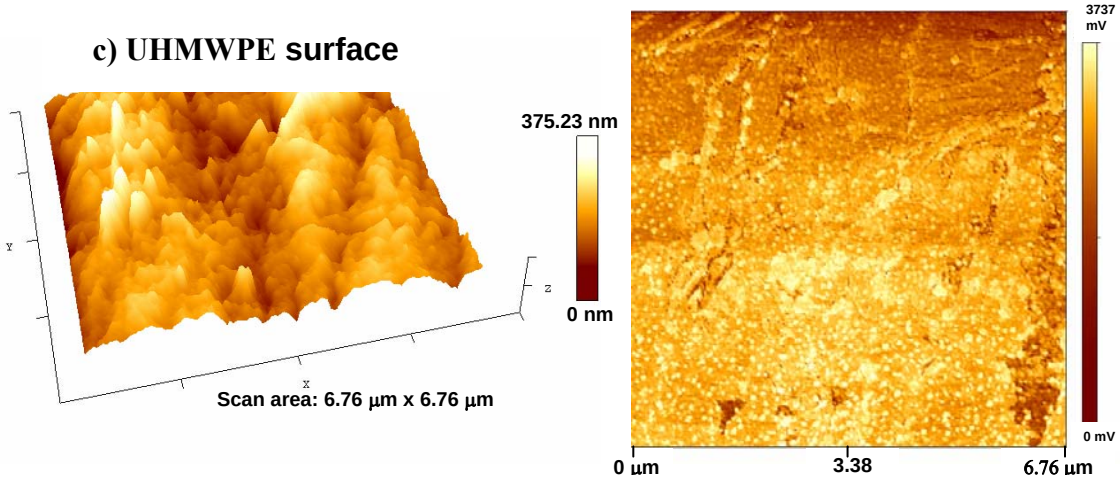

FIG. 5.3. (continued)

2. Polyimide-SWNT composite

Figure 5.4 shows the profile of the nano-triboindenter tip. Figure 5.5 shows the stress-strain profiles of nanoindentation tests conducted on polyimide-SWNT composite specimens with varying weight percent concentrations of SWNT. The radius of the nanoindenter tip was 150 nm. This value was used to calculate the effective area of contact *a*. If the penetration depth is *d*, the effective area of contact is given as:

$$a = \pi d \times (2 \times 150 - d), \qquad (2)$$

The linear stress was calculated as load/*a*. Fig. 5.5 shows plots of the stress versus the indentation depth for PI + NT, cartilage and UHMWPE samples. Pristine PI (0% NT) shows the stiffest response to nanoindentation. As the percentage of nanotubes is increased, the stiffness decreases, goes through a minimum, and then increases. Cartilage has a much lower stress increase per nm indentation, but has greater hysteresis than the pure PI and PI + NT samples (indicating greater energy absorption and

viscoelastic behavior). At the same loading rate, the stress on UHMWPE are much lower at the initial stages of indentation, but increases rapidly at approximately 300 nm depth (Fig. 5.6). There is not much hysteresis shown by UHMWPE and the unloading curve follows the loading curve very closely.

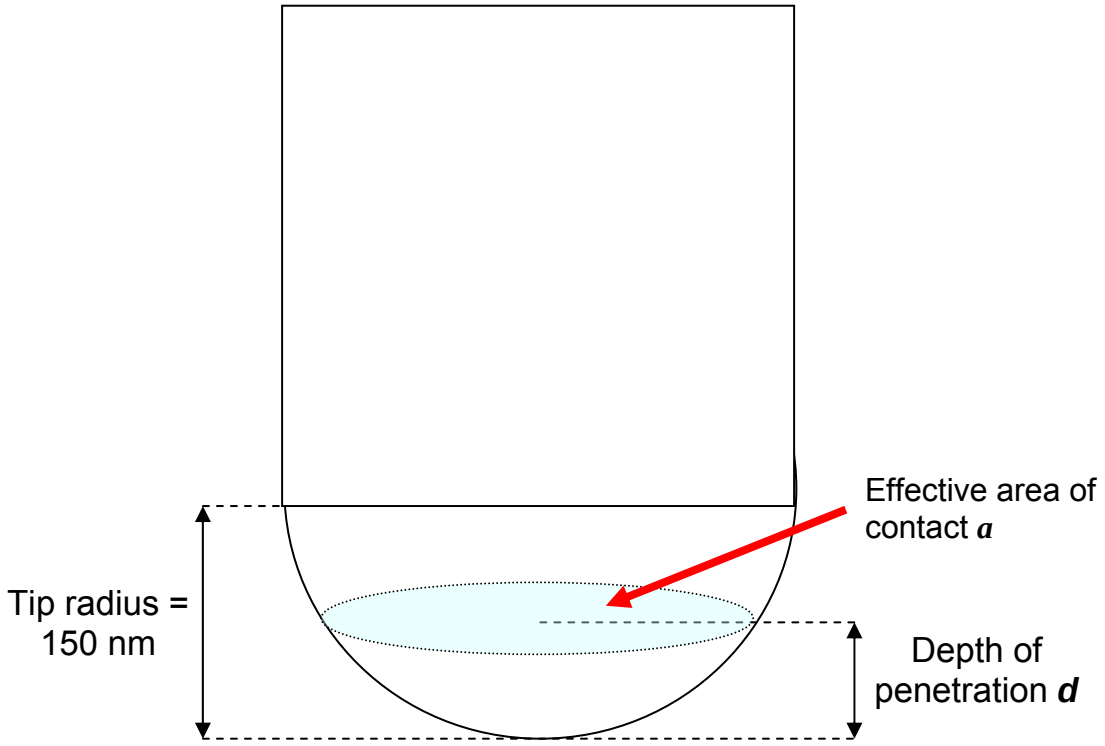

FIG. 5.4 Nano-triboindenter tip.

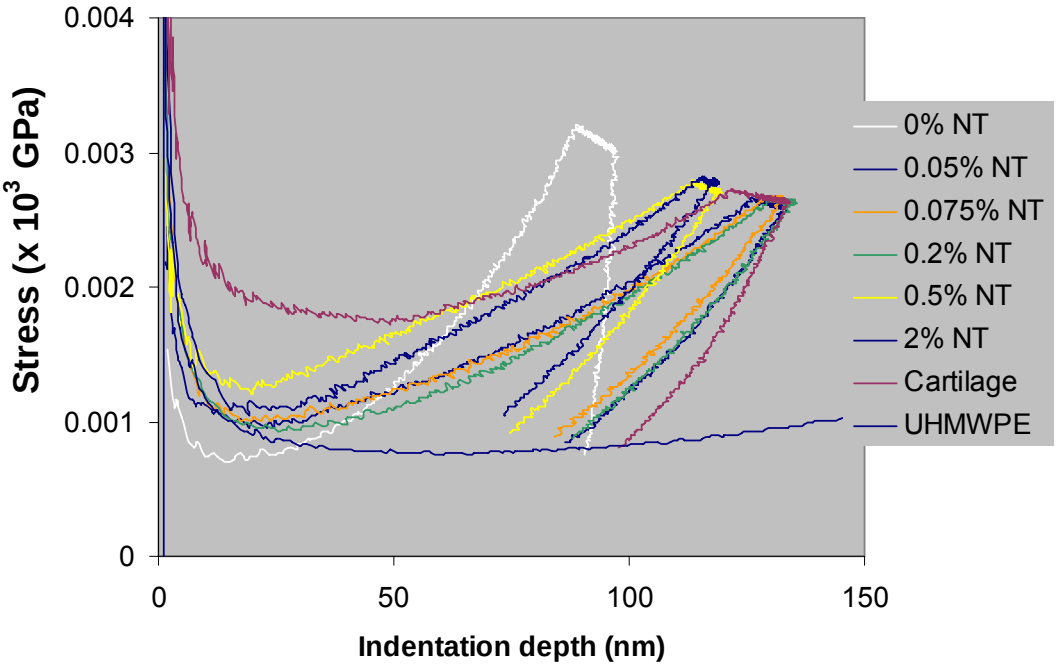

FIG. 5.5. Stress-indentation depth plots for PI + NT, cartilage and UHMWPE.

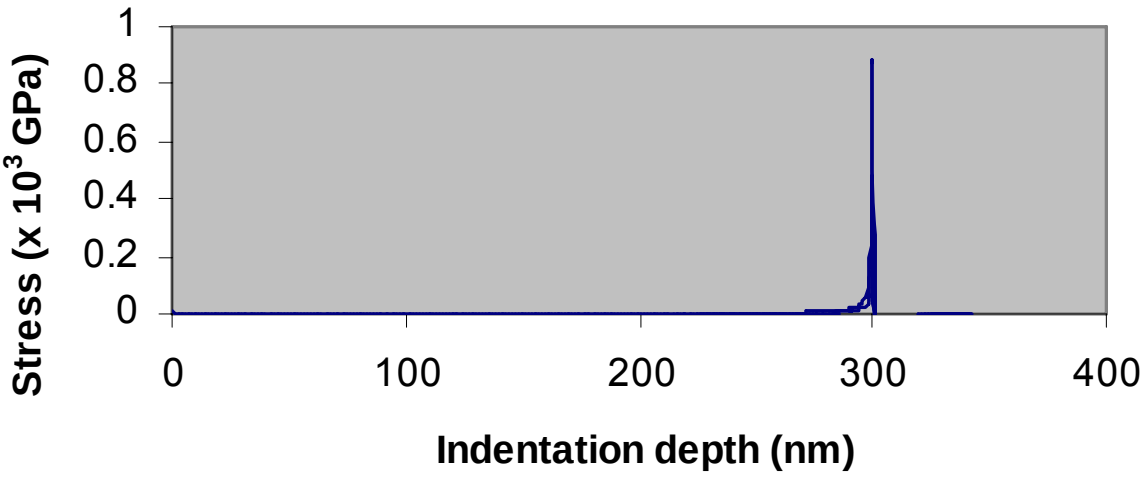

FIG. 5.6. Stress-indentation depth plot for UHMWPE

Figure 5.7 illustrates plots of the coefficient of friction against %SWNT for the PI-SWNT composites under 3 different regimes-when articulated against cartilage with SSF between the surfaces, when articulated against Ti6Al4V under dry conditions and when articulated against Ti6Al4V with SSF between the surfaces. For the dry condition, at a %SWNT concentration of approximately 0.5, there is a minimum in the coefficient of friction. The coefficient of friction ranges approximately between 0.24 (0.5%SWNT) and 0.44 (0.075%SWNT). These values of coefficient of friction are much higher than the values found in natural joints (~0.01). However, there is definite evidence that at an optimum concentration of SWNT's, the coefficient of friction can be minimized. We can see that the COF of the PI composite against Ti6Al4V under dry conditions is the highest. The presence of SSF between the surfaces caused a lowering in the COF. The

lowest COF values are however noticed for the PI composite when tested against cartilage.

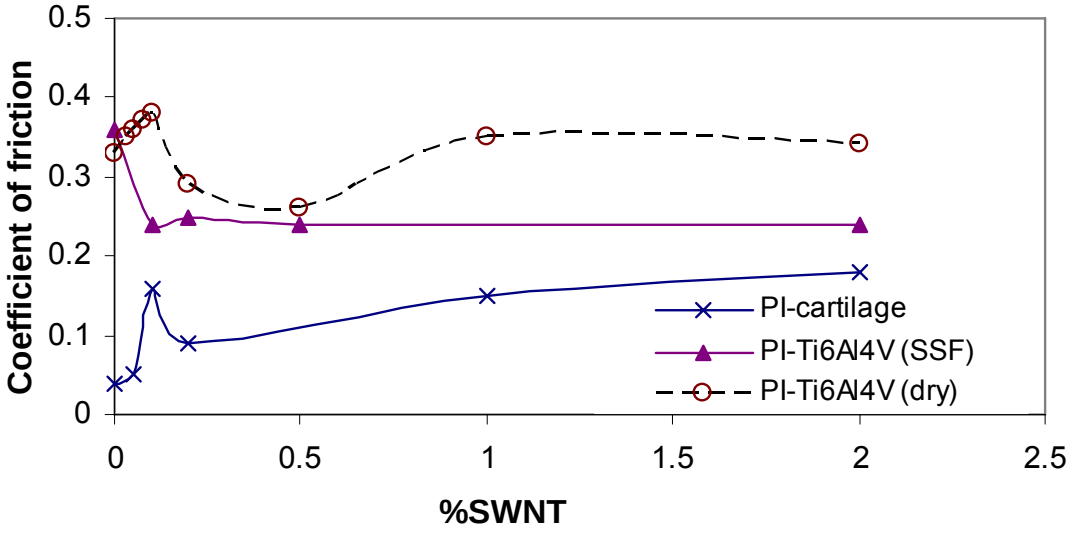

FIG. 5.7. COF versus %SWNT for PI+NT against cartilage and Ti6Al4V.

Figure 5.8 is a TEM image of SWNT's that were added to the PI. It can be seen that the nanotubes (NTs) are present in bundles with a number of them being in contact with each other. This NT-NT contact could have influenced the friction and indentation behavior described earlier. Fig. 5.8b is a TEM image of NTs embedded within the PI matrix. This is an image of a wear particle that came off the composite with 2% NT during the friction tests. There is an indication that the particle tore off around the NT indicating that the NT adheres well to the PI matrix. Figure 5.8c is another image of a

wear particle showing bundles of NTs with the tear taking place around the edge of the NTs. This is also an indication of the strong bonding between the NTs and PI.

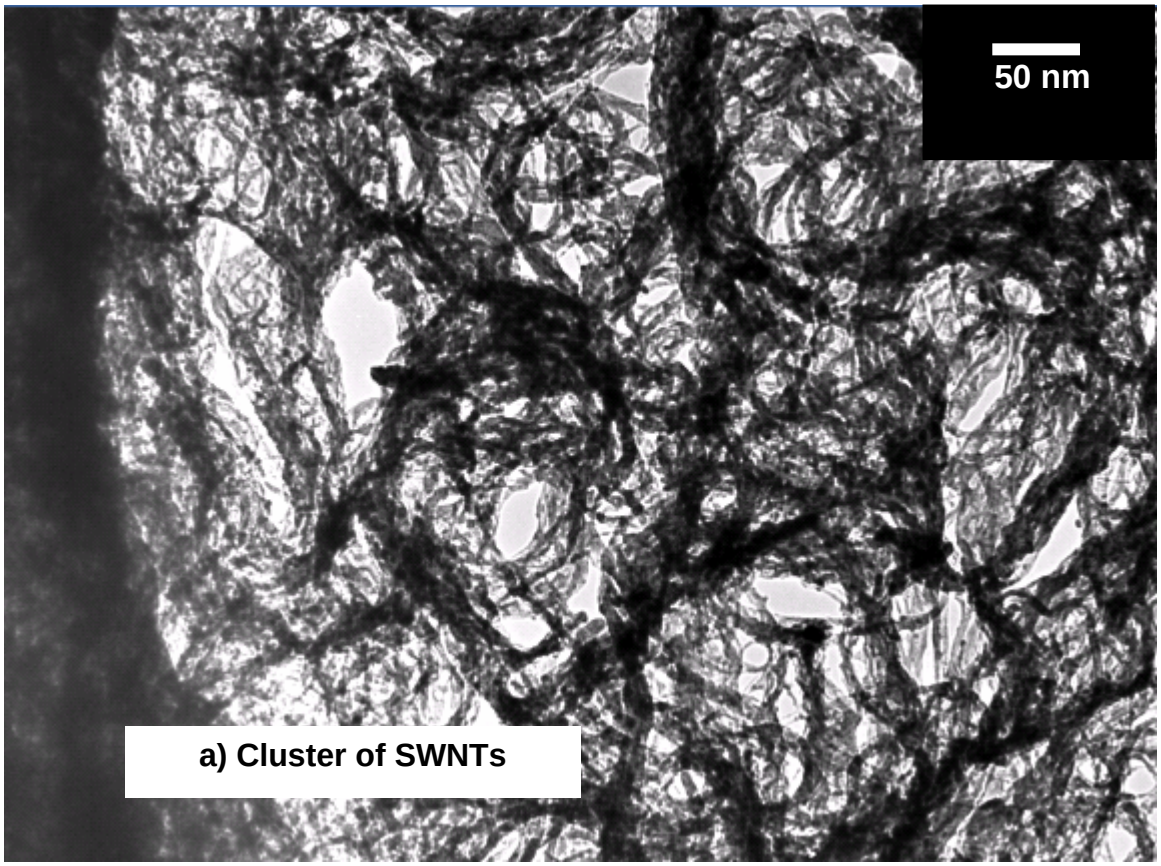

FIG. 5.8. TEM images of SWNT+PI composite (200 kV working voltage).

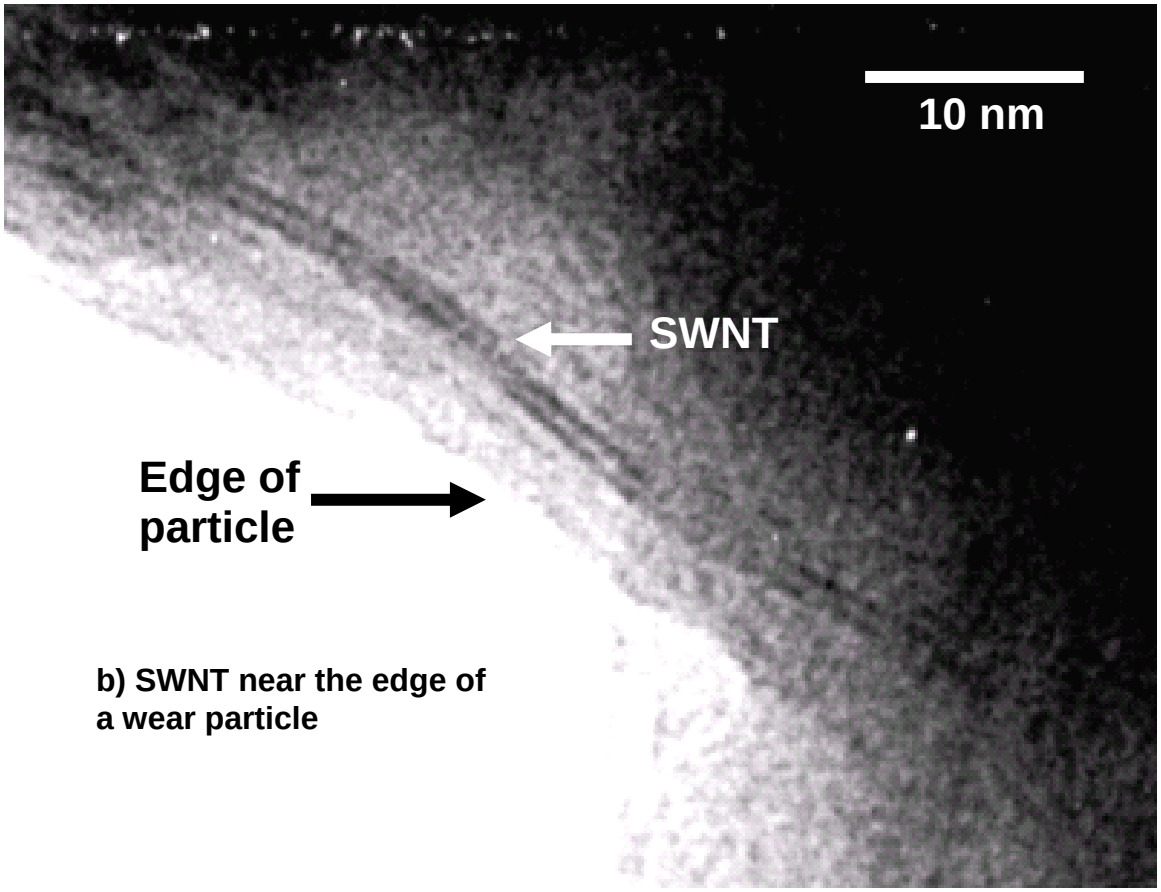

FIG. 5.8. (continued).

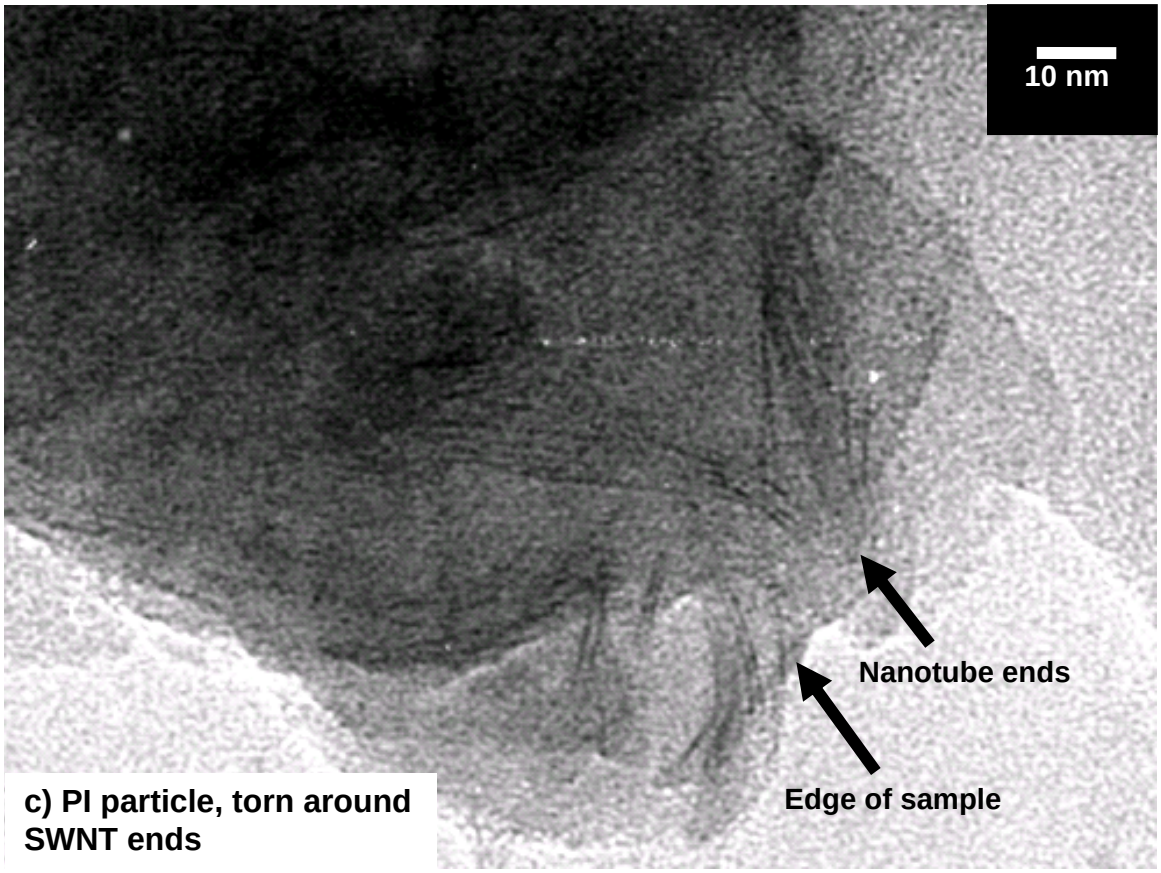

FIG. 5.8. (continued)

Figures 5.9a to g show the AFM topography (on the left) and phase (on the right) images of the wear tracks of pure PI, PI+0.05%NT, PI+0.1%NT, PI+0.2%NT, PI+0.5%NT, PI+1%NT and PI+2%NT when worn against Ti6Al4V alloy under dry conditions. This information was necessary in order to determine the internal and surface structure of the composite with change in nanotube concentration. Figs. 5.9a to g indicate that the nature of wear changes as the concentration of nanotubes increases. The wear track of pristine polyimide has regular abrasive wear grooves (Fig. 5.9a). The phase image indicates a fairly uniform phase throughout. Fig. 5.9b shows corrugations

within corrugations for PI+0.05%NT, the phase image being uniform. Fig. 5.9c shows abrasive wear grooves in the direction of sliding, as well as striations perpendicular to the sliding direction for the case of PI+0.1%NT. The wear track for 0.2%NT concentration has long pits created due to nanotube bundles being pulled out of the surface (Fig. 5.9d). The surface also seems to be somewhat porous. The surface of the wear track for 0.5%NT indicates larger pores with greater distance between pores than the sample with 0.2%NT (Fig. 5.9e). The wear track for the sample with 1%NT shows large abrasive wear grooves with signs of cracking (Fig. 5.9f). Finally, the wear track of the sample with 2%NT shows crystalline grains with inter-granular like cracks (Fig. 5.9g). These images present interesting behavior that will be discussed in Chapter VI.

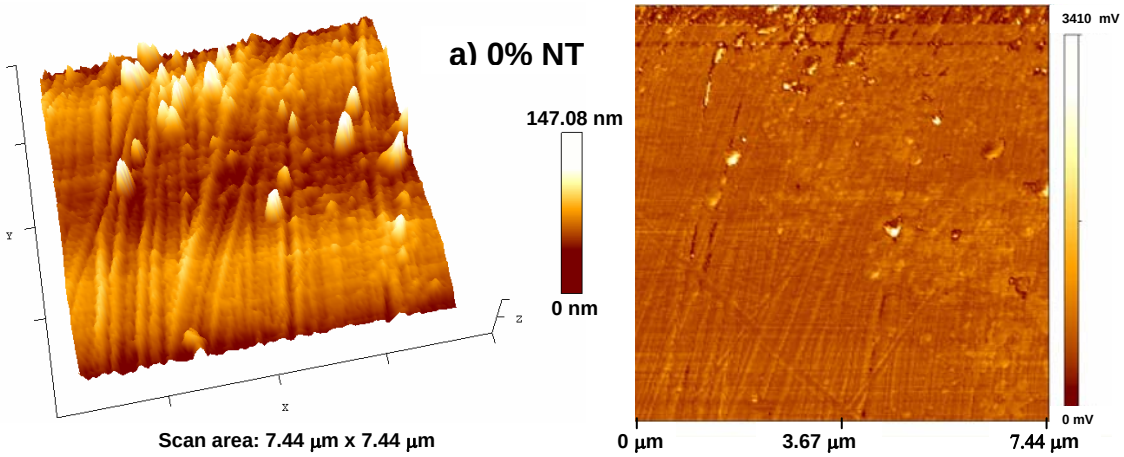

FIG. 5.9. Wear track of PI+NT against Ti6Al4V under dry conditions (AFM).

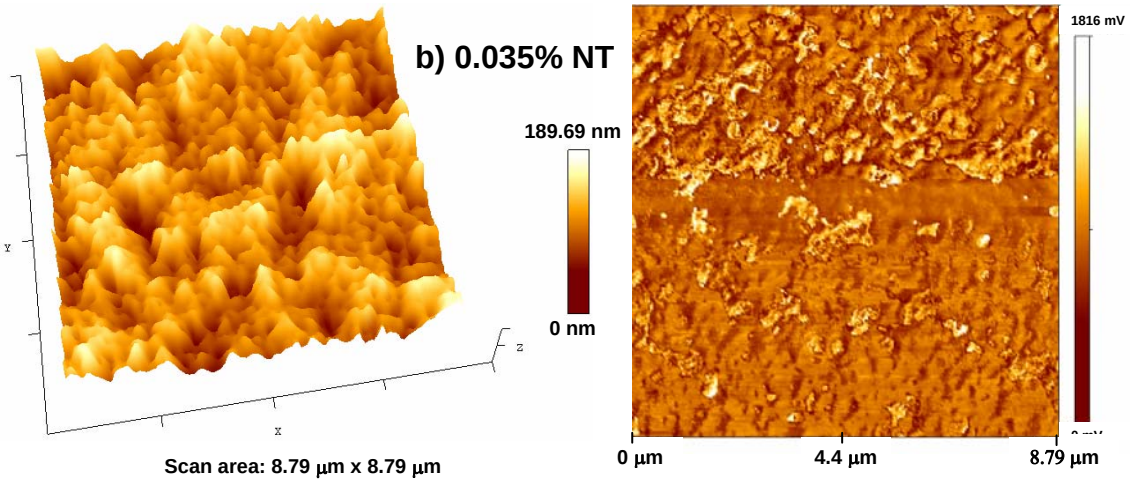

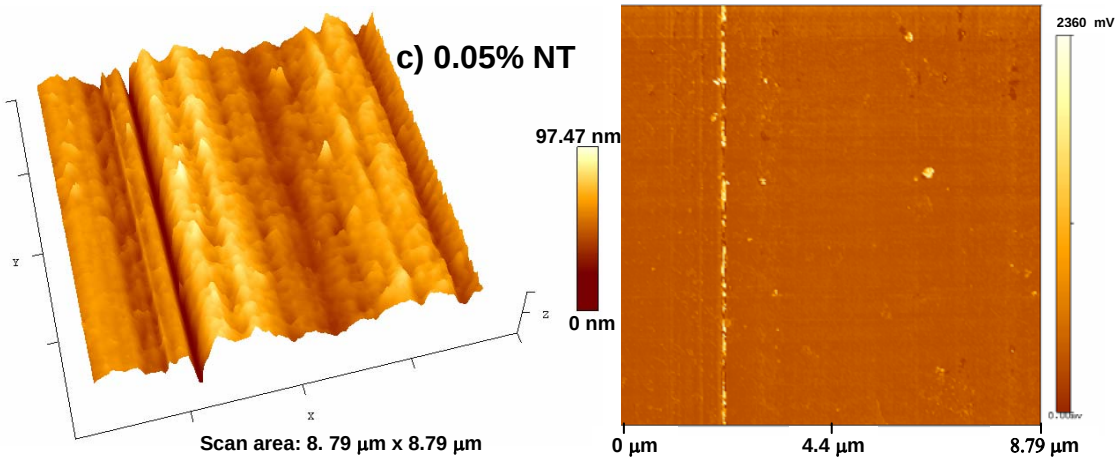

FIG. 5.9. (continued)

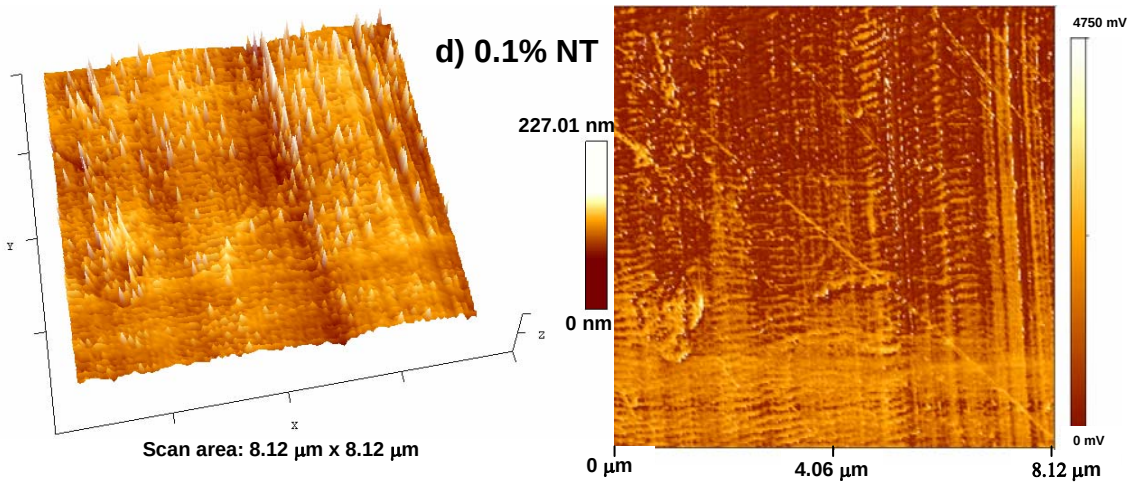

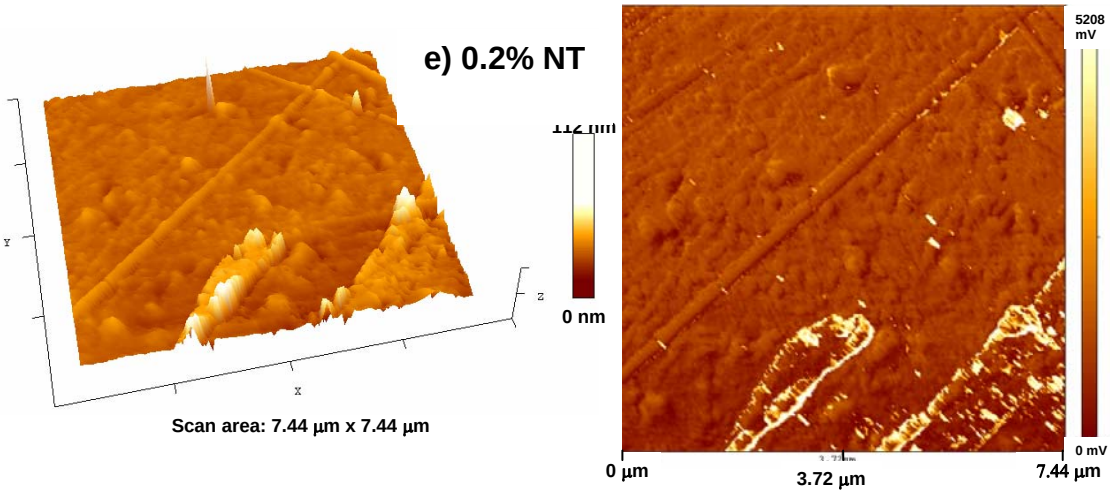

FIG. 5.9. (continued)

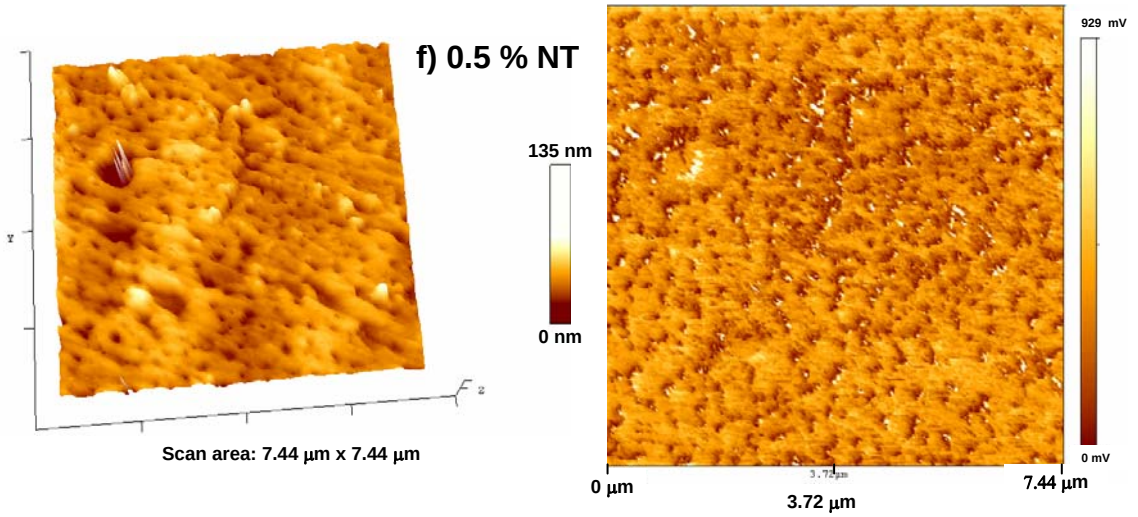

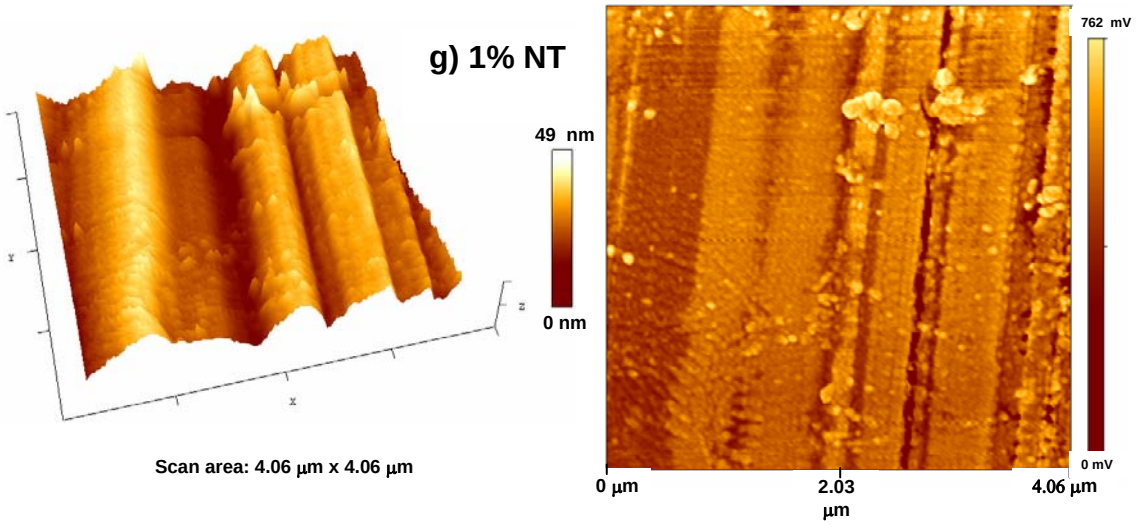

FIG. 5.9. (continued)

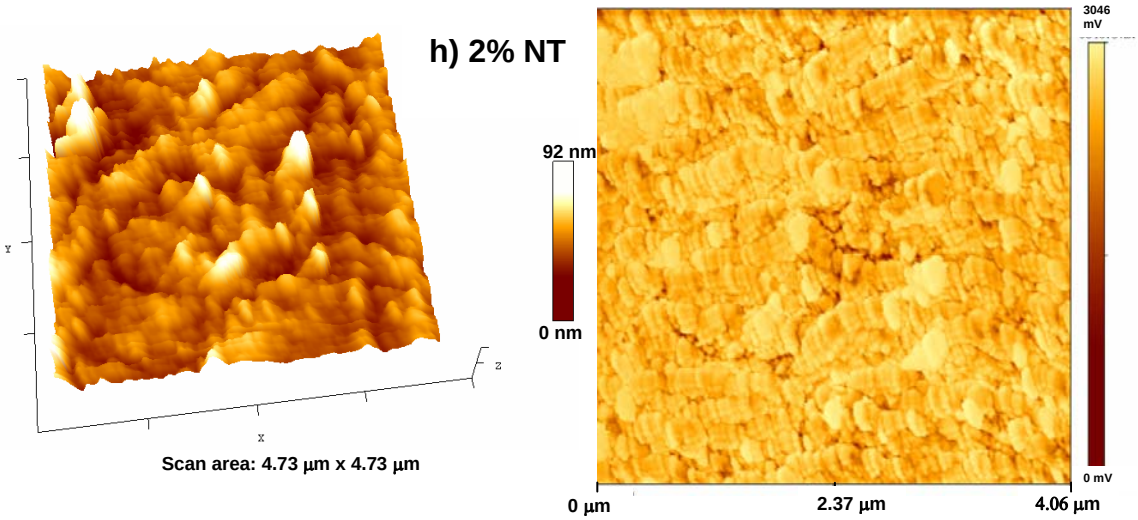

FIG. 5.9. (continued)

B. METALS FOR TOTAL JOINT REPLACEMENT

Initial tests were conducted at high speed (2.5 cm/s) at a short linear reciprocating amplitude of 1mm in order to compare wear characteristics. The materials tested were chromium, tantalum, and niobium, all boronized for 4h. Tests were conducted under dry conditions using SBF as a lubricant. Tests on chromium boride were also conducted using water as a lubricant.

The following information on boronized and pristine Cr has been published in a reference [152]. The information has been included here in order to compare the tribological characteristics with similar metals.

1. Pure and boronized chromium

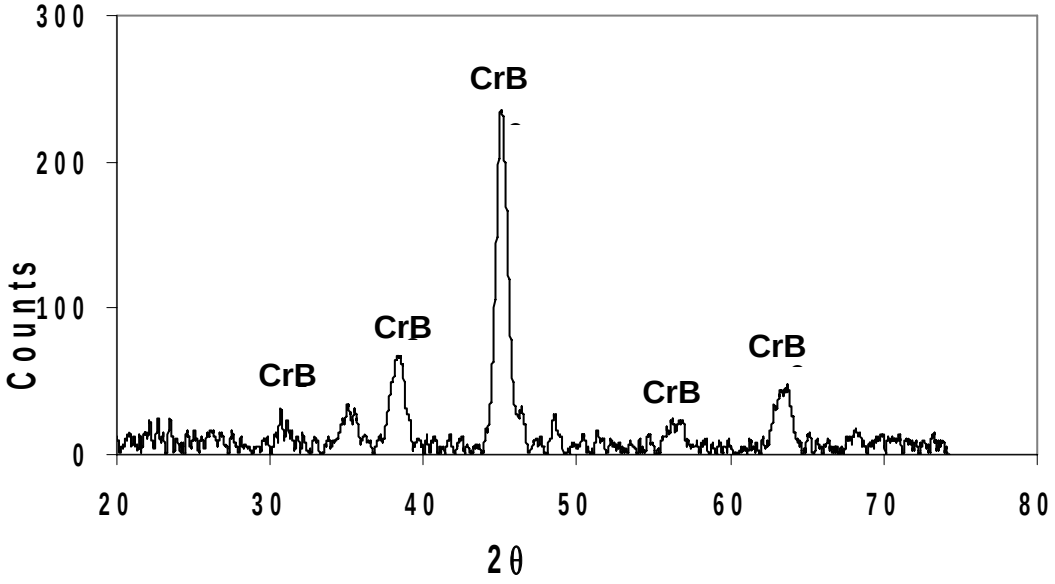

FIG. 5.10. X-ray diffraction pattern of the unworn boronized Cr surface.

Figure 5.10 shows the diffraction pattern of the as received boronized Cr surface. There is a single phase of CrB present. Figures 5.11a and b are plots of the coefficient of friction (COF) against the number of cycles for pure and boronized chromium respectively, under three test conditions. The figures show values for one particular test. In the dry test (Fig. 5.11a), in the case of pure chromium, there is a well defined running-in period with a maximum COF of 0.19. It then decreased and fluctuated around a value of approximately 0.1. In the case of dry chromium boride (Fig. 5.11b), the initial COF was approximately 0.15. It increased thereafter and reached a peak value of approximately 0.26 before decreasing to 0.21 at 25,000 cycles. It remained approximately at this value for the rest of the test. Boronized Cr therefore, had a higher average COF under dry sliding conditions than pure Cr. For tests with water, for pure Cr, the COF increased steadily from an initial value of 0.02 and stabilized after 23,000 cycles at a value of approximately 0.12. In the case of chromium boride, the COF fluctuated between 0.06 and 0.09. For tests under SBF conditions, pure Cr had an initial break-in period after which the COF decreased and stabilized around 0.02, whereas for chromium boride the initial COF was 0.06 after which it decreased and stabilized at approximately 0.035. The COF under SBF conditions, therefore, was found to be the lowest for both material combinations.

The SEM micrograph (Fig. 5.12a) for pure Cr under dry conditions shows that there is intergranular fracture on the surface. There is not much evidence of cracks, but there is evidence of flakes of delaminated material. For the SBF condition, both Cr and chromium boride (Fig. 5.12b) undergo abrasive wear as seen by the presence of grooves.

In the lower left part in Fig. 5.12b, there are some larger cracks found to form squares on the surface. This could be due to the SBF drying during SEM analysis resulting in material contraction (similar to mud cracking in dry weather).

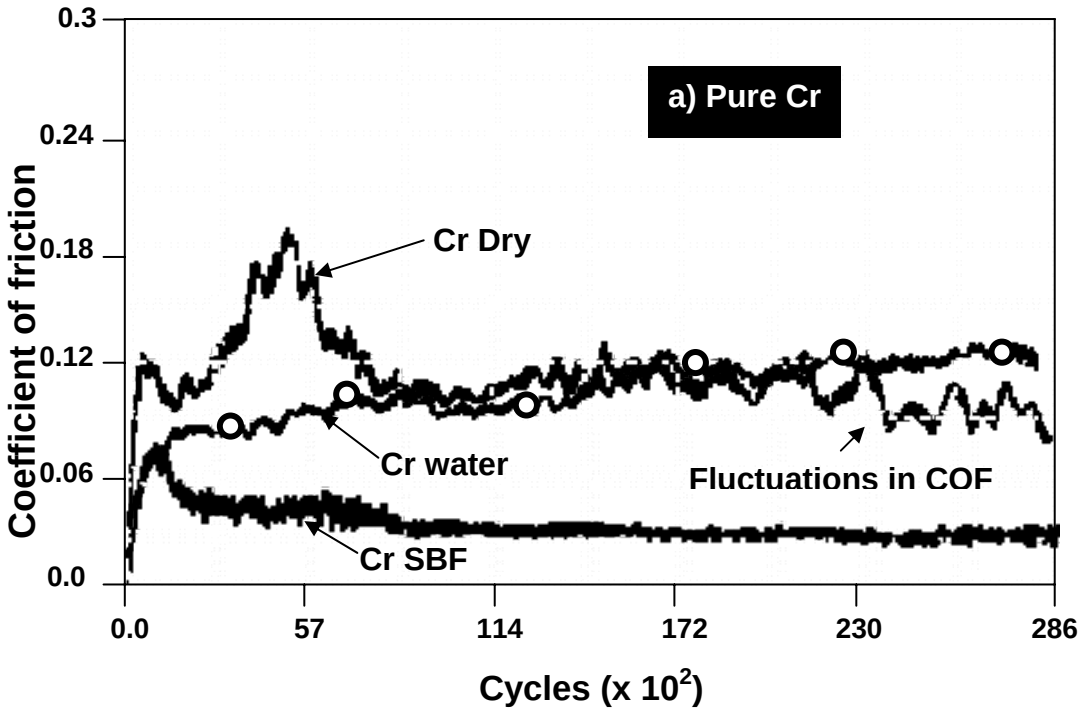

FIG. 5.11. Coefficient of friction against number of cycles.

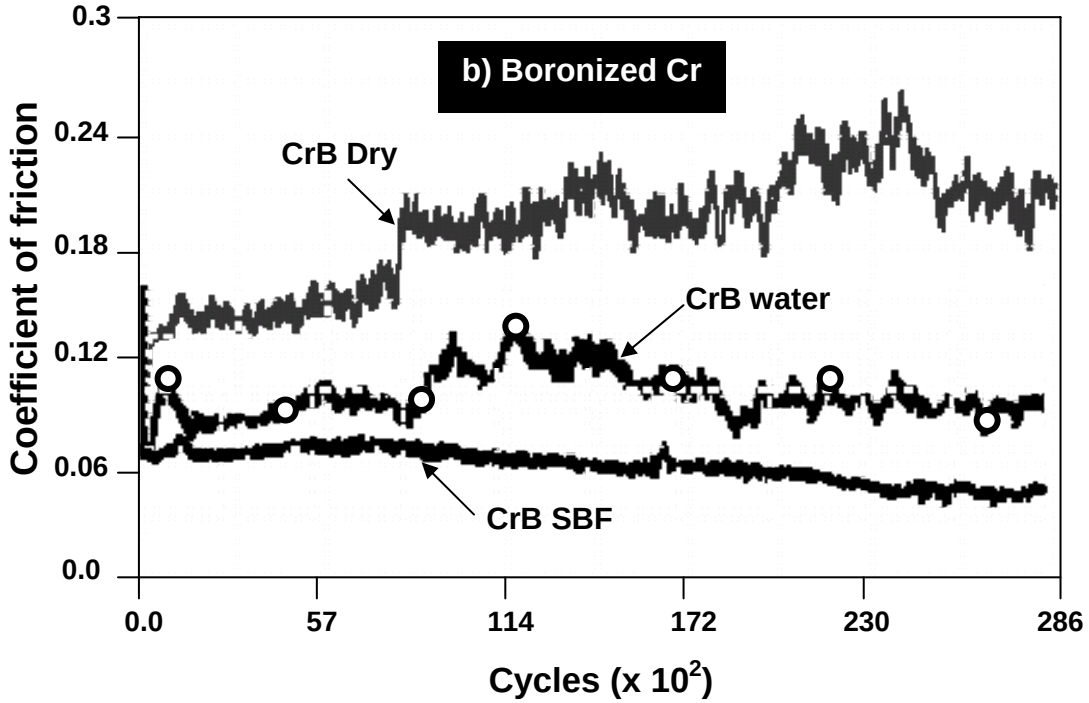

FIG. 5.11. (continued).

Further investigation was carried out using a TEM. Figure 5.13 shows images of debris for Cr and chromium boride tested under SBF conditions, with the diffraction pattern inserted. Under SBF conditions, there is a complex diffraction pattern (Figure 5.13). The debris collected from SBF tests showed an interesting layer-like structure. If this layer-like structure existed during the friction experiments, it could have induced the low friction coefficient observed.

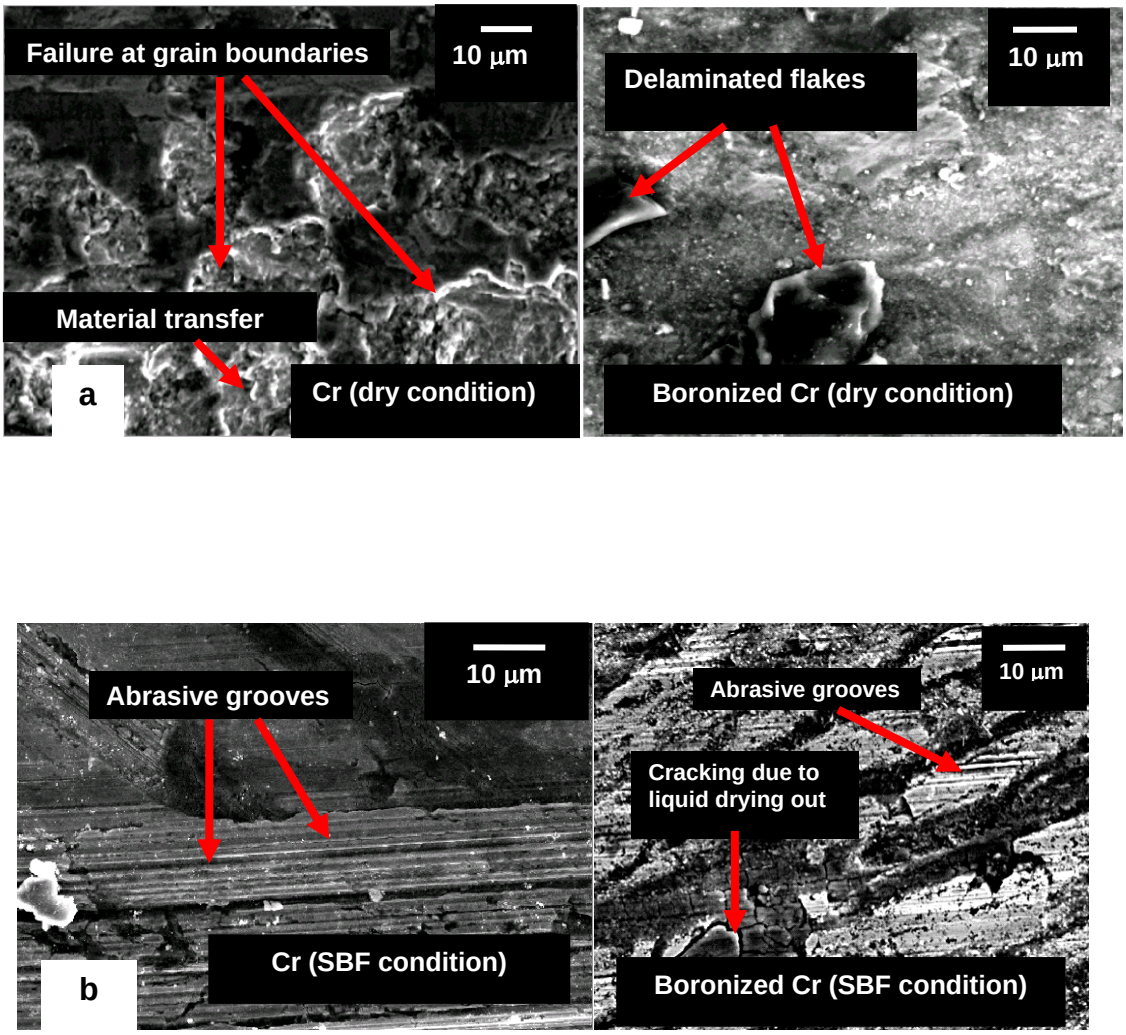

FIG. 5.12. SEM images of wear tracks (secondary electron, 15 kV, 39 mm WD).

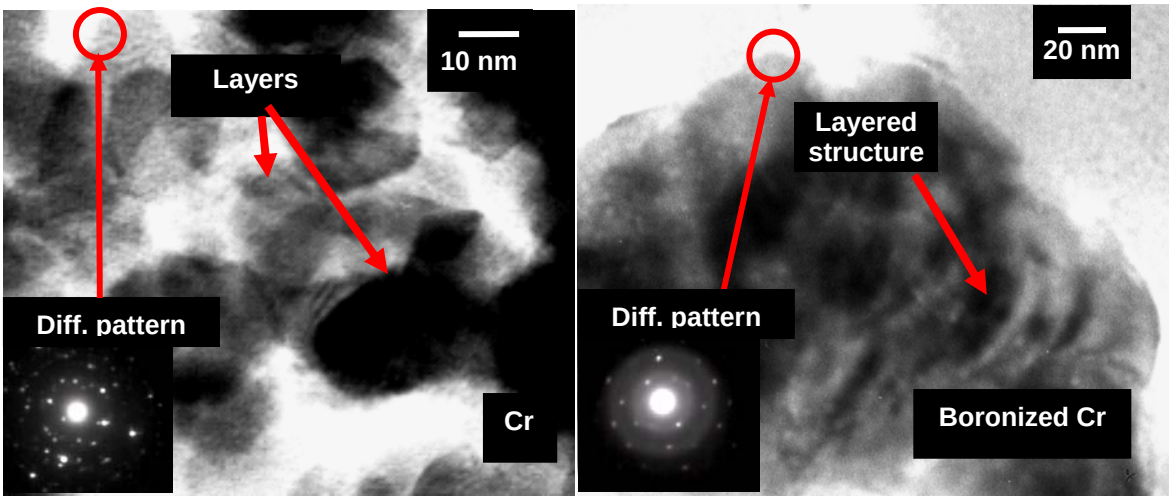

FIG. 5.13. TEM image debris obtained from SBF condition tests.

2. Boronized Niobium

Frictional Behavior

Figure 5.14 is a plot of the coefficient of friction versus time for the dry and SBF condition tests. The dry test condition indicates a definite run-in period after which the COF decreases and fluctuates between 0.24 and 0.36. There are spikes in the curve towards the latter part of the test. The COF curve for the SBF condition test has no running-in period. The initial COF is approximately 0.14, rises steadily and stabilizes around 0.2. There is a constant fluctuation in the COF throughout the test.

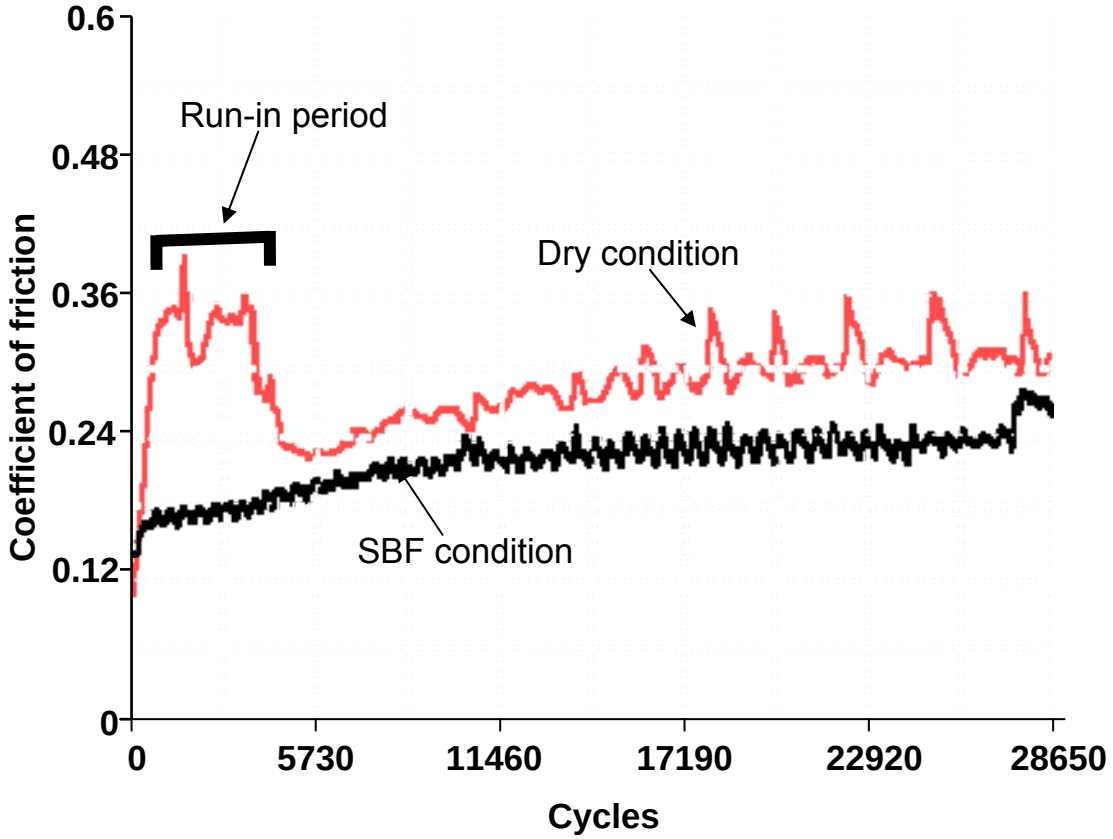

FIG. 5.14. Coefficient of friction vs. cycles for boronized niobium against E52100 steel.

Surface Characteristics

Figure 5.15 is an AFM image with the roughness values of the unworn boronized niobium surface. The average roughness was found to be greater than 200 nm. Fig. 5.16a is the wear track obtained in dry test conditions while Fig. 5.16b shows the wear track for the wet (SBF) condition. In Fig. 5.16a, it is seen that there are abrasive grooves that were introduced during the sliding tests. There is also indication of adhesive wear. In Fig. 5.16b, there is indication of a ductile-like layer (with grooves), that are continuous. It is an indication of accumulated, compressed debris. The rest of the area has cracks.

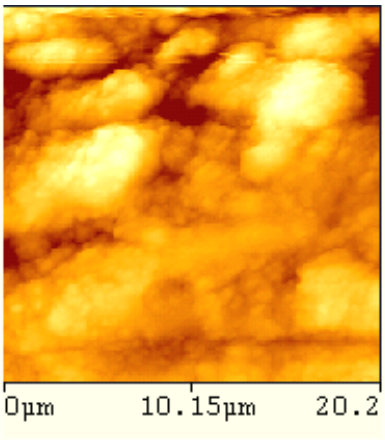

	Whole Area
Total Area St.	411.79 µm²
Roughness Avg. Sa:	217.72 nm
Root mean square sq:	279.22 nm
Mean Sm:	991.05 nm
Range Sr:	1804.56 nm

FIG. 5.15. AFM image and roughness values of unworn boronized niobium surface.

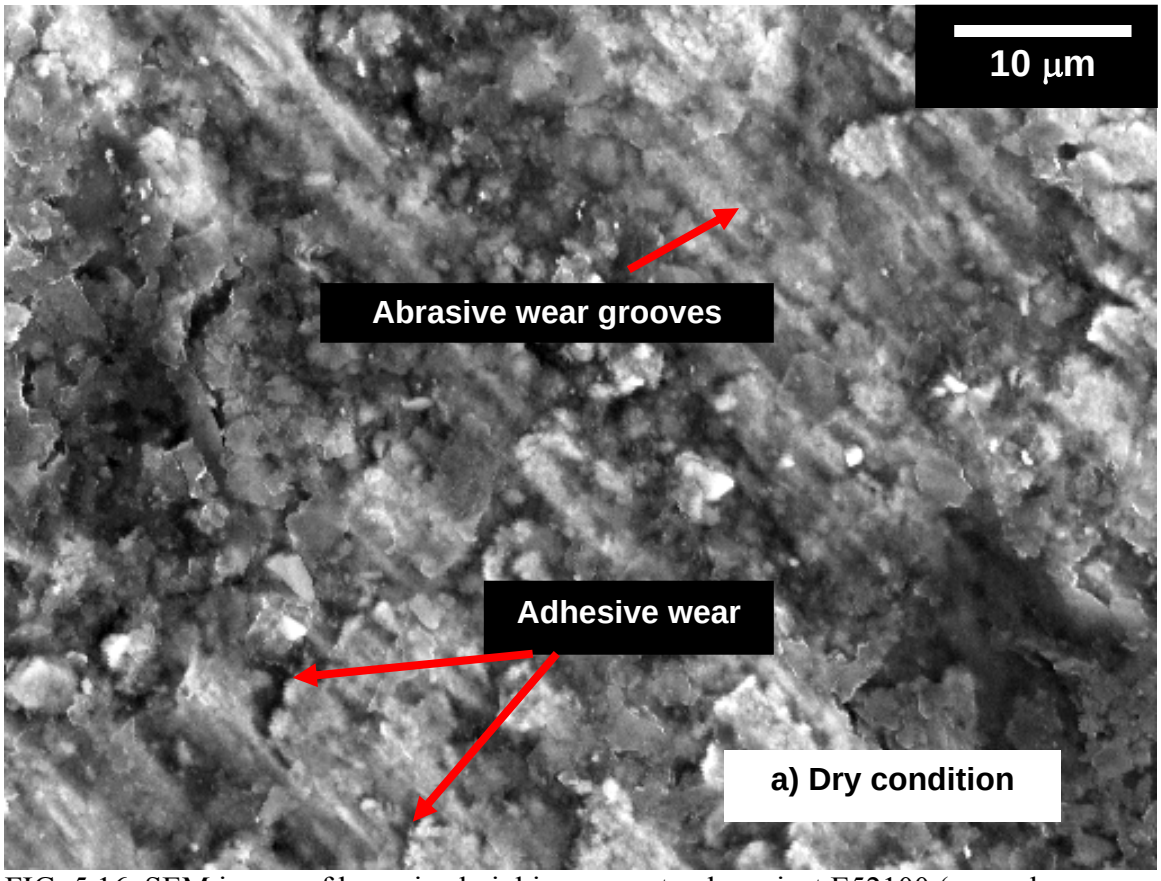

FIG. 5.16. SEM image of boronized niobium wear track against E52100 (secondary electron, 15 kV, 39 mm WD).

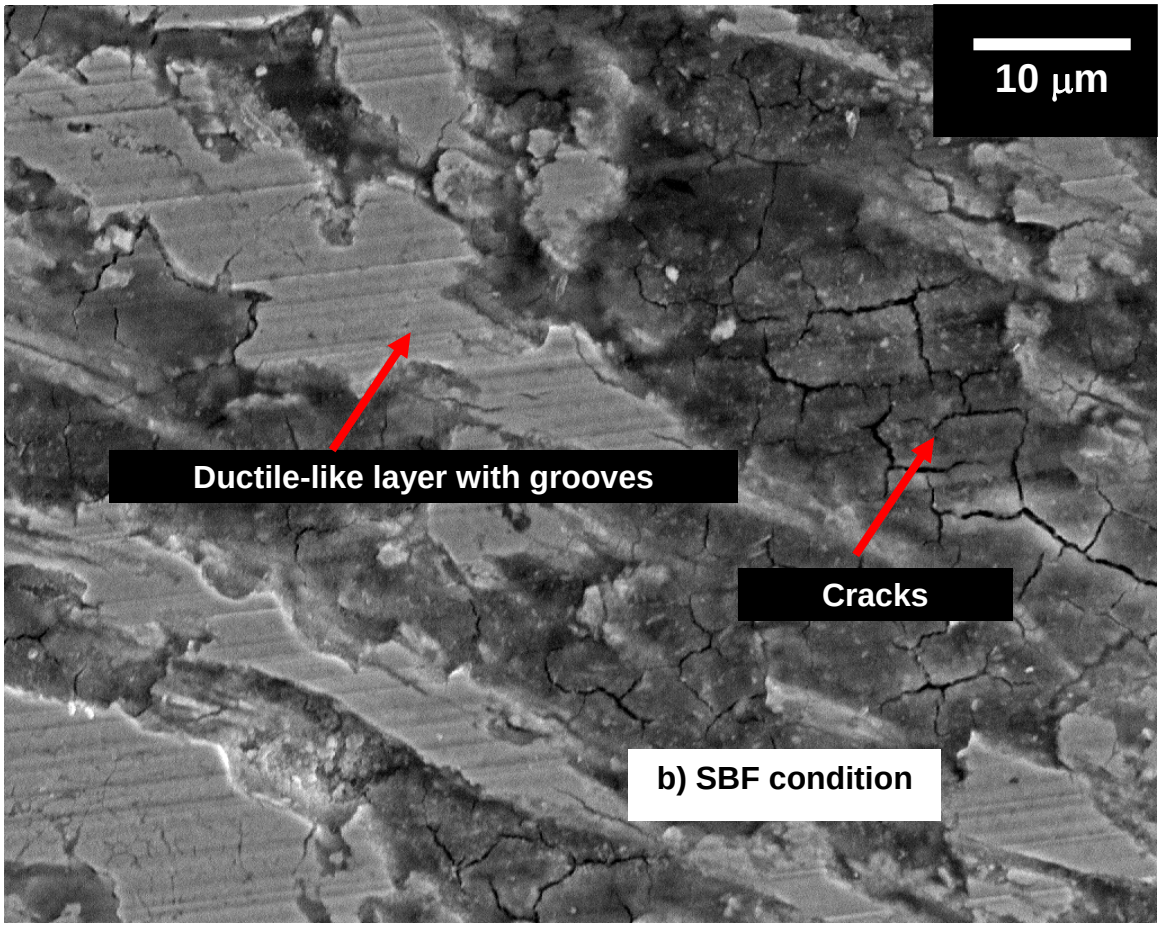

FIG. 5.16. (continued).

To understand these behaviors, we conducted X-ray crystallography analysis on the boride surfaces before and after the friction experiments. Fig. 5.17a is the X-ray diffraction pattern of as-received boronized niobium. It shows the existence of Nb, NbB_2 and NbB phases. Fig. 5.17b shows the spectra obtained on the debris generated from the dry and SBF tests, superimposed on the as-received surface pattern. There are peaks indicating the presence of oxides of Fe (Fe_3O_4, Fe_2O_3). The spectrum obtained from the debris generated during the SBF test indicates the presence of Niobium (V) oxide (Nb_2O_5).

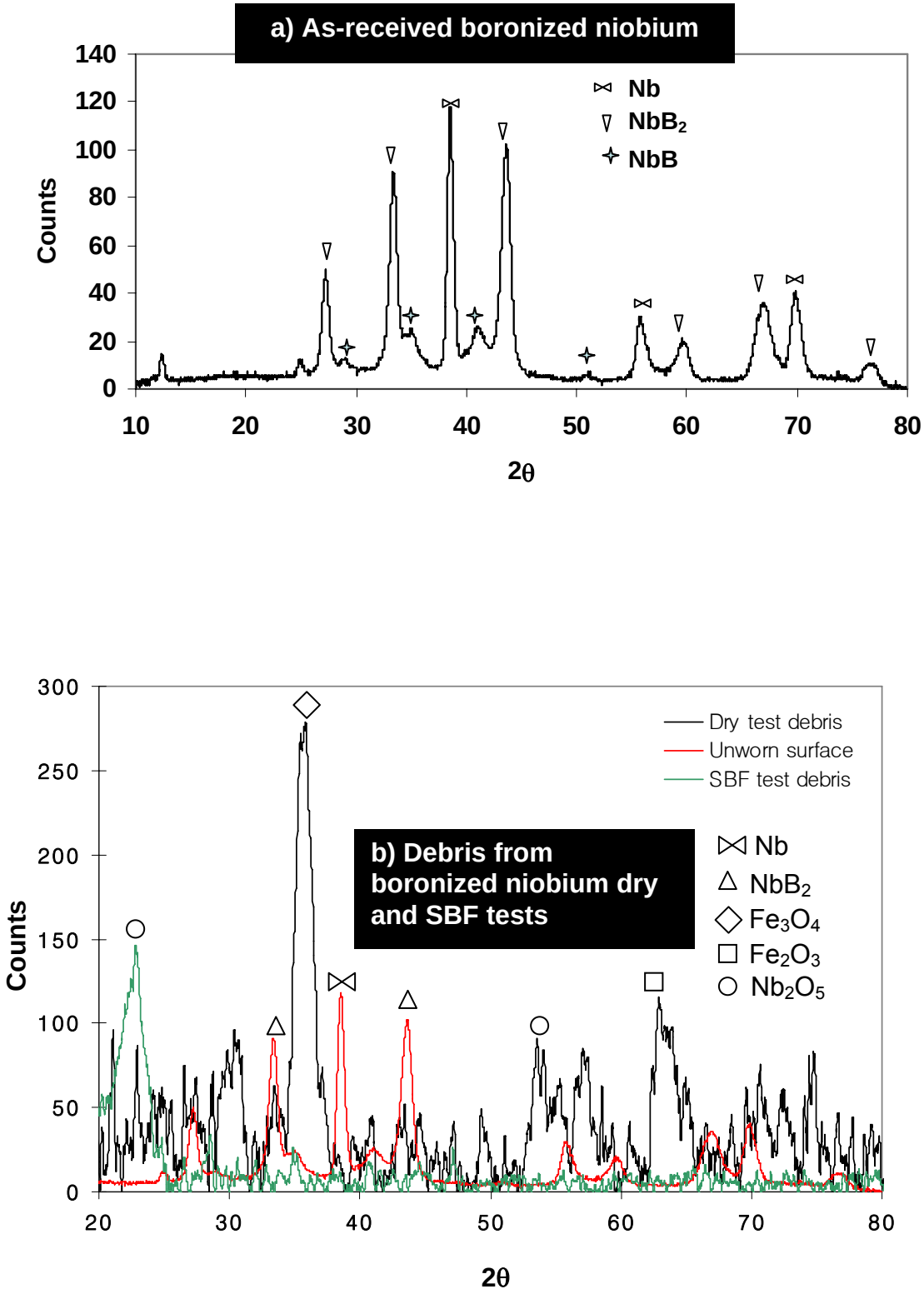

FIG. 5.17. X-ray diffraction pattern.

In Fig. 5.18a, the TEM image of the debris obtained from the dry condition test shows mixed amorphous and crystalline structures. In Fig. 5.18b (TEM image of debris from the SBF condition test), the amorphous phase fraction is less than that of the dry tests. There are mixed crystalline phases possibly from the metals as well as from salts contained in the SBF. Detailed discussions will be carried out in the next chapter.

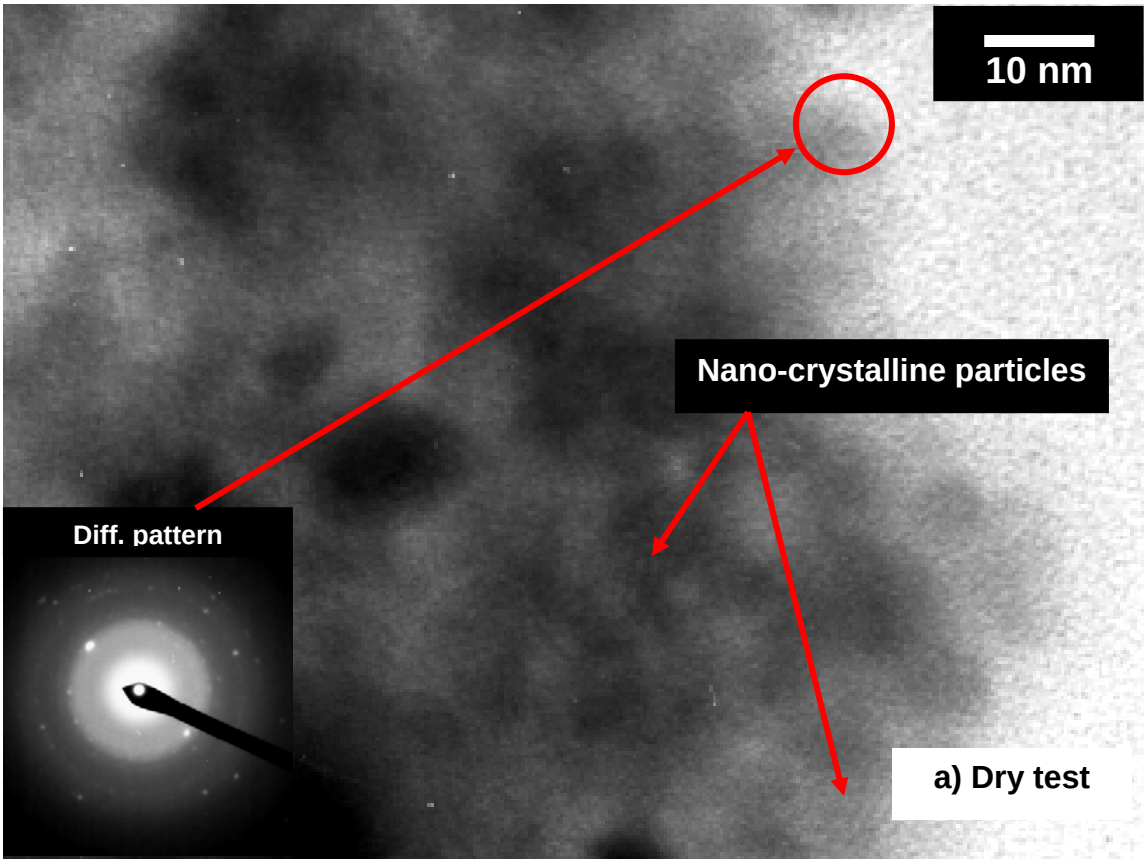

FIG. 5.18. TEM of wear debris from dry and SBF tests (boronized niobium, 200 kV working voltage).

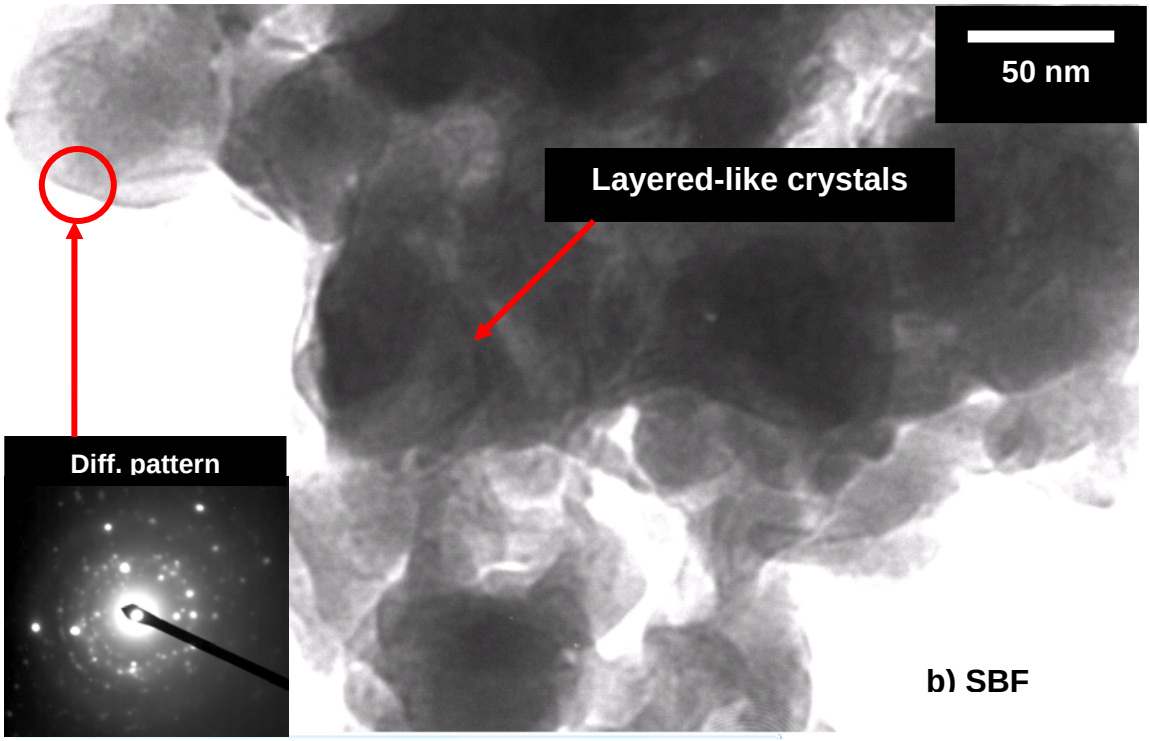

FIG. 5.18. (continued).

3. Boronized Tantalum

Frictional Behavior

Figure 5.19 is a plot of the coefficient of friction against time for tests conducted under dry and SBF conditions. For the dry test, there is a well defined running-in period where the coefficient of friction rises to a maximum value of approximately 0.44 at 1875 cycles after starting the test. The friction coefficient decreased thereafter and stabilized at a value of approximately 0.34 for the rest of the test. For the test conducted under SBF conditions, there was no well defined run-in period. The coefficient of friction rose from zero to a value of approximately 0.4 in the first 1875 cycles of the test. It thereafter varied between 0.32 and 0.4.

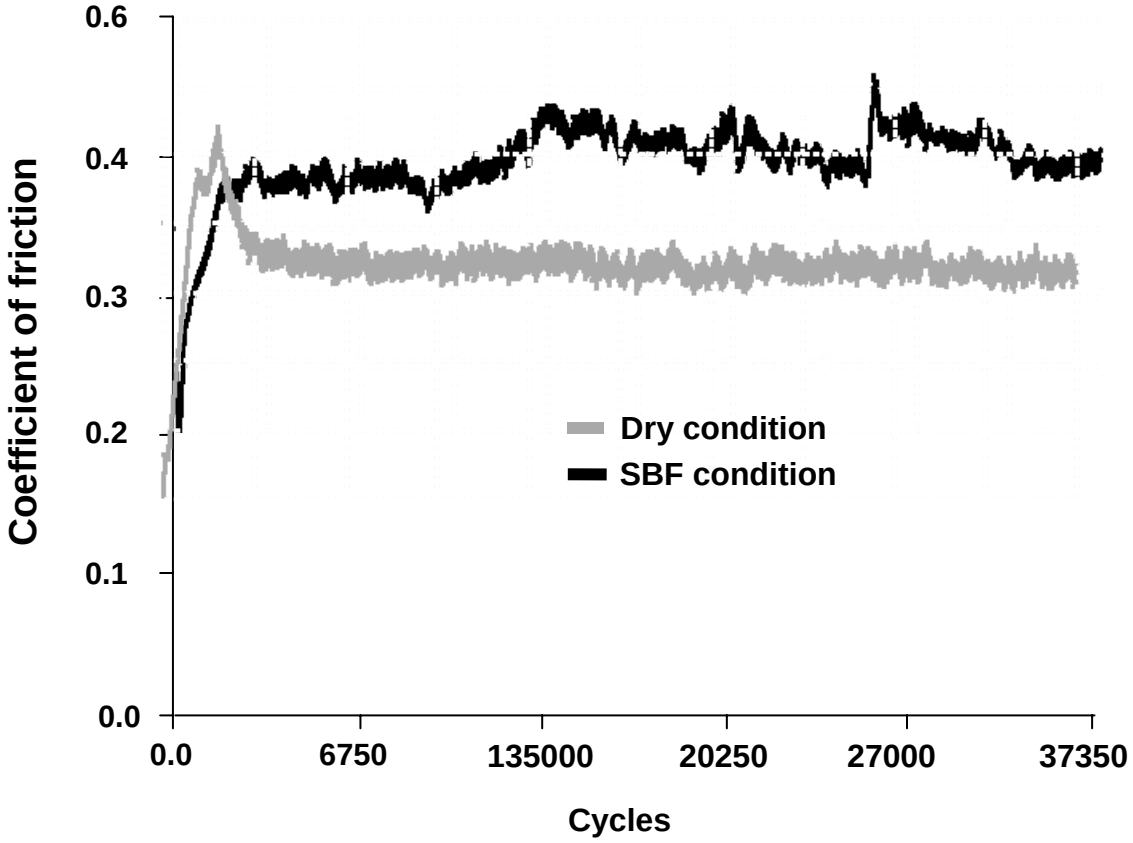

FIG. 5.19. Coefficient of friction against cycles for boronized tantalum against E52100.

Wear Track Analysis

Figure 5.20 is an AFM image with roughness values of the unworn boronized tantalum surface. The average roughness was found to be ~107 nm. Figure 5.21 is the SEM image of the wear track on boronized tantalum for a test conducted under dry conditions. There are cracks on the wear track that are perpendicular to the sliding direction. Figures 5.22a and b are SEM images of the wear tracks for a test conducted under SBF conditions. Fig. 5.22a shows flakes of delamination due to subsurface

fracture. Fig. 5.22b shows inter-granular cracks formed due to possible tribochemical wear.

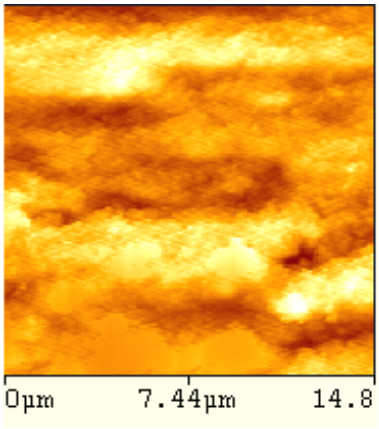

	Whole Area
Total Area St.	221.45 µm²
Roughness Avg. Sa:	107.43 nm
Root mean square sq:	134.35 nm
Mean Sm:	631.18 nm
Range Sr:	1018.84 nm

FIG. 5.20. AFM image and roughness values of unworn boronized tantalum surface.

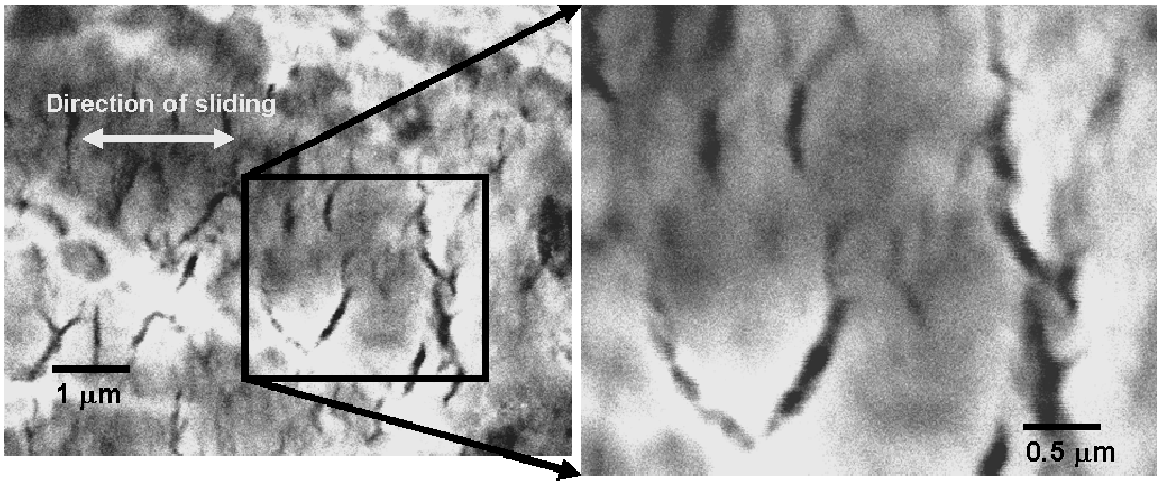

FIG. 5.21. SEM image showing cracks perpendicular to sliding direction for dry test (boronized tantalum, secondary electron, 15 kV, 39 mm WD).

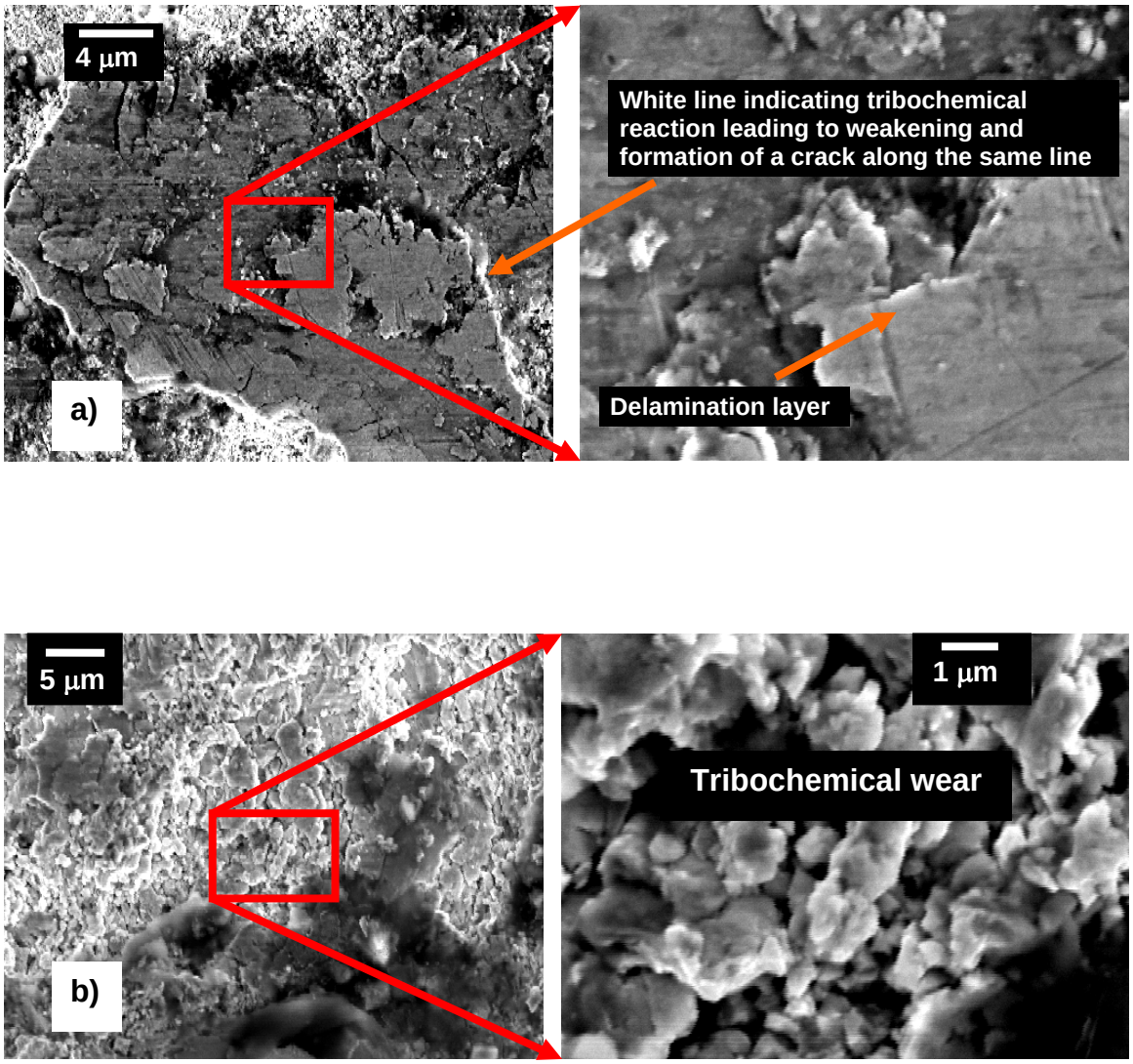

FIG. 5.22. SEM image under SBF conditions (boronized tantalum, secondary electron, 15 kV, 39 mm WD).

X-ray Diffraction

The x-ray diffraction pattern results are shown in Figs. 5.23a and b. Figure 5.23a is the spectrum obtained on the unworn boronized tantalum. Tantalum has three distinguishable peaks at ~38, 56, and 69 respectively. Figure 20b is the X-ray diffraction

pattern from the debris generated in dry and SBF conditions, superimposed on the pattern obtained on the as-received surface. Under dry condition, there is evidence of the existence of iron oxide (Fe_2O_3). Under SBF conditions, however, the types of oxides found were different, as shown in Fig. 5.23b. Here, peaks for sodium potassium borate (KNa_2BO_3) and TaO_2 are clearly seen.

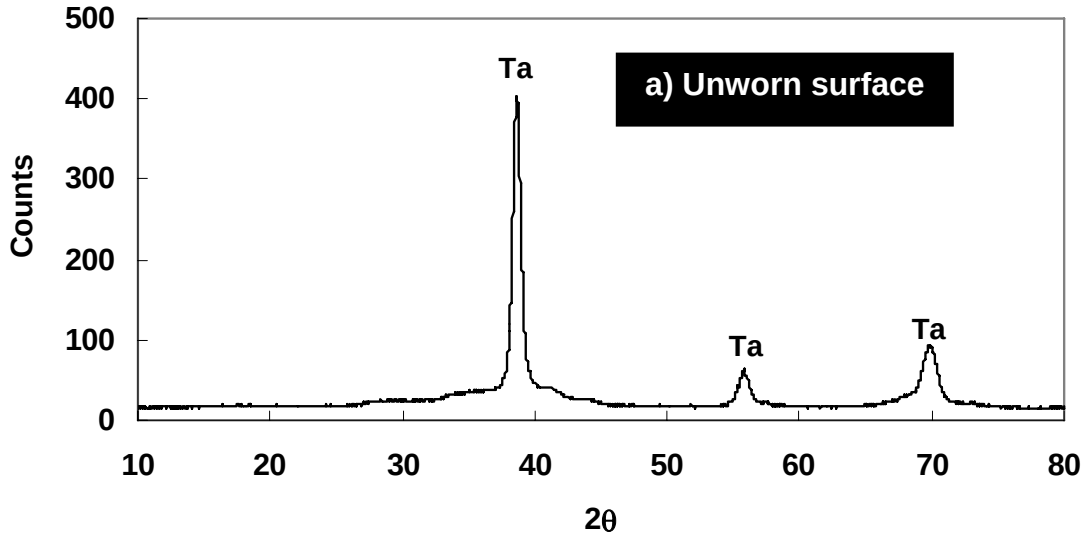

Fig. 5.23. X-ray diffraction pattern for boronized tantalum.

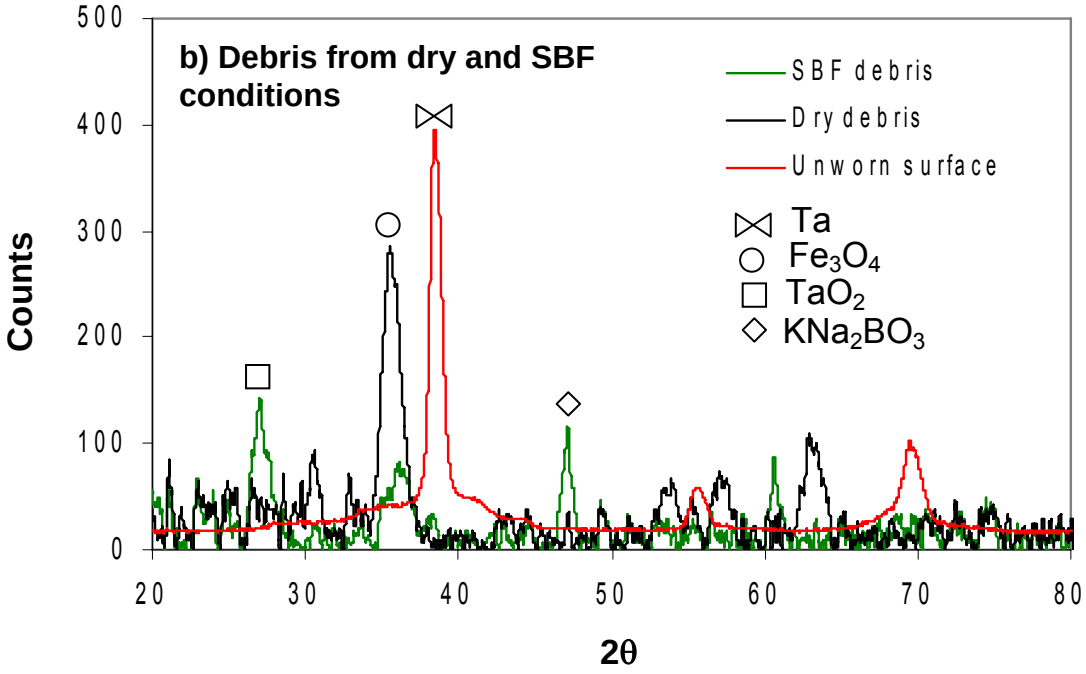

Fig. 5.23. (continued).

Debris Analysis

Figure 5.24a is a TEM micrograph of the wear debris generated under dry sliding conditions. There are agglomerated particles in the nanometer size range. The HRTEM image shows the presence of nanocrystals. The inset diffraction pattern shows rings formed by the nanocrystals present.

Figure 5.24b is a TEM micrograph of the debris generated under SBF conditions. Here too there are nanometer sized agglomerated particles. The diffraction pattern shows even smaller grain sizes due to the continuous rings (nano-crystalline to amorphous).

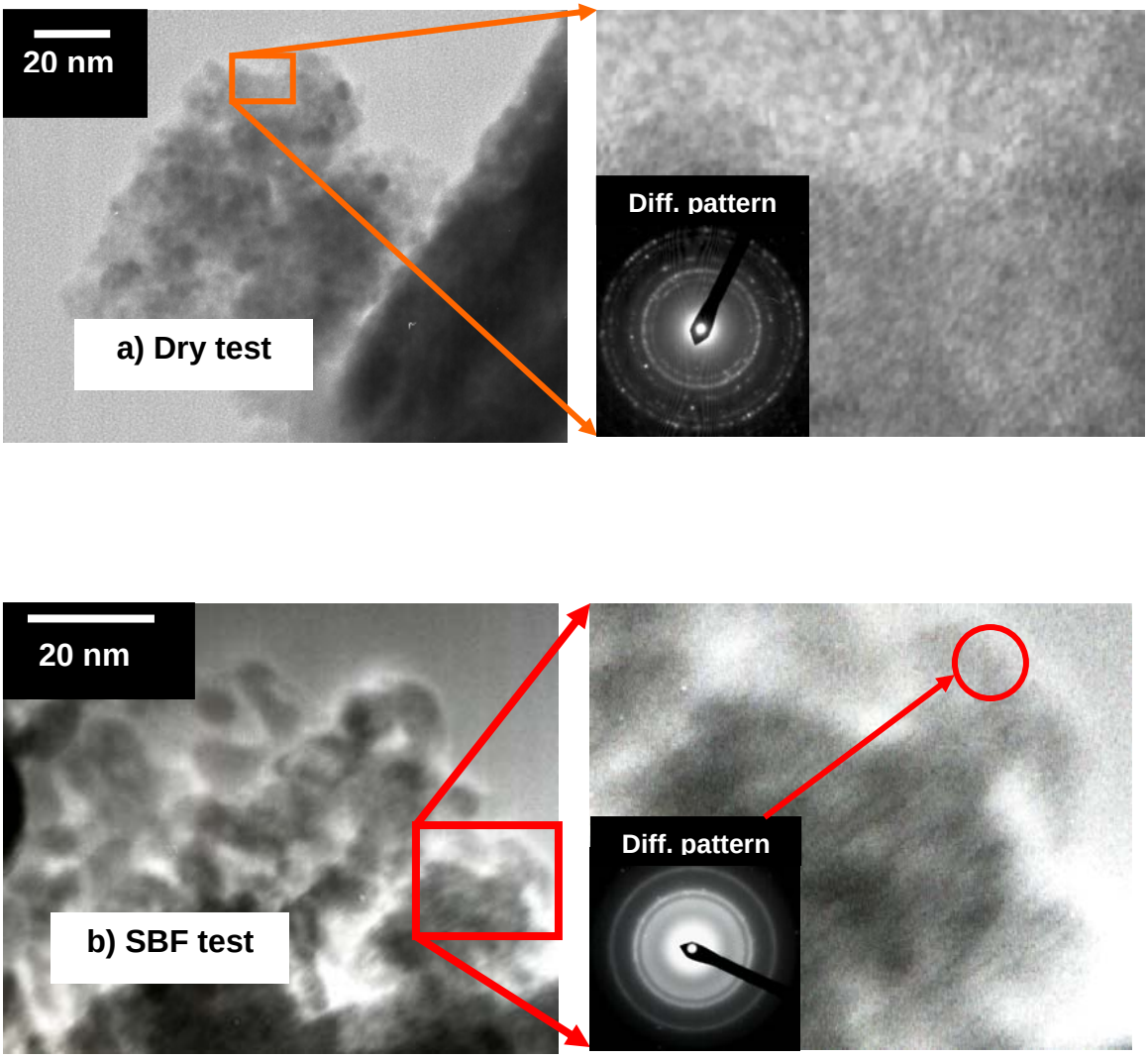

FIG. 5.24. TEM image of wear debris from boronized Ta (inset: diffraction pattern, 200 kV working voltage).

4. Comparison of wear and friction of Ti6Al4V, Ta, Nb, boronized Ta and Nb

The wear tracks were analyzed when worn against a comparatively hard material E52100 in dry condition. The sliding speed chosen was 1.5 cm/s in order to closely simulate natural joint conditions. The sliding motion was linear reciprocating with an

amplitude of 3 mm. Simulated synovial fluid (SSF) was used as a lubricant. This information would more closely resemble natural joint implant conditions.

Figures 5.25a to c are AFM images with roughness values of the unworn Ti6Al4V, pure niobium and pure tantalum surfaces respectively. Figs. 5.26a to c are plots of the coefficient of friction versus number of cycles. Figures 5.27a to e are corresponding AFM topography (left) and phase (right) images of the wear tracks of Ti6Al4V, Nb, boronized Nb, Ta and boronized Ta respectively, when worn against bearing steel E52100. In Fig. 5.27a, there is an indication of long, somewhat cylindrical particles on the surface. These particles would tend to roll and cause a varying COF as can be seen in the COF-cycles plot in Fig. 5.27a. After certain amount of particles accumulated, the friction coefficient stabilized at around 0.6. There are intermittent drops in the COF. Figure 5.27b shows the AFM topography and phase images of the wear track of Nb. There are typical abrasive wear grooves on the surface. The phase image indicates the presence of debris and grains of different phases. The phases could probably be oxides due to the increased temperature during sliding and reaction with air. The friction curve (Fig. 5.26b) indicates a typical run-in period until asperities on the surface are removed. After this, the COF varied between approximately 0.7 and 0.9.

The wear track for boronized Nb (Fig. 5.26c) indicates a great amount of roughness. The phase image looks very uniform throughout. The friction curve indicates no run-in period. There is an initial increase in COF, followed by a gradual decrease after which it stabilized around 0.65 (Fig. 5.26b).

The plain Ta wear track indicates deep pits caused due to material pullout (Fig. 5.27d). The phase image indicates the presence of two major phases. On the left is a phase present with pointed asperities. On the right, there are more rounded asperities with some indication of inter-granular-like fracture. The friction plot shows a clear running-in period after which the COF decreased and stabilized at approximately 0.7 (Fig. 5.26c).

The topography image of boronized tantalum (Fig. 5.27e) indicates the presence of cracks and flattened areas. The phase image is predominantly uniform except for the cracks that show up as a different phase due to tilting of the AFM probe. The friction curve for boronized Ta does not have a running-in period. There is a rise in COF to a value of approximately 0.7, right at the beginning and it remains at this value for some time. It later decreased and stabilized at a value of approximately 0.6 (Fig. 5.26c).

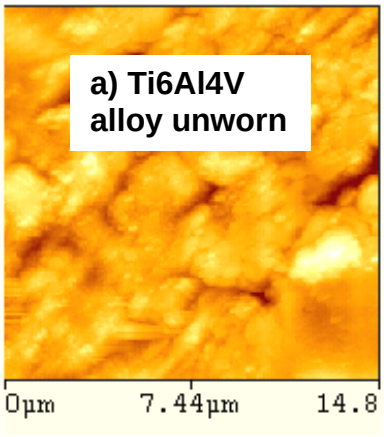

	Whole Area
Total Area St.	221.45 µm²
Roughness Avg. Sa:	30.30 nm
Root mean square sq:	42.18 nm
Mean Sm:	289.31 nm
Range Sr:	454.65 nm

FIG. 5.25. AFM image and roughness values for Ti6Al4V alloy.

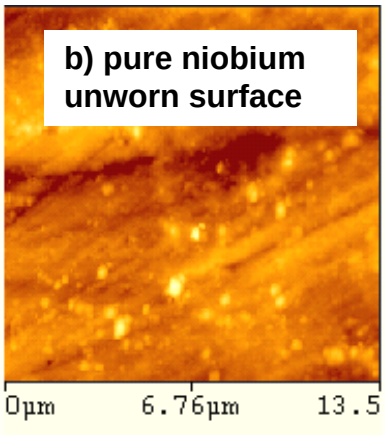

	Whole Area
Total Area St.	183.02 µm²
Roughness Avg. Sa:	16.96 nm
Root mean square sq:	23.84 nm
Mean Sm:	80.45 nm
Range Sr:	343.17 nm

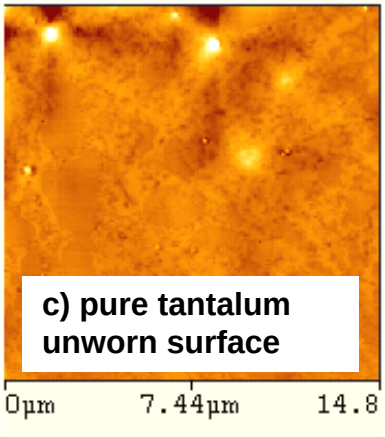

	Whole Area
Total Area St.	221.45 µm²
Roughness Avg. Sa:	3.00 nm
Root mean square sq:	4.84 nm
Mean Sm:	47.62 nm
Range Sr:	140.53 nm

FIG. 5.25. (continued).

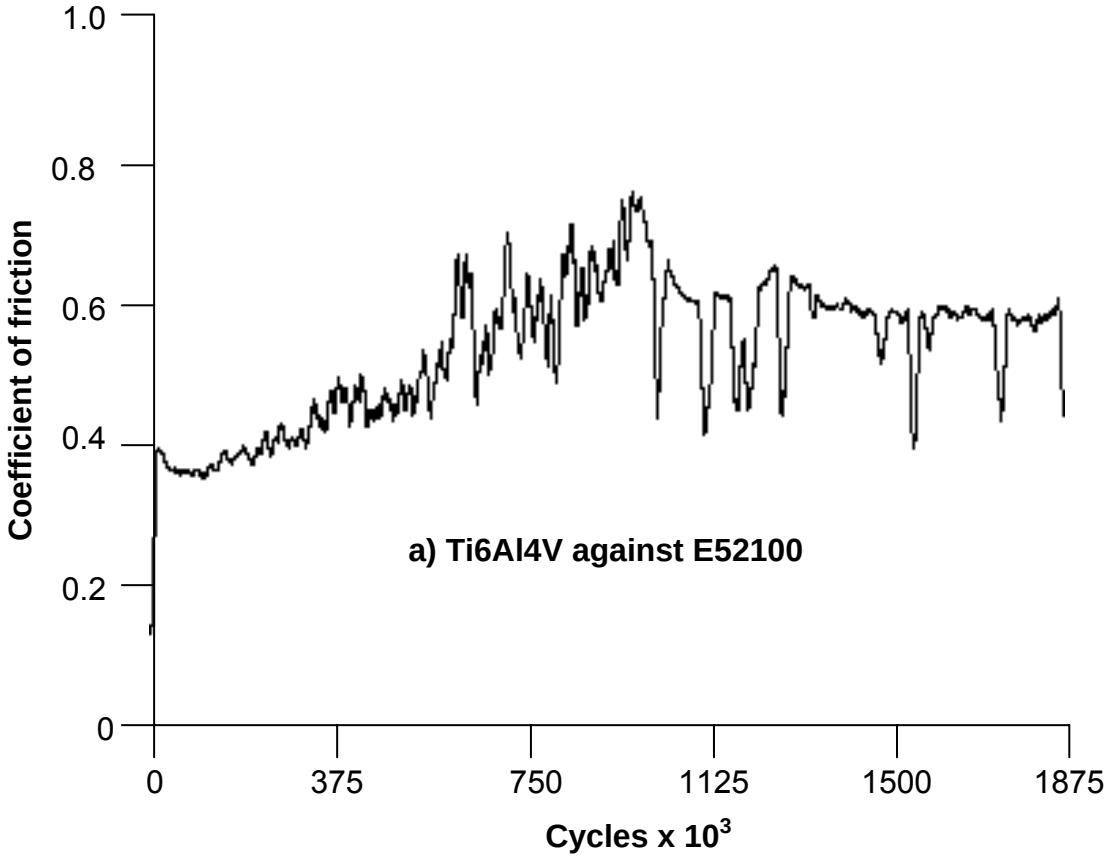

FIG. 5.26. Coefficient of friction against cycles.

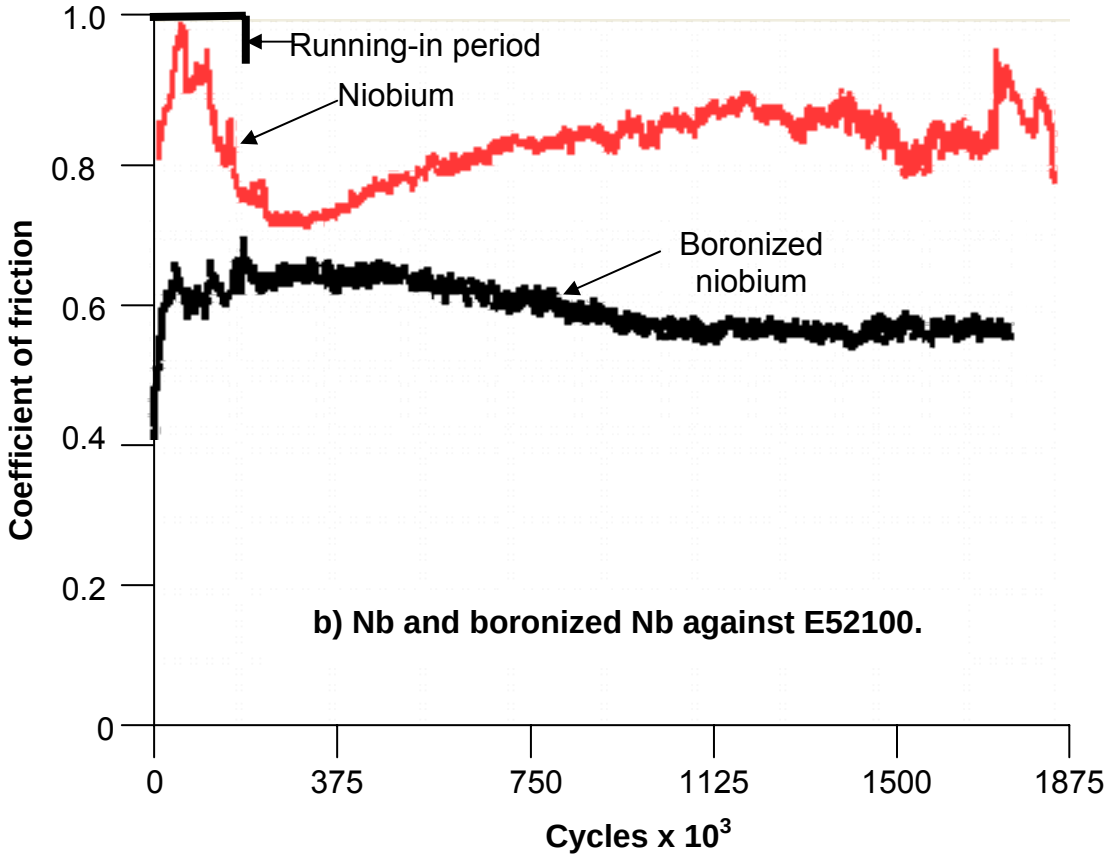

FIG. 5.26. (continued).

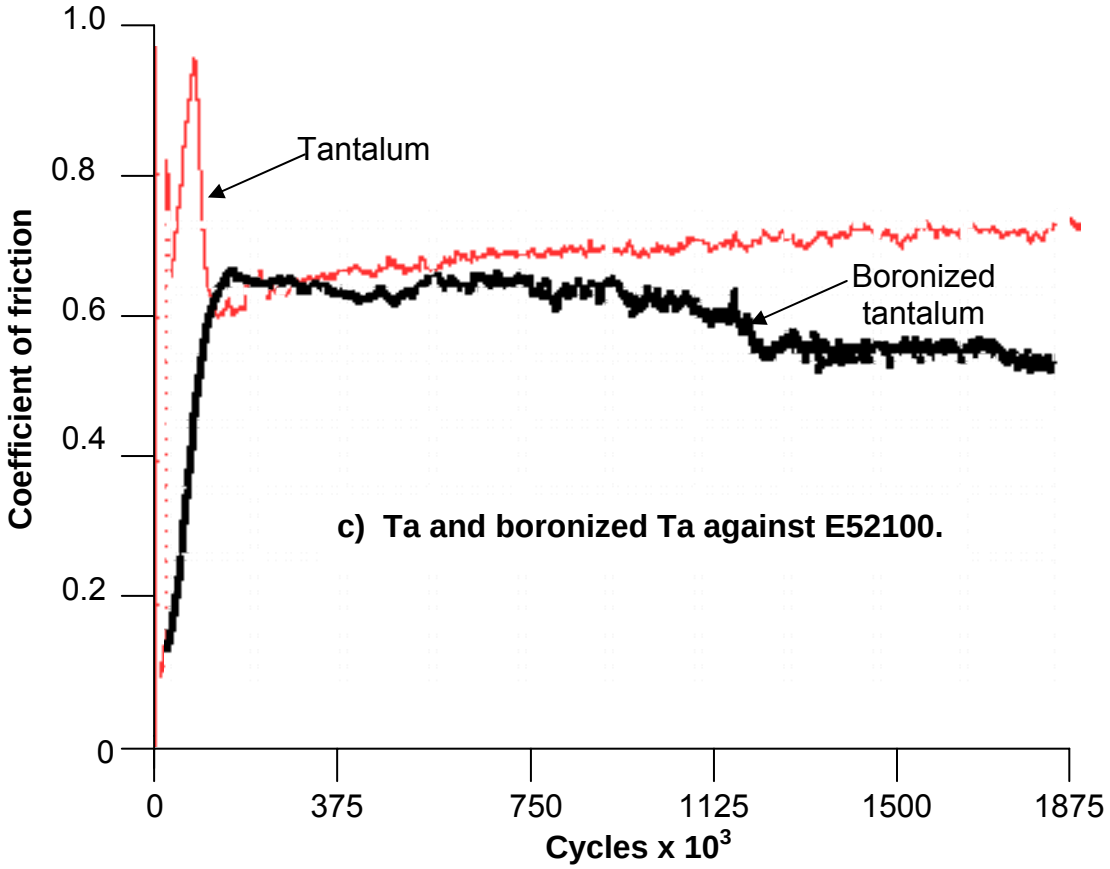

FIG. 5.26. (continued).

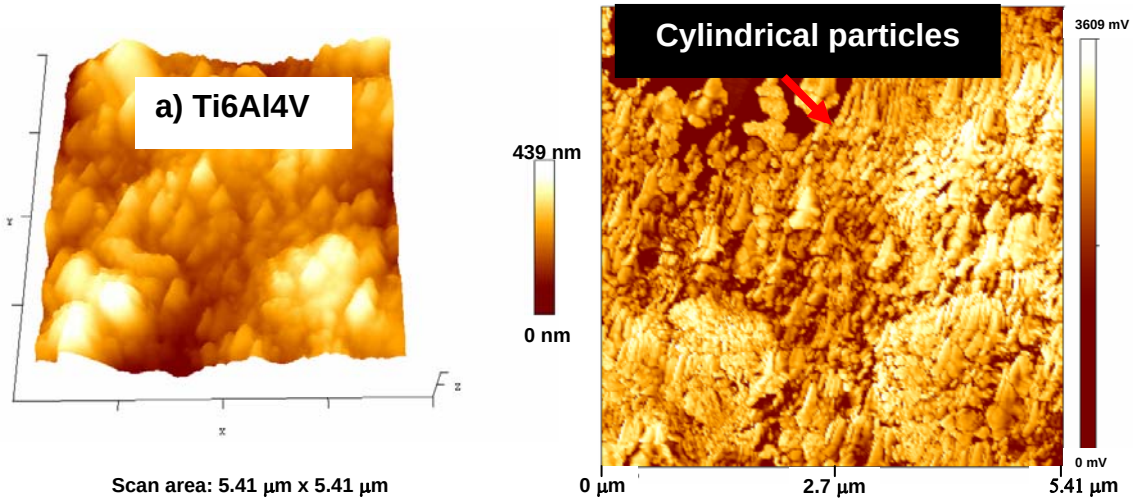

FIG. 5.27. AFM topography (L) and phase (R) images of wear track.

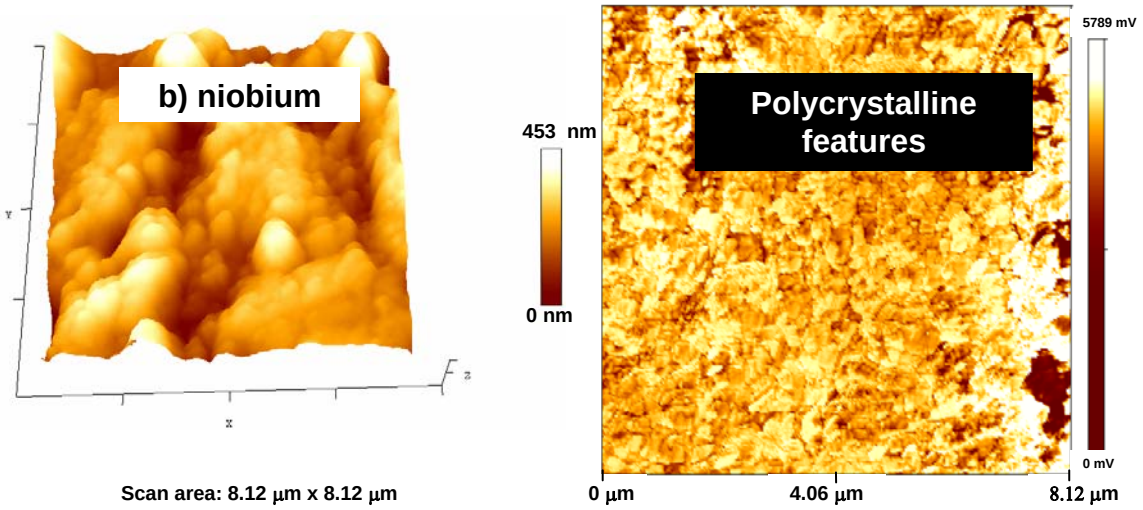

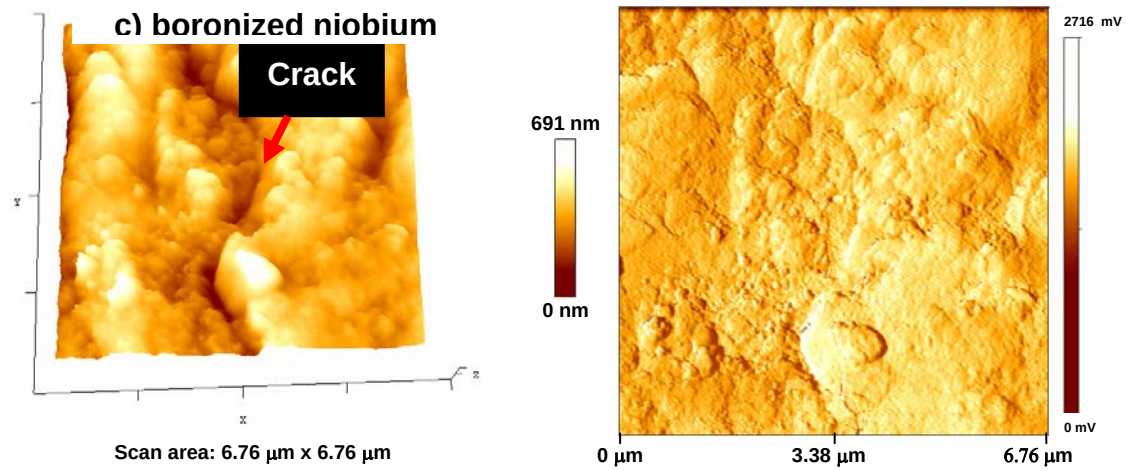

FIG. 5.27. (continued).

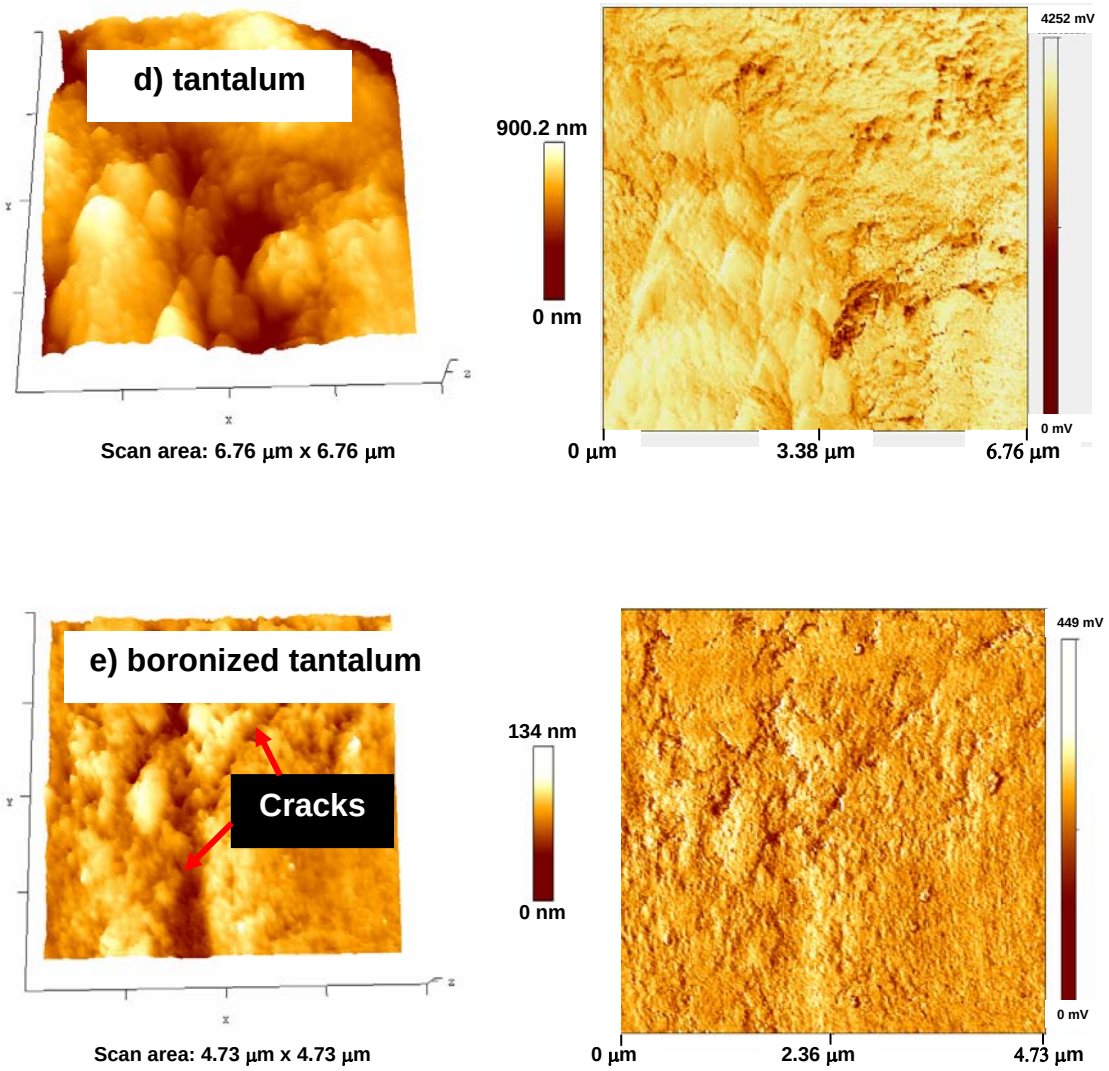

FIG. 5.27. (continued).

Figure5.28 illustrates the average coefficient of friction for Nb, Boronized Nb, Ta boronized Ta, and Ti6Al4V alloy when articulated against UHMWPE in the presence of SSF. There is not much variation in the average COF among these materials and varied around 0.1. There were four tests conducted for each material. Detailed discussions on tribological mechanisms will be conducted in the next chapter.

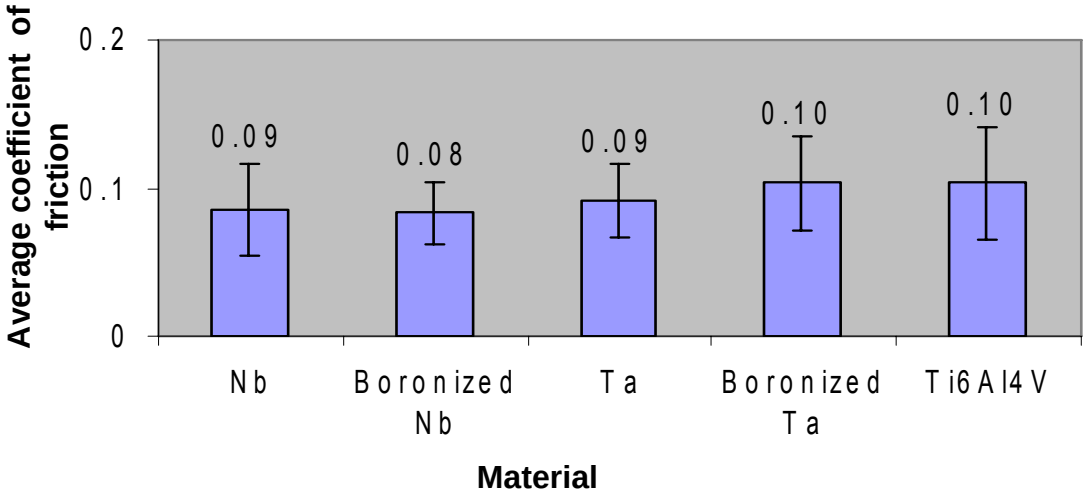

FIG. 5.28. Average coefficient of friction of tested metals against UHMWPE.

CHAPTER VI

DISCUSSION

A. POLYMER COMPOSITE FOR TISSUE ENGINEERING

In Chapter I, the positive biocompatibility of PTMC and suitable adhesion of chondrocyte cells were discussed. The greatest drawbacks of tissue culture of cartilage are insufficient mechanical strength of the scaffold material and generated tissue, and weak bonding to the underlying bone. The pristine PTMC samples that were subjected to nanoindentation tests were too weak for consideration and could not withstand loads of over 50 μN without catastrophic deformation. In Fig. 5.3b, we observe a scanned area of approximately 10 μm^2 of the surface of a PTMC that was mixed with hydroxyapatite (HAP) polymer and multi walled nanotubes, prior to polymerization. This composite was able to withstand nanoindentation loads of 200 μN and the deformation was similar to that of cartilage. The coefficient of friction was also fairly low when articulated against cartilage. The final surface obtained has protrusions (probably hydroxyapatite) upto a maximum height of ~400 nm. The HAP particles are not evenly spread over the surface. Adequate mixing prior to and during polymerization could help evenly distribute the polymer. These protrusions of HAP can possibly enable bone growth when the polymer is implanted in the place of cartilage. There is also a nanotube-like structure that is coming out of the PTMC and lying along the surface. Surface functionalization of nanotubes can render them hydrophilic, similar to natural cartilage. This can enhance the water and nutrient absorption property of the cartilage for cell culture. The nanotubes also have damping characteristics (being hollow). The sliding behavior of nanotubes

over different materials can be different. In the case of our generated composite, the coefficient of friction was rendered fairly low possibly due to the combination of the different surface interactions and damping behavior of the nanotubes. The mechanical strength also showed adequacy for cartilage implants. The strength and friction properties showed an improvement over conventional total joint replacement polymer UHMWPE. The degradation rate can be modified by changing the crystallinity of the bulk PTMC and by changing the reactivity on the nanotube surface. Carbon nanotubes have shown sufficient biocompatibility and hydroxyapatite forms a major proportion of the mineral content of bone.

Fig. 5.2 shows the average friction coefficient obtained for each material against articular cartilage. The lowest coefficient of friction was obtained for cartilage from the femoral condyle against cartilage from the tibial plateau (0.0525). PTMC+HAP+NT had the next lowest average friction coefficient (0.06). Cartilage against UHMWPE had the highest friction coefficient (0.1075). This gives an indication that surface properties of polymers can be varied to bring the friction coefficient close to that of natural joints. A major drawback of the test was the fixation of polymeric materials to the subchondral bone with superglue. As these were not in vivo experiments, we could not implant the material and test for bone ingrowth.

Nanoindentation force-distance curves (Fig. 5.1) show that PTMC+HAP+NT has an elastic behavior similar to that of cartilage though cartilage proved to be stiffer. UHMWPE showed a much softer response, with higher deformation, than any other

material while subchondral bone was the stiffest. This indicates that our composite material is not likely to provide stress shielding effects if implanted.

Variation of PTMC molecular weight and/or crystallinity can alter its degradation rate and optimize it for cell growth applications. The compressive modulus and strain of cartilage obtained can be compared with that obtained from other research studies of cartilage and of future developed biomaterials. Items for future work leading from this research would be to control the distribution of component material, alignment and functionalization of nanotubes and possible cell attachment and growth tests on and within the composite material.

B. POLYIMIDE-SWNT COMPOSITE

The goal of replacing UHMWPE as a component in joint arthroplasty requires the development of a material that possesses its benefits as well as exhibits fewer of its drawbacks. It is required to have a biomimetic, biocompatible material that possesses a low wear rate and whose wear particles are well taken care of by the body's immune system. Polyimides have proven to be biocompatible. They also possess high mechanical and thermal strength and are thus used to replace metals in various applications. Being a polymer, it is also deformable and its properties can be tailored during synthesis. Single walled carbon nanotubes have a diameter in the nanometer range and a length in the micron range. They may therefore suitable for replacing natural fibers such as collagen or provide reinforcement to weak tissue. They also possess high thermal conductivity and mechanical strength.

The combined advantages of polyimides and nanotubes were investigated. Nanoindentation tests on polyimides combined with different weight percentages of SWNTs exhibit an interesting trend (Figs. 5.5 and 5.6). The contact stresses on a natural cartilage surface within a joint, under bulk investigation, are in the range 3 to 20 MPa [153, 154]. The stresses obtained from nano-indentation are highly localized and orders of magnitude higher than the bulk values. The deformation during the dwell period is higher for the pristine PI sample as compared to the PI + NT samples. This indicates that the viscoelastic response of the composite surfaces is lower than that of the pure PI surface. This can be due to the effect of PI-NT and NT-NT surface interactions. However, the deformation during varying stress is higher for the composite samples than for the pristine PI sample.

In order to compare the stiffness of PI + NT samples on a single plot, the change of stress per nanometer indentation depth was calculated as the slope of the loading region of the respective curves in Fig. 5.5, at an indentation depth of 75 nm, and plotted (Fig. 6.1). It is seen that the stress change per nm indentation depth is the highest for pristine PI. It decreases to a minimum at approximately 0.2% NT concentration, and thereafter increased and stabilized. This plot can be modeled as:

$$E\rho = Ax^2+Bx+C, \quad (3)$$

Where Eρ is the stress change per unit indentation depth and **x** is the %NT concentration in PI. A, B, and C are coefficients. The following table gives the values of A, B, and C for different values of x and Eρ obtained empirically. Eρ has the units of force/volume and hence can be defined as the ‘specific force’.

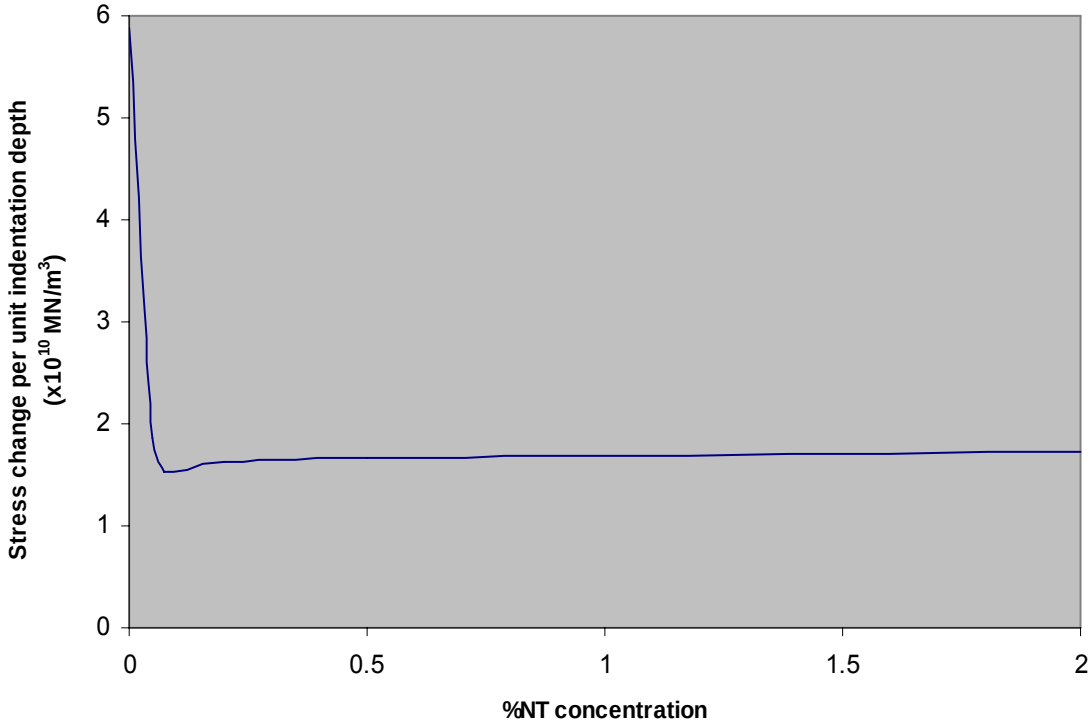

FIG. 6.1. Stress change per nm indentation versus %NT in PI

TABLE 5.1. Nanotube concentration, specific force, and modeled coefficients.

x	Eρ ($x 10^{10}$ MN/m^3)	A ($x 10^{10}$ MN/m^3)	B ($x 10^{10}$ MN/m^3)	C ($x 10^{10}$ MN/m^3)
0	5.875	Any value	Any value	5.875
0.05	0.6	-20	-80	5.875
0.075	0.5	-20	-55	5.875
0.2	0.55	-18	-18	5.875
0.5	0.8	-11	-2.9	5.875
2.0	0.9	-1	-0.075	5.875

It is seen that the coefficients A and B can take on any value when %NT = 0, and the remaining constant C takes on the value of Eρ (which is 5.875). As the %NT increases, the values of coefficients A and B increase (keeping C constant), but remain negative. The value of **A** increases at a slower rate than B and the values are identical at

0.2%NT (minimum stress change point). The change in the value of these coefficients can be attributed to the different surface interactions, and nanotube deformation taking place within the composite. The increase in deformability at a certain NT percentage followed by subsequent decrease indicates that the behavior of PI+NT composites can be tailored by varying the NT concentration. UHMWPE proved to be much softer than cartilage or the PI+NT during the early stages of loading but showed an opposite trend at higher loads. This behavior could be a cause for the discomfort felt by patients having UHMWPE joint implants. The minimum in the COF (Fig. 5.7), occurs at a %NT concentration in the same range as the minimum in stress change per nm. (0.2-0.5%NT). The AFM images (Figs. 5.9e and f) indicate a transition from amorphous to a crystalline structure at these %NT concentrations. This indicates that a semi-crystalline configuration leads to a minimum in COF. Fig. 5.9 compares the COF trend vs. NT concentration for three different regimes indicated. PI-cartilage combination had the lowest COF. At lower NT concentrations, there was not much difference in the COF under dry and SSF conditions against Ti6Al4V. At higher concentrations however, as expected, the COF for the dry condition was higher. In both cases, the minimum COF occurred at %0.5 NT concentration. In Fig. 5.10a, we can see that SWNTs exist in the form of agglomerated bundles. The resulting dimensions of a bundle are much larger than that of individual nanotubes. This can affect the mechanical and tribological properties of the composites. The sliding behavior between two nanotubes and nanotube and PI are most likely to be different due to the different morphologies and chemical structures. In Figs. 5.10b and 5.10c we can see that the nanotubes act as tear arresters.

The nanotubes show good bonding with the surrounding PI and the PI tears more easily around the nanotubes. This indicates that proper distribution of nanotubes and in a specific orientation can lead to reduced wear of the composite surface. Coming to the AFM images, there is again indication of a difference for NT concentrations of 0.2 and 0.5% compared to other concentrations, with respect to the wear pattern. Pristine PI shows typical abrasive wear grooves with certain amount of adhesive tearing, leading to tears standing more or less vertically on the surface. For 0.05%NT, there are abrasive grooves as well as mild striations perpendicular to the sliding direction. These striations are possibly caused due to folding of the polymer due to compression of the surface layer and/or crystallization in that direction. In the case of 0.1%NT, these striations are more pronounced. This indicates that the nanotubes cause the polymer chains to orient in the direction perpendicular to sliding. For 0.2% and 0.5%NT, the surfaces tend to be much softer (due to the lower mV. Values in the phase image), with a pit-like appearance on the surface. The maximum height variation is also much lower, in the range 40 to 60 nm. Fig. 11d. indicates long trenches possibly left behind by nanotubes being pulled out of the surface. This could be due to the increased softness of the polymer allowing the nanotubes to tear out. For 0.5%NT, the pits seem to be larger than for 0.2%NT. Figs. 10f. and g indicate more brittle like surfaces for 1% and 2% NT concentrations with a metal grain-like structure for 2%NT.

From the above discussion, we can conclude that at a percentage NT concentration in the range 0.2 to 0.5 wt. %, PI-NT composites have a unique behavior. Overall, there is a transition from a harder but ‘not very brittle’ surface character at

lower concentrations, to a soft, highly deformable character at 0.2 to 0.5%NT, followed by a hard and brittle character at higher concentrations. The effects of nanotubes lie not only in strengthening the polymer, but also in their mutual surface interactions and deformability. Interactions between nanotubes are of two forms, as shown in Figs. 6.2 and 6.3. Undeformed nanotubes can absorb the impacts of loads and also slide against each other (as there is no chemical bond between adjacent nanotubes). At higher nanotube concentrations, the surface tends to be more crystalline due to the orientation of groups of nanotubes in the same direction. The nanotubes also tend to get compressed to the limit (Fig. 6.3) and are not able to absorb applied loads. This leads to high loads on the interacting surfaces and an increase in COF. At low %NT concentrations there is insufficient sliding between nanotubes and therefore the COF is high.

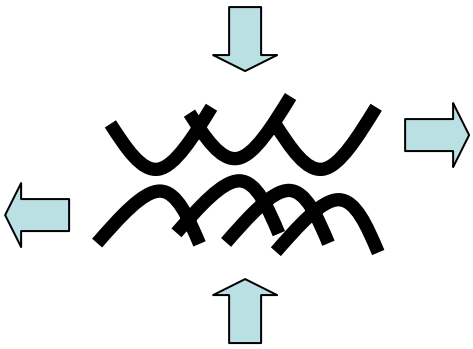

FIG. 6.2. Interfacial sliding of undeformed nanotubes

These characteristics of nanotube deformability and surface interactions can cause the friction and modulus trend noticed. In the range 0.2% to 0.5% NT concentration, there could be high efficiency of sliding and deformability leading to the low values of modulus and COF. The nanotubes are strongly attached strongly to the PI

matrix (as seen in Figs. 5.8b and c) and there is assumed to be negligible sliding between the nanotubes and PI.

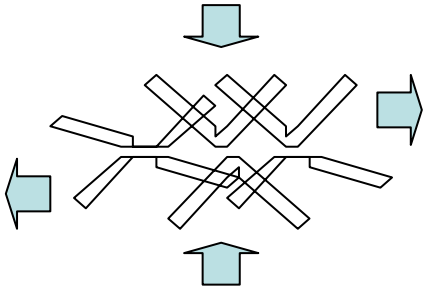

FIG. 6.3. Interfacial sliding of deformed nanotubes

C. METALS FOR TOTAL JOINT REPLACEMENT

1. Chromium and boronized chromium

Friction and Wear

Analysis of Fig. 5.13a suggests that asperity removal requires greater energy than under lubricated conditions for pure Cr. Fig. 5.14a shows fatigue failure along with some material transfer. Large fluctuations in the friction coefficient are possibly due to a stick-slip phenomenon. For boronized Cr there is indication of fatigue failure at and below the surface, leading to flakes coming off the surface and forming debris. This is due to the brittle nature of the ceramic CrB phase (Fig. 5.12). Under SBF conditions, the run-in period is much smaller and so is the COF during this period for pure Cr. The low COF with SBF is probably caused due to the presence of ions which could adhere to the surfaces and also react with the surfaces. Figure 5.14b indicates that the wear mode is mostly abrasive. For boronized Cr under SBF conditions also the friction coefficient is low. Fig. 5.14b suggests that there is abrasive wear as well as cracking (similar to mud

drying in dry weather). A closer look at the debris from the SBF tests (Fig. 5.15) indicates that there is a layer like structure present. This layer-like structure is possibly the cause for the low COF under SBF conditions due to the ease of sliding of one layer over the other. In order to determine the effectiveness of SBF as a lubricant, water was used as a comparison. The COF under water conditions for both Cr and boronized Cr was in between that of dry and SBF conditions. This indicates that the ions present in SBF are effective in decreasing the COF. Figure 5.13a indicates that pristine metal Cr has a definite running-in period under dry conditions whereas with a lubricant, there was no running in period. Fig. 5.13b indicates that boronized Cr had no running in period under all conditions. This indicates that boronizing of the surface causes a more gradual wear of the surface as compared to the pristine metal. Under SBF conditions, the COF was in a range acceptable for total joint replacements. These results show promise that Cr and its boronized counterpart could possibly be used as a total joint replacement material as far as tribological behavior is concerned. However, cracking of the surface does not indicate good mechanical characteristics. Further investigations into the wear particle size and biocompatibility are required to confirm suitability of these materials for joint replacements.

2. Boronized niobium

TABLE 6.1 Properties of Nb, boronized Nb and E52100 [155, 156]

	Nb	Boronized niobium	E52100
Vicker's hardness (HV)	110	2500	848
Elastic Modulus (GPa)	103	650	210
Density (g/cc)	8.6	6.88	7.81

Table 6.1 displays the hardness, modulus and density values of the tested materials. The hardness of boronized niobium is more than 20 times that of pristine Nb while it is approximately 8 times that of E52100 steel. It would be expected that wear of E52100 is faster than that of boronized niobium and slower when compared with niobium. Although the density of these three materials appear to be in the same range, the hardness and modulus of boronized niobium is much higher than those of E52100 and pure niobium. However, this high hardness is associated with greater brittleness and hence the crack development on drying (Fig. 5.18b). Moreover, the extent of boronizing and the hardness decrease with depth from the surface, into the material [157]. Fig. 5.18a indicates that E52100 steel tends to stick to the boronized niobium surface causing adhesive wear, under dry sliding conditions. From X-ray diffraction results (Fig. 5.19b) it can be seen that oxides of iron and Nb form. Under SBF conditions, there is evidence of only the oxide of Nb (Nb_2O_5) within the debris. This is the likely ductile layer phase on the surface (Fig. 5.18b). In SBF conditions, the temperature at the interface is likely to be lower due to evaporation and convection of the SBF. The temperature is likely to be too low for the formation of iron oxides. In order to determine exact chemical reactions taking place, in-situ techniques of phase and temperature determination is to be developed and incorporated. The adhesive wear mode (Fig. 5.18a) confirms the stick slip like friction pattern observed (Fig. 5.16). The removal of the running-in period in the SBF condition (Figure 5.16) indicates that the surface asperities are more easily removed or are rendered softer. Comparing with the SEM images of Figs. 5.18a and b, under dry conditions, there are abrasive grooves caused by harder surfaces and wear debris. Under

SBF conditions, there are ductile-like flattened patches with wear grooves interspersed, with brittle patches containing cracks. This is an indication of possible tribo-chemical reactions taking place under SBF conditions due to combination of the ions present and the temperature rise due to friction. TEM images show amorphous like debris (particles as well as diffraction pattern) for the dry test. Fig. 5.20a shows a complex crystalline diffraction pattern and layered like debris particles. The friction coefficient under SBF conditions is still too high for consideration for a metal on metal prosthesis. Articulating against a polymeric or ceramic material may show more promise.

3. Boronized tantalum

TABLE 6.2 Properties of Ta, boronized Ta and E52100

	Ta	Boronized tantalum	E52100
Vicker's hardness (HV)	156	3419	848
Elastic Modulus (GPa)	186		210
Density (g/cc)	16.6		7.81

In the case of boronized tantalum too, we find a definite running in period for the dry condition test. The running in period was eliminated in the presence of SBF, but amazingly the COF rose to a value higher than that under dry sliding conditions. The lower friction coefficient under dry conditions corresponded with a more crystalline debris as indicated in the TEM images (Fig. 5.26a). From X-ray diffraction results (Fig. 5.25a), Ta did not react with the boron atoms that diffused into the surface. Under dry conditions the most prominent peak was that of Fe_3O_4, caused by the reaction of iron in E52100 with air. Under SBF conditions, the prominent peaks were of reaction products

from the boronized tantalum surface. Sodium Potassium Borate (KNa_2BO_3) formed due to reaction of the ions in SBF with unreacted boron atoms in the boronized surface and oxygen. There was also a peak that corresponded with tantalum oxide (TaO_2). The lower oxygen percentage could be a result of shielding of atmospheric oxygen by the SBF. SEM images indicated brittle cracks formed under dry conditions whereas delamination and intergranular cracks formed under SBF conditions. The intergranular cracks are lined bright probably due to charging caused by interaction of electrons with reaction products. These findings do not show boronized tantalum as a promising material for joint replacements. The dry test showed a more crystalline diffraction pattern from the debris as compared to the SBF condition.

The above discussion behavior of boronized metals and pristine Cr can be summed up that higher friction coefficients correspond with the generation of more amorphous debris. Except for the case of boronized Cr, the friction coefficients are too high for the materials to be considered as metal on metal joint replacements. All the boronized surfaces underwent cracking due to the brittle-like ceramic surface.

4. Comparison of wear and friction of Ti6Al4V, Ta, Nb, boronized Ta, boronized Nb

Towards the latter stages of this research, available test conditions and test materials enabled the comparison of Ta, Nb, boronized Ta, and boronized Nb with current orthopedic metal alloy Ti6Al4V. All materials were tested against E52100 with simulated synovial fluid (SSF) between surfaces and at body temperature (37 ^{o}C). The test speed chosen was 1.5 cm/s. Fig. 5.23a indicates that the COF curve for Ti6Al4V is

bereft of a running in period. This indicates that the asperities are easily removed. The wear particles (Fig. 5.28a) are somewhat cylindrical in shape and could probably roll between the contact surfaces causing the fluctuation in COF during the test (Fig. 5.28a). In the case of pristine Nb, there is a definite running in period indicated in Fig. 5.28b. The corresponding AFM images (Fig. 5.29b) indicate the presence of polycrystalline (phase) debris particles on the surface. This is supportive of the running in period. Boronized Nb did not have a running period indicated in the COF curve. The topography image shows a crack on the surface while the phase is very uniform. Pristine tantalum also had a well defined running in period indicated in the COF plot (Fig. 5.28c) whereas boronized Ta didn't. There is presence of different phases (Fig. 5.29d) on the wear track surface of Ta. Boronized Ta had cracks on its wear track (Fig. 5.29e) and the phase appears uniform. These results indicate that boronizing the surface gets rid of a running in period and renders a uniform phase on the surface under metal to metal wear conditions.

Finally, the above mentioned metals were tested against UHMWPE at physiological temperatures and speeds. There is not much difference in the friction coefficient for the different metals. No improvement or drawbacks of Nb, boronized Nb, Ta or boronized Ta over Ti6Al4V can be encountered from friction tests alone. Future tests on wear extent on UHMWPE and possible phase transformations will enlighten us further into the replacement of Ti6Al4V alloy with these novel metals and their boronized counterparts.

CHAPTER VII

CONCLUSIONS

This thesis investigated the tribological behavior of two groups of biomaterials on regarding three major aspects. The first was to study the failure mechanisms of joint prostheses using a tribology approach combined with careful surface characterization (boronized metals). The wear debris were generated and analyzed. The second part was to study the surface-property relationships of bio-tribomaterials. Approaches include comprehensive study of polymer-based hybrid materials as well as metals with coatings. This effort leads to the development of a methodology of bio-tribomaterials characterization and a new understanding of the surface properties of these materials. It was found that the surface properties play a significant role in bio-tribological applications, particularly for a surface like cartilage. The third part was to investigate the tribological behavior, in terms of friction, wear, and nanomechanical properties. The competing mechanisms in surface adhesion, component sliding and bulk elastic properties were found. A new friction mechanism was proposed.

A. SUMMARY OF BIOMATERIAL PROPERTIES

To summerize the materials studied, some of them can be used for future joint repair as far as mechanical and tribological characteristics are concerned.

The composite material formed by combining PTMC with hydroxyapatite and CNTs showed improved strength and friction over cartilage. The improved strength - load bearing and frictional properties are basic factors required of a cartilage tissue engineering scaffold. For future biological applications, its degradation rate and

biocompatibility need to be determined. Liquid absorption, porosity and cell adhesion studies are suggested to be carried out.

The PI+NT composites showed improved performance over UHMWPE. The nanomechanical properties are close to that of cartilage. Changing the concentration of nanotubes resulted in different tribological properties. Alignment and functionalization of the nanotubes can lead to tailored properties that can improve in vivo interaction with tissue, enzymes and synovial fluid. Future mathematical and finite element modeling would be useful in tailoring desired properties.

The pristine and boronized refractory metals represented different friction and wear mechanisms over Ti6Al4V. It was found that using the boron coating, different types of debris can be generated. This leads to a new approach in joint replacement: less-harmful debris can be used to extend the service life. Further more, it was discovered that the tribochemical reactions modify the frictional behavior of joint materials.

B. CONTRIBUTIONS TO FUNDAMENTAL UNDERSTANDING OF TRIBOLOGICAL AND BIOMIMETIC PERFORMANCE

1. Nanomechanical properties

The load-deformation properties of surfaces of potential biomaterials was determined. The relationship between stress and indentation depth was determined for PI + nanotube composites. The specific force **Eρ,** (MN/m3) was determined and corresponding coefficient of these properties are apparently important in understand the behavior of nanostrucred materials.

2. Interfacial properties of a nanocomposite

The friction and deformation behavior of PI + NT composite surfaces were found to be associated with three possible interfacial interactions. They are NT-PI, NT-NT and NT-deformed NT interactions. This theory is useful for future bio-nanomaterial design.

3. Debris formation and wear mechanisms

The study of refractory metals and boronized refractory metals provided useful information on the failure and wear mechanisms. Useful information on the material reactions was also obtained. This information provides the ability to predict the chemical reaction mechanisms of the surfaces and debris formation mechanisms. In general, it opens several new areas of research for biomaterials development.

C. FUTURE SUGGESTIONS

The methodology developed in this thesis research in biomaterials characterization can be applied for future investigations. All material groups can be applied.

Interface investigation of synthetic materials with cells and biological systems is suggested for the next step. This will lead to the understanding of biocompatibility.

Using coatings can decrease friction, increase wear resistance, and further eliminate the formation of wear debris or make it less-harmful.

REFERENCES

1. D. F. Williams: Definitions in biomaterials, in *Proceedings of a Consensus Conference of the European Society for Biomaterials 4, Chester, England,* (Elsevier, New York, 1986).

2. N. Nakabayashi: Dental biomaterials and the healing of dental tissue. *Biomaterials* **24**, 2437-2439 (2003).

3. W. Höland: Biocompatible and bioactive glass-ceramics – state of the art and new directions. *Journal of Non-crystalline Solids Section 3: Glass-Ceramics* **219**, 192-197 (1997).

4. J. S. Cooper, and S. R. Thaller: Repair of orbital floor fractures: application of biomaterials in plastic surgery. *OperativeTechniques in Plastic and Reconstructive Surgery* **9**(2), 49-52 (2002).

5. S.M. Warren, K. D. Fong, R. P. Nakamuli, H. M. Song, T. D. Fang, and M. T. Longaker: Biomaterials for skin and bone replacement and repair in plastic surgery. *Operative Techniques in Plastic and Reconstructive Surgery* **9**(1), 10-15 (2002).

6. H. H. Vandenburgh: Bioengineered muscle constructs and tissue-based therapy for cardiac disease. *Progress inPediatric Cardiology* **21**, 167-171 (2006).

7. M.-A. B. Kruft, A. Benzina, R. Blezer, and L. H. Koole: Studies on radio-opaque polymeric biomaterials with potential applications to endovascular prostheses. *Biomaterials* **17**, 1803-1812 (1996).

8. J. Rieu, and P. Goeuriot: Ceramic composites for biomedical applications. *Clinical Materials* **12**, 211-217 (1993).

9. J. Cohen: Biomaterials in orthopedic surgery. *American Journal of Surgery* **114**, 31-41 (1967).

10. Y. Wang, D.J. Blasioli, H.-J. Kim, H. S. Kim, and D. L. Kaplan: Cartilage tissue engineering with silk scaffolds and human articular chondrocytes. *Biomaterials* **27**, 4434-4442 (2006).

11. J. A. Hubbel: Synthetic biodegradable polymers for tissue engineering and drug delivery. *Current Opinion in Solid State and Materials Science* **3**(3), 246-251 (1998).

12. T. S. Hin: *Engineering Materials for Biomedical Applications.* (World Scientific Publishing Co. Pte. Ltd. Singapore, 2004).

13. J. D. Currey: *Bones, Structure and Mechanics.* (Princeton University Press, Princeton and Oxford, 2002).

14. Y. H. An: in *Mechanical Testing of Bone and the Bon-Implant Interface, 1st. edition*, edited by R. A. Draughn, (CRC press, Boca Raton, USA, 1999).

15. P. Shipman, A. Walker, and D. Bichell: *The Human Skeleton.* (Harvard University Press, Cambridge, MA, and London, England 1985).

16. B. Kingston: *Understandin Joints*. (Stanley Thornes Ltd., Cheltenham 2000).

17. A. W. Ham, and A. H. Cormack: *Histophysiology of cartilage, bone, and joints.* (J. B. Lippincott Company, Philadelphia 1972).

18. D. R. Carter, and G. S. Beaupre. Skeletal function and form, (Cambridge University Press, Cambridge, UK 2001)

19. V. C. Mow, A. Ratcliffe, and A. R. Poole: Cartilage and diarthrodial joints as paradigms for hierachical materials and structures. *Biomaterials* **13**(2), 67-97 (1992).

20. D. T. Felson: Osteoarthritis. *Rheum. Dis. Clin. North Am.* **16**(3), 499-512 (1990).

21. H. Lorenz, and W. Richter: Osteoarthritis: cellular and molecular changes in degenerating cartilage. *Progress in Histochemistry and Cyrochemistry* **40**(3), 135-163 (2006).

22. B. Swoboda: Epidemiological arthrosis research. *Orthopäde* **30**(11), 834-840 (2001).

23. J. A. Buckwalter, and H. J. Mankin: Articular cartilage II. Degeneration and osteoarthritis, repair, regeneration and transplantation. *J. Bone Jt. Surg.* **79A**, 612-632 (1997).

24. J. A. Buckwalter, and J. A. Martin: Degenerative joint disease. *Clinical Symposia, Ciba Geigy, Summit NJ*, 2-32 (1995).

25. J. A. Buckwalter and J. A. Martin: Osteoarthritis. *Advanced drug delivery reviews* **58**, 150-167 (2006).

26. D. T. Felson, R. C. Lawrence, M. C. Hochberg, T. McAlindon, P. A. Dieppe, R. Hirsch, C. G. Helmick, and J. M. Jordan: Osteroarthritis: new insights. Part 1: the disease and its risk factors. *Ann. Intern. Med.* **133**. 635-646 (2000).

27. J. Cushnaghan, and P. Dieppe: Study of 500 patients with limb joint osteoarthritis. I. Analysis by age, sex and distribution of sumptomatic joint sites. *Ann. Rheum. Dis.* **50**, 8-13 (1991).

28. K. D. Brandt: Pain, synovitis and articular cartilage changes in osteoarthritis. *Semin. Arthritis. Rheum.* **18**(2), 77-80 (1989).

29. J. A. Martin, S. M. Ellerbroek, and J. A. Buckwalter: The age-related decline in chondrocyte response to insulin-like growth factor-I: the role of growth factor binding proteins. *Journal of Orthopedic Research* **15**, 491-498 (1997).

30. J. A. Martin, and J. A. Buckwalter: Telomere erosion and senescence in human articular cartilage chondrocytes. *Journal of Gerontology: Biological Sciences.*. **56A**(4), B172-B179 (2001).

31. J. R. Lindstrom, I. V. Ponseti, and D. R. Wenger: Acetabular development after reduction in congenital dislocation of the hip. *Journal of Bone and Joint Surgery* **61A**, 112-118 (1979).

32. Y. Ishii, I. V. Ponseti: Long-term results of closed reduction of complete congenital dislocation of the hip in children under one year of age. *Clinical Orthopaedics,* 167-174 (1978).

33. J. A. Buckwalter, and T. D. Brown: Joint injury, repair, and remodeling: roles in post-traumatic osteoarthritis. *Clinical Orthopaedics and Related Research*, 7-16 (2004).

34. J. A. Martin, T. Brown, A. Heiner, and J. A. Buckwalter: Post traumatic osteoarthritis: the role of accelerated chondrocyte senescence. *Biorheology* **41**, 479-491 (2004).

35. R. M. Stecher: Heberden's nodes. Heredity in hypertrophic arthritis of the finger joints. *American Journal of the Medical Scences* **201**, 801 (1941).

36. C. C. Plato, and A. H. Norris: Osteoarthritis of the hand: age specific joint-digit prevalence rates. *American Journal of Epidemioogy* **109**, 169-180 (1979).

37. M. A. Cimmino, and M. Cutolo: Plasma glucose concentrations in symptomatic osteoarthritis: a clinical and epidemiological survey. *Clinical and Experimental Rheumatology* **8**, 251-257 (1990).

38. T. Stûrmer, H. Brenner, R. E. Brenner, and K. P. Gûnther: Non-insulin dependent diabetes mellitus (NIDDM) and patterns of osteoarthritis. *Scandinavian Journal of Rheumatology.* **30**, 169-171 (2001).

39. J. A. Buckwalter: Regenerating articular cartilage: why the sudden interest? *Orthopadics Today* **16**, 4-5 (1996).

40. J. A. Buckwalter: Were the Junter brothers wrong? Can surgical treatements repair articular cartilage? *Iowa Orthopaedic Journal* **17**, 1-13 (1997).

41. J. A. Buckwalter, J. A. Martin, M. Olmstead, K. A. Athanasiou, M. P. Rosenwasser, and V. C. Mow: Osteochondral repair of primate knee femoral and patellar articular surfaces: implications for preventing post-traumatic osteoarthritis. *Iowa Orthopaedic Journal* **17**, 1-13 (1997).

42. D. T. Felson, J. J. Anderson, A. Naimark, A. M. Walker, and R. F. Meenan: Obesity and knee osteoarthritis. The Framingham study. *Annals of Internal Medicine* **109**, 18024 (1988).

43. J. A. Buckwalter, V. C. Mow and A. Ratliff: Restoration of injured or degenerated articular surfaces. *Journal of the American Academy of Orthopaedic Surgeons* **2,** 192-201 (1994).

44. J. Howse: *Semi-captive Cups for Hip Replacement, in Joint Replacement,* edited by. R. Coombs, A. Gristina, and D. Hungerford (Orthotext, London 1990).

45. G. K. McKee, Total hip replacement-past, present and future, *Biomaterials* **3**. 130-135, 1982.

46. E. J. Haboush: Arthroplasty of the hip based on biomechanics, photo-elasticity, fast-setting dental acrylic, and other considerations. *Bull Hospital of Joint Disorder,* **14,** 242-277 (1953).

47. J. Charnley: Arthroplasty of the hip-a new operation. *The Lancet* **277**(7187), 1129-1132 (1961).

48. J. Charnley: Tissue reactions to polytetrafluorethylene. *The Lancet* **282**(7322), 1379 (1963).

49. D. Dowson: Progress in tribology: a historical perspective, in *Proceedings of the First World Tribology Congress on New Directions in Tribology*, edited by I. M. Hutchings (World Tribology Congress, London, 1997), pp. 3-20.

50. G. K. McKee, and J. Watson-Ferrar: Replacement of arthritic hips by the McKee-Ferrar prosthesis. *Journal of Bone and Joint Surgery* **48B**(2), 245 (1966).

51. R. Tuli, W-J. Li, and R. S. Tuan: Current state of cartilage tissue engineering. *Arthritis Research and Therapy.* **5**, 235-238 (2003).

52. R. Cancedda, B. Dozin, P. Giannoni, R. Quarto: Tissue engineering and cell therapy of cartilage and bone. *Matrix Biology* **22**, 81-91 (2003).

53. L. E. Freed, J. C. Marquis, A. Nohria, J. Emmanual, A. G. Mikos, and R. Langer: Neocartilage formation in vitro and in vivo using cells cultured on synthetic biodegradable polymers. *Journal of Biomedical Materials Research* **27**, 11-23 (1993).

54. D. A. Grande, C. Halberstadt, G. Naughton, R. Schwartz, and R. Manji: Evaluation of matrix scaffolds for tissue engineering of articular cartilage grafts. *Journal of Biomedical Materials Research* **34**, 211-220 (1997).

55. K. Yasuda, J. P. Gong, Y. Katsuyama, A. Nakayama, Y. Tanabe, E. Kondo, M. Ueno, and Y. Osada: Biomechanical properties of high-toughness double network hydrogels. *Biomaterials* **26**, 4468-4475 (2005).

56. M. Oka, T. Noguchi, P. Kumar, K. Ikeuchi, T. Yamamuro, S. H. Hyon and Y. Ikada: Development of an artificial articular cartilage. *Clinical Materials* **6**(4), 361-381 (1990).

57. R. J. Covert, R. D. Ott, and D. N. Ku: Friction characteristics of a potential articular cartilage biomaterial. *Wear* **255**, 1064-1068 (2003).

58. M. E. Freeman, M. J. Furey, B. J. Love, and J. M. Hampton: Friction, wear and lubrication of hydrogels as synthetic articular cartilage, *Wear* **241**, 129-135 (2000).

59. W. Święszkowski, D. N. Ku, H. E. N. Bersee, and K. J. Kurzydlowski: An elastic material for cartilage replacement in an arthritic shoulder joint. *Biomaterials* **27**, 1534-1541 (2006).

60. N. P. Suh: *Tribophysics.* (Prentice-Hall, NJ, 1986).

61. G. W. Stachowiak, and A. W. Batchelor: *Engineering Tribology. 3rd. ed.* (Elsevier Butterworth-Heinemann, Burlington, MA, 2005).

62. Y. Zhang: Boundary lubrication-an important lubrication in the following time. *Journal of Molecular Liquids* **128**(1-3), 56-59 (2006).

63. B. A. Hills, and R. W. Crawford: Normal and prosthetic synovial joints are lubricated by surface-active phospholipid. *The Journal of Arthroplasty* **18**(4), 499-505 (2003).

64. F. C. Linn: Lubrication of animal joints. II. The mechanism. *Journal of Biomechanics* **1**, 193-205 (1968).

65. R. I. Tanner: An alternative mechanism for the lubrication of synovial joints. *Physics in Medicine and Biology* **11**(1), 119-127 (1966).

66. C. W. McCutchen: Mechanism of animal joints. *Nature* **184**, 1284 (1959).

67. P. S. Walker, A. Unsworth, D. Dowson, J. Sikorski, and V. Wright: Mode of aggregation of hyaluronic acid protein complex on the surface of articular cartilage**.** *Annals of the Rheumatic Diseases* **29**, 591-602 (1970).

68. J. H. Dumbleton: *Tribology of Natural and Artificial Joints.* (Elsevier Scientific Publishing Co., Amsterdam 1981).

69. A. G. Ogston, and J. E. Stanier: Further observations on the preparation and composition of the hyaluronic acid complex of ox synovial fluid. *Biochemical Journal* **52**, 149 (1952).

70. D. J-Vahid, M. Jagatia, Z. M. Jin, and D. Dowson: Prediction of lubricating film thickness in UHMWPE hip joint replacements. *Journal of Biomechanics* **34**(2), 261-266 (2001).

71. M. Schaldach, and D. Hohmann: *Advances in Artificial Hip and Knee Joint Technology.* (Springer-Verlag, New York, 1976).

72. A. Pizzoferrato, G. Ciapetti, S. Stea, and A. Toni: Cellular events in the mechanisms of prosthesis loosening. *Clinical Materials* **7**. 51-81 (1991).

73. V. V. Surin, K. Sundholm, and L. Backman: Infection after total hip replacement. *Journal of Bone and Joint Surgery* **68-B**, 412-418 (1993).

74. J. Charnley: Post-perative infection after total hip replacement with special reference to air contamination in the operating room. *Clinical Orthopaedics* **87**, 167-187 (1972).

75. R. Poss, T. S. Thornhill, F. C. Ewald, W. H. Thomas, N. J. Batte and C. B. Sledge: Factors influencing the incidence and outcome of infection following total joint arthroplasty. *Clinical Orthopaedics* **182**, 117-126 (1984).

76. H. W. Buchholz, and K. Heinert: Long term results of cemented arthroplasty. *Orthopedic Clinics of North America* **19**, 531-540 (1988).

77. V. Pacheco, P. Shelley, and B. M. Wroblewski: Mechanical loosening of the stem in Charnley arthroplasties. *Journal of Bone and Joint Surgery* **70-B**, 596-599 (1988).

78. J. P. Iannotti, R. A. Balderston, R. E. Booth, R. H. Rothman, J. C. Cohn, and G. Pickens: Aseptic loosening after total hip arthroplasty. Incidence, clinical significance, and etiology. *Journal of Arthroplasty* **1.** 99-107 (1986).

79. D. W. Robersts, R. Poss, and K. Kelley. Radiographic comparison of cementing techniques in total hip arthroplasty. *Journal of Arthroplasty* **1**. 241-247 (1986).

80. S. H. Teoh: Fatigue of biomaterials: a review. *International Journal of Fatigue* **22**, 825-837 (2000).

81. J. Black: *Biological Performance of Materials: Fundamentals of Biocompatibility.* (Marcel Dekker, Basel, Switzerland 1999).

82. S. Ralph, and M. D. Greco: *Implantation Biology: The Host Response and Biomedical Devices.* (CRC Press, London, 1994).

83. S. Santavirta, Y. T. Konttinen, R. Lappalainen, A. Anttila, S. B. Goodman, M. Lind, L. Smith, M. Takagi, E. Gómez-Barrena, L. Nordsletten, and J. –W. Xu: Materials in total joint replacement. *Current Orthopaedics* **12**. 51-57 (1998).

84. S. Li, and A. H. Burstein: Ultra high molecular weight polyethylene. The material and its use in total hip joint implants. *Journal of Bone and Joint Surgery* **76A**, 1080-1090 (1994).

85. E. Gómez-Barrena, J. D. Chang, and S. Li: The role of polyethylene properties in osteolysis after total hip replacement, in Instructional course lectures 45, edited by D. J. Pritchard, (American Academy of Orthopaedic Surgeons, Rosemont IL, 1996), pp. 187-197.

86. V. Premnath, W.H. Harris, M. Jasty, and E. W. Merill: Gamma sterilization of UHMWPE articular implants: an analysis of the oxidation problem. *Biomaterials* **17**. 1741-1753 (1996).

87. A. A. Edidin, L. Pruitt, C. W. Jewett, D. J. Crane, D. Roberts, and S. M. Kurtz: Plasticity induced damage layer is a precursor to wear in radiation-cross-linked UHMWPE acetabular components for total hip replacement. *Journal of Arthroplasty* **14**(5), 616-627 (1999).

88. A. Wang, D .C. Sun, S. S. Yau, B. Edwards, M. Sokol, A. Essner, V. K. Polineni, C. Stark, and J. H. Dumbleton: Orientation softening in the deformation and wear of ultrahigh molecular weight polyethylene. *Wear* **203**, 230-241 (1997).

89. L. A. Pruitt: Deformation, yielding, fracture and fatigue behavior of conventional and highly cross-linked ultra high molecular weight polyethylene. *Biomaterials* **26**, 905-915 (2005).

90. R. S. Pascaud, W. T. Evans, P. J. McCullagh, and D. P. Fitzpatrick: Influence of gamma-irradiation sterilization and temperature on the fracture toughness of ultra-high-molecular-weight polyethylene. *Biomaterials* **18**, 727-735 (1997).

91. S. M. Kurtz, C. M. Rimnac, L. Pruitt, C. W. Jewett, V. Goldberg, and A. A. Edidin: The relationship between the clinical performance and large deformation mechanical behavior of retrieved UHMWPE tibial inserts. *Biomaterials* **21**, 283-291 (2000).

92. *Artificial Hip and Knee Joint Technology*,.edited by M. Schaldach, D. Hohmann, R. Thull and F. Hein (Springer-Verlag Berlin, Heidelberg, New York, 1976).

93. J. Raghunath, H. J. Salacinski, K. M. Sales, P. E. Butler, and A. M. Seifalian: Advancing cartilage tissue engineering: the application of stem cell technology. *Current Opinion in Biotechnology* **16**, 503-509 (2005).

94. F. Shapiro, S. Koide, and M. J. Glimcher: Cell origin and differentiation in the repair of full thickness defects of articular cartilage. *Journal of Bone and Joint Surgery* **75A**, 532-553 (1993).

95. T. Ahsan, and R. L. Sah: Biomechanics of integrative cartilage repair. *Osteoarthritis and Cartilage* **7**, 29-40 (1999).

96. H. J. Mankin: The response of articular cartilage to mechanical injury. *Journal of Bone and Joint Surgery* **64-A**, 460-466 (1982).

97. K. Ushio, M. Oka, S-H. Hyon, T. Hayami, S. Yura, K. Matsumura, J. Toguchida, T. Nakamura: Attachment of artificial cartilage to underlying bone. *Journal of Biomedical Mateials Research Part B: Applied Biomaterials* **68B**, 59-68 (2004).

98. M. A. Freeman, M. J. Furey, B. J. Love, and J. M. Hampton: Friction, wear and lubrication of hydrogels as synthetic articular cartilage, *Wear* **241**, 129-135 (2000)

99. R. J. Covert, R. D. Ott, and D. N. Ku: Friction characteristics of a potential articular cartilage biomaterial. *Wear* **255**, 1064-1068 (2003).

100. H. G. Burkitt, B. Young, and J. W. Heath: *Functional Histology, 3rd ed.* (Longman Group, UK Limited, 1993).

101. R. B. Martin, D. B. Burr and N. A. Sharkey: *Skeletal Tissue Mechanics.* (Springer-Verlag, New York, Inc. 1998).

102. *Bone Mechanicas Handbook*, *2nd ed.,* edited by S. C. Cowin, (CRC press, Boca Raton, FL, 2001).

103. P. Gehron-Robey, and A. L. Boskey: The biochemistry of bone, in: *Osteoporosis,* edited by F. Marcus, D. Feldman, and J. Kelsey, (Academic Press, San Diego, CA, 1996).

104. J. B. Lian, G. S. Stein, E. Canalis, P. Gehron-Robey, and A. L. Boskey, Bone formation: osteoblast lineage cells, growth factors, matrix proteins and the mineralization process, in *Primer on the Metabolic Bone Diseases and Disorders*

of Mineral Metabolism, 4th. Ed., edited by. M. J. Favus, (Lippincott/Williams & Wilkins, Philadelphia, 1999).

105. J. P. Gorski: Is all bone the same? Distinctive distributions and properties of non-collagenous matrix proteins in lamellar and woven bone imply the existence of different underlying osteogenic mechanisms, *Critical Reviews in Oral Biology* **9**, 201 (1998).

106. V. Levitin: *High Temperature Strain of Metals and Alloys: Physical Fundamentals,* (Wiley-VCH, Weinheim 2006).

107. H. Matsuno, A. Yokoyama, F. Watari, M. Uo, and T. Kawasaki: Biocompatibility and osteogenesis of refractory metal implants, titanium, hafnium, tantalum and rhenium. *Biomaterials* **22**, 1253-1262 (2001).

108. M. F. Semlitsch, H .Weber, and R. M. Streicher: Joint replacement components made of hot-forged and surface-treated Ti-6Al-7Nb alloy. *Biomaterials* **13**, 781-788 (1992).

109. H. Matsumae: An experimental study of tantalum and zirconium as biomaterials. *J. Jpn. Stomatol Soc.* **37**(4), 862-878 (1988).

110. M. Fujita: In vitro study on biocompatibility of zirconium and titanium. *Journal of the Stomatological Society Japan* **60**. 54-65 (1993).

111. J. H. Yoon, Y. K. Jee, S. Y. Lee: Plasma paste boronizing treatment of the stainless steel AISI 304. *Surface and Coatings Technology* **112**(1-3), 71-75 (1999).

112. A. Küper, X. Qiao, H. R. Stock, and P. Mayr: A novel approach to gas boronizing. *Surface and Coatings Technology* **130**(1): 87-94 (2000).

113. K. Stewart, Boronizing protects metals against wear, *Advanced Materials and Processes* **3**, 23-25 (1997).

114. C. Meric, S. Sahin, B. Backir, and N. S. Koksal: Investigation of the boronizing effect on the abrasive wear behavior in cast irons. *Materials and Design* **27**(9), 751-757 (2005).

115. B. Selçuk, R. İpek, M. B. Karamiş, and V. Kuzuku: An investigation on surface properties of treated low carbon and alloyed steels (boriding and carburizing). *Journal of Materials Processing Technology* **103**, 310-317 (2000).

116. R. İpek, B. Selçuk, M. B. Karamiş, V. Kuzuku, and A. Yücel: An evaluation of the possibilities of using borided GG25cast iron instead of chilled GG25 cast iron (surface properties). *Journal of Materials Processing Technology* **105**, 73-79 (2000).

117. U. Sen, S. Sen, and F. Yilmaz: Structural characterization of boride layer on boronized ductile iron. *Surface and CoatingsTechnology* **176**, 222-228 (2004).

118. C. Martini, G. Palombarini: Mechanism of thermochemical growth of iron borides on iron. *Journal of Materials Science* **39**, 933-937 (2004).

119. J. Subrahmanyam: Wear studies on boronized mild steel. *Wear* **95**, 287-292 (1984).

120. K. –H. Habig, and R. C. Fischer: Wear behaviour of boride layers on alloyed steels *Tribology International* **14**, 209 (1981).

121. H.-J. Hunger and G. Trute: Boronizing to produce wear-resistant surface Layers. *Heat Treatment of Metals* **2,** 31-39 (1994).

122. S. V. Bhat: *Biomaterials,* (Kluwer Academic Publishers, New Delhi 2002).

123. K. S. Katti: Biomaterials in total joint replacement: *Colloids and Surfaces B: Biointerfaces* **39**(3), 133-142 (2004).

124. G. Lewis: Polyethylene wear in total hip and knee arthroplasties. *Journal of Biomedical Materials Research* **38**(1), 55-75 (1997).

125. J.-T. Hong, N.-S. Yoon, T.-H Kim, D.-H Lee, and W.-G. Kim: Preparation and characterization of biodegradable poly(trimethylenecarbonate-e-caprolactone)-block-poly(p-diozanone) copolymers. *Journal of Polymer Science: Part A: Polymer Chemistry* **43**, 2790-2799 (2005).

126. I. Engelberg, and J. Kohn: Physico-mechanical properties of degradable polymers used in medical applications: a comparative study. *Biomaterials* **12**, 292-304 (1991).

127. M. Schappacher, T. Fabre, A. F. Mingotaud, and A. Soum: Study of a (trimethylenecarbonate-co-e-caprolactone) polyker-Part 1: preparation of a new nerve guide through controlled random copolymerization using rare earth catalysis, *Biomaterials* **22**, 2849-2855 (2001).

128. J. C. Middleton, and A. J. Tipton: Synthetic biodegradable polymers as orthopedic devices. *Biomaterials* **21**. 2335-2346 (2000).

129. K. A. Athanasiou, C. E. Agrawal, F. A. Barber, and S. S. Burkhart: Orthopaedic applications for PLA-PGA biodegradable polymers. *Arthrosc: Journal of Arthroscopic and Related Surgery* **14**(7), 726-737 (1998).

130. E. A. Wang, V. Rosen, J. S. D'jAlessandro, M. Bauduy, P. Cordes, T. Harada, D. I. Israel, R. M. Hewick, K. M. Kerns, P. LaPan, D. Luxenberg, D. McQuaid, I. K.

Moutsatsos, J. Nove, and J. M. Wozney: Recombinant human bone morphogenic protein induces bone formation. *Proceedings of the National Academy of Sciences* **87**, 2220-2224 (1990).

131. M. Ramchandani, and D. Robinson: In vitro release of ciprofloxacin from PLGA 50:50 implants. *Journal of Controlled Release* **54**, 167-175 (1998).

132. G. Odian: *Principles of Polymerization, 2nd ed.* (New York, Wiley Interscience, 1981).

133. Z. Zhang, R. Kuijer, S. K. Bulstra, D. W. Grijpma, and J. Feijen: The in vivo and in vitro degradation behavior of poly(trimethylene carbonate). *Biomaterials* **27**, 1741-1748 (2006).

134. S. A. M. Ali, S. –P. Zhong, P. J. Doherty, and D. F. Williams: Mechanisms of polymer degradation in implantable devices I. Poly(caprolactone). *Biomaterials* **14**(9), 648-656 (1993).

135. I. Engelberg, and J. Kohn: Physico-mechanical properties of degradable polymers used in medical applications: a comparative study. *Biomaterials* **12**, 292-304 (1991).

136. S. L. Ishaug-Riley, L. E. Okun, F. Prado, M. A. Applegate, and A. Ratcliffe: Human articular chondrocyte adhesion and proliferation on synthetic biodegradable polymer films. *Biomaterials* **20**, 2245-2256 (1999).

137. X. Jiang, Y. Bin, and M. Matsuo: Electrical and mechanical properties of polyimide-carbon nanotubes composites fabricated by in situ polymerization. *Polymer* **46**, 7418-7424 (2005).

138. C. Shen, and J. H. Dumbleton: The evaluation of a polyimide and a poly(amide-imide) as joint replacement materials. *Wear* **40**, 351-360 (1976).

139. R. R. Richardson Jr., J. A. Miller, and W. M. Reichert: Polyimides as biomaterials: preliminary biocompatibility testing. *Biomaterials* **14**(8), 627-635 (1993).

140. H. Cai, F. Yan, and Q. Xue: Investigation of tribological properties of polyimide/carbon nanotube nanocomposites. *Materials Science and Engineering A* **364**, 94-100 (2004).

141. S. K. Smart, A. I. Cassady, G. Q. Lu, and D. J. Martin: The biocompatibility of carbon nanotubes. *Carbon* **44**, 1034-1047 (2006).

142. E. Cenni, D. Granchi, C. R. Arciola, G. Ciapetti, L. Savarino, and S. Stea: Adhesive protein expression on endothelial cells after contact in vitro with polyethylene terephthalate coated with pyrolitic carbon. *Biomaterials* **16**(16), 1223-1227 (1995).

143. L. Ma, G. Sines: Fatigue behavior of a pyrolitic carbon. *Journal of Biomedical Materials Research* **51A**(1), 61-68 (2000).

144. A. D. Haubold: Blood/carbon interactions. *ASAIO J.* **6**, 88-92 (1983).

145. D. J. Darensbourg, P. Ganguly, and D. R. Billodeaux: Ring opening polymerization of trimethylene carbonate using aluminum (III) and tin (IV) salen chloride catalysts. *Macromolecules* **38**(13), 5406-5410 (2005).

146. S. Banda: Characterization of aligned carbon nanotubes/polymer composites. Master of science thesis, (Virginia Commonwealth University, Richmond, Virginia, 2004).

147. Distributor's website: http://www.goodfellow.com (accessed on 9th June, 2006).

148. T. Kokubo, H. Kushitani. and S. Sakka: Solutions able to reproduce in vivo surface-structure changes in bioactive glass-ceramic A-W. *Journal of Biomedical Materials Research*, **24,** 721-734 (1990).

149. X. F. Shi: Apatite coating over zirconium metal by a biomimetic method, (Master of science thesis, Rose-Hulman Institute of Technology, Terre Haute, IN, 2002).

150. D. Chescoe, and P. J. Goodhew: *The Operation of the Transmission Electron Microscope* (Oxford University Press, Royal Microscopical Society, New York 1984).

151. J. J. Bozzola, and L. D. Russel: *Electron Microscopy: Principles and Techniques for Biologists 2nd ed.* (Jones and Bartlett, Sadbury MA, 1999).

152. R. Ribeiro, S. Ingole, M. Usta, C. Bindal, A. H. Ucisik and H. Liang: A tribological comparison of pure and boronized chromium,. *Journal of Tribology* **128**, 895-897 (2006).

153. J. P. Paul: Joint kinetics. in *The Joints and Synovial Fluid, Vol. II*, edited by L. Sokoloff, (Academic Press, New York, 1980).

154. W. A. Hodge, R. S. Fijan, K. L. Carlson, R. G. Burgess, W. H. Harris, and R. W. Mann: Contact pressure in the human hip joint measured in vivo, in *Proc. Natl Acad. Sci.,* (National Academy of Science, USA, 1986), pp. 2879-2883.

155. http://www.matweb.com (accessed on 8th. June, 2006).

156. R. Ribeiro, S. Ingole, C. Bindal, A. H. Ucisik, M. Usta: Tribological investigation of tantalum boride coating under dry and simulated body fluid conditions, in press: *Wear (2006).*

157. M. Usta, I. Ozbek, C. Bindal, A. H. Ucisik, S. Ingole, and H. Liang: A comparative study of borided pure niobium**,** tungsten and chromium. *Vacuum* **80** (11, 12), 1321-1325 (2006).

VITA

Rahul Ribeiro studied in several schools before going to the Marine Engineering and Research Institute, Kolkata, India for undergraduate studies in Marine Engineering. He worked for five years in the Merchant Navy as a Marine Engineer. He obtained a Master of Science degree in Mechanical Engineering in the year 2003 and a Doctor of Philosophy degree in Materials Science and Engineering in 2006 from Texas A&M University.

Mr. Ribeiro is an active researcher in various areas of science and engineering. His Ph.D. dissertation was mainly involved with investigating materials for bone joint applications. His experience includes running and maintenance of diesel engines, air compressors, boilers turbines, alternators, and also research related to tribology, materials science, and tissue and cell experimentation.

He is a percussionist of eastern and western pop and rock music. He has held key leadership and volunteer positions in various organizations ranging from a housing community to an engineering department student organization.

Mr. Rahul Ribeiro can be reached at MS 3123, Texas A&M University, College Station, TX 77843. His email address is rahulr@neo.tamu.edu.